ЕЛЕКТРОТЕХНИЧКИ ФАКУЛТЕТ
УНИВЕРЗИТЕТА У БАЊОЈ ЛУЦИ

FACULTY OF ELECTRICAL ENGINEERING
UNIVERSITY OF BANJALUKA

ELEKTRONIKA

ELECTRONICS

YU ISSN 1450-5843

ГОДИШТЕ 10, BROJ 1, СЕПТЕМБАР/ОКТОБАР 2006. *VOLUME 10, NUMBER 1, SEPT/OCT 2006.*

F A C U L T Y O F E L E C T R I C A L E N G I N E E R I N G
U N I V E R S I T Y O F B A N J A L U K A

Address: Patre 5, 78000 Banjaluka, Republic of Srpska, Bosnia and Herzegovina
Phone: + 387 51 211-408, + 387 51 221-820
Fax: + 387 51 211-408

E L E C T R O N I C S

e-mail: elektronika@etfbl.net

Editor: Prof. Branko L. Dokić, Ph. D.
Faculty of Electrical Engineering
University of Banjaluka, Republic of Srpska
e-mail: bdokic@etfbl.net

Secretary: Petar Matić, M.Sc.
e-mail: pero@etfbl.net,
Faculty of Electrical Engineering
University of Banjaluka, Republic of Srpska

Publisher: Faculty of Electrical Engineering
University of Banjaluka, Republic of Srpska
Address: Patre 5, 78000 Banjaluka, Republic of Srpska, Bosnia and Herzegovina
Phone: + 387 51 211-408, + 387 51 221-820
Fax: + 387 51 211-408
http://www.etfbl.net

Number of printed copies: 150

PREFACE

The articles in this journal discuss the problems and future trends in digital control of electric drives. Particular attention is paid to the motion control algorithms and to the developments in the power conversion control. Specific influence of an ever increased number crunching capability of modern digital controllers on the drive controller structures is probed deeply. Performance enhancements of semiconductor power switches are outlined and their influence on the drive converter topology and characteristics is briefly analyzed. Finally, the needs and the possibilities are outlined for a digitally controlled drive to assume versatile adaptation and self -commissioning features, reducing in such a way the need for the operators intervention in both the installation and regular operation phases.

Contemporary motion control systems employ DSP controlled AC drives. The growth of electric drives is determined by the current level of technology. High reliability, long lifetime, relatively low maintenance and short startup times of electric drives are in consort with their ecological compatibility: low emission of pollutants. The quality of electric drives is extended by a high efficiency, low no-load losses, high overload capability, fast dynamic response, the possibility of recuperation, and immediate readiness for the full-featured operation after the drive startup. Electric drives are available in a wide range of rated speeds, torques and power, they allow for a continuous speed regulation, reversal capability, and they easily adapt to different environment conditions such as the explosive atmosphere or clean room requirements. Unlike the IC engines, electric motors provide for a ripple-free, continuous torque and secure a smooth drive operation.

During the past two decades, the evolution of powerful digital microcontrollers allowed for a full-digital control of the electromechanical conversion processes taking place in an electrical drives. The process automation made significant progress in the fifties, thanks to the introduction of numerical control (NC). Although not flexible and fully programmable, NC systems replaced relays and mechanical timers common on the factory floor in the first half of the century. As the first reliable and commercially available microcontrollers were made in the sixties, they were advantageously used for the purpose of a flexible control of electric drives in production machines. As from then, the hydraulic and pneumatic actuators gradually disappear and give space to DC and AC electric motors. Among the first applications of variable speed frequency controlled AC drives were pumps, fans and compressors, where the speed regulation feature eliminated mechanical damping of the fluid flow and reduced the associated power losses and turbulence. For their increased reliability, low maintenance, and better characteristics, the frequency controlled induction motors gradually replaced DC drives in many of their traditional fields of application. Further technological improvements made the frequency controlled AC drives the cheapest actuators ever. Compact digital controllers emulate the functions traditionally implemented in the analog form and allow also the execution of nonlinear and complex functions that could not have been completed by analog circuitry (ANN, nonlinear estimators, spectrum estimation and others). Highly evolved observers of the drive states allow reduction of the number of sensors. The drives with minimum number of sensors and the shaft sensorless drives are more robust and reliable than their sensored counterparts. The lack of sensors and associated cables makes the drive cheaper and the installation simpler and faster. In the development phase are the advanced parallel control structures such as the direct and incremental torque control that make the use of a large numerical throughput to implement a non-cascade control concept thereupon augmenting the response speed and overall drive dynamic performance.

The growth of high performance drives depends on the investments in new production sites. Recent trends of replacing production sites to countries where the labour cost is lower calls for more advanced motion control systems, requiring less maintenance and skilled workers. The elements of motion control systems, and in particular the power electronic units became commodity products, their cost becoming one of the main issues. At the same time, the energy efficiency, a higher peak-to-rated power ratio, the energy quality and the regenerative braking imposed new standards to power converter topologies and solutions.

SHORT BIOGRAPHY OF GUEST EDITOR

Slobodan N. Vukosavic (M'93) was born in Sarajevo, Yugoslavia, in 1962. He received the B.S., M.S., and Ph.D. degrees from the University of Belgrade, Yugoslavia, in 1985, 1987, and 1989, respectively. He was employed in the Nikola Tesla Institute, Belgrade. He joined the ESCD Laboratory of Emerson Electric, St. Louis, MO. in 1988. Since 1991, he has been with the Vickers Electrics and MOOG Electric, designing motion control products. He is currently professor at the University of Belgrade, ETF, where he serves as the Department Head of the Power Engineering. His students won the IEEE IFEC contest in 2005. Member of the Yugoslav National Academy of Engineering, he published extensively and has completed over 40 large R/D and industrial projects.

At the Faculty of Electrical Engineering, University of Belgrade, S. N. Vukosavic is engaged in delivering lectures to graduates and postgraduates in the field of control of electrical drives, electrical machines and power electronics; developed and led the Laboratory for Digital Control of Electrical Drives at the University of Belgrade, and Electrical Traction Laboratory. S. N. Vukosavic was visiting professor, lecturer at postgraduate courses, and gave seminars on Electrical Drives at Technical Institutes and Universities of Novi Sad, Torino, Genova and Boston.

S. N. Vukosavic published 62 scientific papers in international and 43 in national journals; he presented 15 invited papers and tutorials, conducted 31 international prooject and is the author of patented technical solutions and inventions. His publications are focused on Electrical drives and power converters control, Power electronics, System modeling and identification, Microcomputer-based real-time control and the Electrical machines design and control. His papers are cited in leading international publications; repeated referencing is also found in *Wiley Encyclopedia of Electrical and Electronics Engineering.*

SINUSOIDAL OUTPUT VOLTAGE GENERATION WITH FIVE-PHASE VOLTAGE SOURCE INVERTERS

Emil Levi

Abstract: *Five-phase variable-speed drives are currently considered for numerous applications. If the machine is designed with a sinusoidally distributed stator winding, the supply should consist of the fundamental harmonic only. Since five-phase drives are invariably supplied from five-phase voltage source inverters (VSIs), adequate methods for VSI pulse width modulation (PWM) are required. This paper analyses space vector and carrier-based PWM schemes for a five-phase VSI, which provide sinusoidal output voltages and can therefore be used for five-phase motor drives with sinusoidal distribution of windings. A detailed model of a five-phase VSI is presented first. Next, a space vector PWM (SVPWM) method is introduced, which enables operation with pure sinusoidal output voltages up to a certain reference voltage value. An equivalent carrier-based PWM, with the fifth harmonic injection, is further introduced and it is shown that it offers the same quality of performance as the SVPWM. Carrier-based PWM however offers advantages from implementation point of view. Simulation results are included throughout the paper to illustrate and verify the theoretical considerations.*

Keywords: *Carrier-based PWM, Five-phase voltage source inverter, Space vector modulation, Sinusoidal output.*

1. INTRODUCTION

A number of PWM techniques have been developed in the past to control a three-phase VSI [1]. However, SVPWM has become the most popular one because of the easiness of digital implementation and better DC bus utilisation, when compared to the sinusoidal PWM method. With the advent of multiphase motor drive systems, a need has arisen to develop appropriate PWM techniques for multi-phase inverters. There are currently only a very few PWM schemes available for inverters with a phase number greater than three. The emphasis in such developments has been on SVPWM, following the analogy with the three-phase VSI. In principle, there is a lot of flexibility available in choosing the proper space vector combination for an effective control of multi-phase VSIs because of a large number of space vectors.

A specific problem, encountered in multi-phase drive systems, is that generation of certain low-order voltage harmonics in the VSI output can lead to large stator current harmonics, since these are in essence restricted only by stator leakage impedance [2]. For example, if a five-phase machine with sinusoidal winding distribution is supplied with voltages containing the 3rd and the 7th harmonic, stator current harmonics of the 3rd and the 7th order will freely flow through the machine and their amplitude will be restricted by stator leakage impedance only. It is therefore important that the multi-phase VSI output is kept as close as possible to sinusoidal and the SVPWM scheme of [2], for a dual-three phase machine, was developed with exactly this reasoning in mind. On the other hand, five-phase machines can be designed with concentrated windings and in such a case it is desirable to utilise the third harmonic stator current injection to enhance the torque production [3]. Since now both the fundamental and the third stator current harmonic are controlled, it is necessary to have a suitable PWM technique, which enables control of both the fundamental and the third harmonic of the stator supply voltage. A space vector PWM method, proposed in [4], has been developed for this type of a five-phase machine. It is based on the vector space decomposition technique and the inverter output voltages contain the fundamental and the third harmonic, which are both of controllable magnitudes.

If a five-phase machine is with a sinusoidally distributed winding, the output voltages should contain only the fundamental component and they need to be free of low-order harmonics. A five-phase VSI offers a total of $2^5 = 32$ space vectors, of which thirty are active state vectors, forming three concentric decagons, and two are zero state vectors. The simplest method of realising SVPWM is to utilise only ten large length vectors, belonging to the largest decagon in the *d-q* plane, in order to implement the symmetrical SVPWM [5, 6]. Two active space vectors neighbouring the reference space vector and two zero space vectors are utilised to synthesise the input reference voltage. This method is a simple extension of space vector modulation of three-phase VSIs. While being the simplest possible, it leads to generation of low-order output voltage harmonics of significant values, as shown in [7]. The reason is that only two active space vectors are used, instead of four. As discussed in [8] in conjunction with a SVPWM technique developed for a nine-phase inverter with sinusoidal output, the number of applied active vectors in SVPWM of a multi-phase VSI should be equal to $n-1$, where n is the (odd) number of phases. This translates into the need to apply not only large but medium length space vectors as well in the case of a five-phase VSI.

Realisation of sinusoidal output voltages by means of SVPWM of a five-phase VSI is described in [7,9]. By combining the utilisation of large and medium length neighbouring space vectors in an appropriate manner, perfectly sinusoidal output voltages are created. However, this situation can only be maintained up to a certain value of the input reference, which is smaller than the maximum reference achievable with the given DC link voltage. Extension of the inverter operating region up the maximum achievable output voltage inevitably requires operation with unwanted harmonics of the order $10n\pm3$, n=0,1,2,3,… [7].

This paper at first reviews the principles of SVPWM for a five-phase VSI, discussed at length in [7], aimed at achieving operation with sinusoidal output. Next, a carrier-based PWM schemes for a five-phase VSI is elaborated. It is interesting to note that, until now, hardly any effort has been put into investigating carrier-based PWM schemes for multi-phase VSIs (the only available work related to this subject appears to be [10], where discontinuous carrier-based schemes were analysed to some extent).

It is shown in the paper that carrier-based PWM with the fifth harmonic injection enables the same utilisation of the DC bus voltage as the corresponding SVPWM, while being considerably simpler for practical implementation. Theoretical analysis is supported by simulation results.

2. REPRESENTATION OF A FIVE-PHASE VSI

Power circuit topology of a five-phase voltage source inverter is shown in Fig. 1. The load is taken as star-connected with isolated neutral point and the inverter output phase voltages are denoted with lower case symbols (*a,b,c,d,e*), while the leg voltages have symbols in capital letters (*A,B,C,D,E*). The model of the five-phase VSI is developed in space vector form. The relationship between the machine's phase-to-neutral voltages and inverter leg voltages is given with (the inverter leg voltages take the values of ± $0.5V_{DC}$)

$$\begin{aligned} v_a &= (4/5)v_A - (1/5)(v_B + v_C + v_D + v_E) \\ v_b &= (4/5)v_B - (1/5)(v_A + v_C + v_D + v_E) \\ v_c &= (4/5)v_C - (1/5)(v_A + v_B + v_D + v_E) \\ v_d &= (4/5)v_D - (1/5)(v_A + v_B + v_C + v_E) \\ v_e &= (4/5)v_E - (1/5)(v_A + v_B + v_C + v_D) \end{aligned} \tag{1}$$

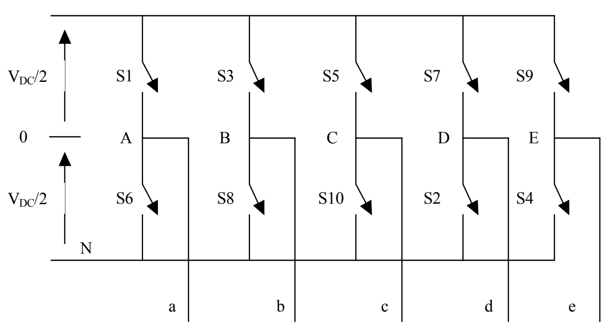

Fig. 1. Five-phase voltage source inverter circuit.

Since a five-phase VSI is under consideration, one deals here with a five-dimensional space. Hence two space vectors have to be defined, each of which describes space vectors in one two-dimensional subspace (*d-q* and *x-y*). The third subspace is single-dimensional (zero sequence) and it cannot be excited due to the assumed star connection of the system with isolated neutral point. Space vectors of phase voltages are defined in the stationary reference frame, using power variant transformation, as:

$$\underline{v}_{dq} = v_d + jv_q = 2/5(v_a + \underline{a}v_b + \underline{a}^2 v_c + \underline{a}^{*2} v_d + \underline{a}^* v_e) \tag{2}$$

$$\underline{v}_{xy} = v_x + jv_y = 2/5(v_a + \underline{a}^2 v_b + \underline{a}^* v_c + \underline{a}v_d + \underline{a}^{*2} v_e) \tag{3}$$

where $\underline{a}$ = exp(j2π/5), $\underline{a}^2$ = exp(j4π/5), $\underline{a}$* = exp(-j2π/5), $\underline{a}^{*2}$ = exp(-j4π/5) and * stands for a complex conjugate.

In general, an *n*-phase two-level VSI has a total of 2^n space vectors. Thus in the case of a five-phase VSI there are 32 space vectors, two of which are zero vectors. The remaining 30 active vectors form three decagons in both *d-q* and *x-y* planes and are calculated using (2)-(3) in conjunction with inverter output phase voltages of (1) for each possible inverter state. The phase voltage space vectors in the *d-q* plane are summarised in Table I for all 32 switching states, while corresponding space vectors in the *x-y* plane are given in Table II. The five-phase VSI space vectors in the *d-q* plane and in the *x-y* plane are shown in Fig. 2. It can be seen from Fig. 2 that the outer decagon space vectors of the *d-q* plane map into the inner decagon of the *x-y* plane, the innermost decagon of *d-q* plane forms the outer decagon of the *x-y* plane, while the middle decagon space vectors map into the same region. In general, the harmonics of the order $10n\pm1$ (*n* = 0,1,2,3…) map into the *d-q* subspace, while the harmonics of the order $10n\pm3$ (*n* = 0,1,2,3…) map into the *x-y* subspace [4]. Since all the available non-zero space vectors map into both subspaces, the problem of sinusoidal output voltage generation reduces in essence to the problem of an appropriate generation of *d-q* voltage components (commensurate with the reference voltage space vector) that simultaneously ensure zero resulting space vector in the *x-y* subspace.

Figure 2 can be used to explain why application of large vectors only cannot yield a sinusoidal output voltage. When reference voltages are sinusoidal, the space vector reference contains only *d-q* components (*x-y* components are zero). However, if only large vectors are used to create the desired *d-q* voltages, *x-y* voltage components will inevitably be created as well (each switching combination that gives a large vector in the *d-q* plane gives simultaneously a small vector in the *x-y* plane; thus low-order voltage harmonics, such as the 3rd and the 7th, are generated as well).

Table I. Phase voltage space vectors in the *d-q* plane.

Space vectors	Value of the space vectors
$\underline{v}_{1phase}$ to $\underline{v}_{10phase}$ (large)	$2/5V_{DC}2\cos(\pi/5)\exp(jk\pi/5)$ k = 0,1,2 ….9
$\underline{v}_{11phase}$ to $\underline{v}_{20phase}$ (medium)	$2/5V_{DC}\exp(jk\pi/5)$ k = 0,1,2 ….9
$\underline{v}_{21phase}$ to $\underline{v}_{30phase}$ (small)	$2/5V_{DC}2\cos(2\pi/5)\exp(jk\pi/5)$ k = 0,1,2 ….9
$\underline{v}_{31phase}$ to $\underline{v}_{32phase}$	0

Table II. Phase voltage space vectors in the *x-y* plane.

Space vectors	Value of the space vectors
$\underline{v}_{21phase}$ to $\underline{v}_{30phase}$	$2/5V_{DC}2\cos(\pi/5)\exp(jk\pi/5)$ k = 0,1,2 ….9
$\underline{v}_{11phase}$ to $\underline{v}_{20phase}$	$2/5V_{DC}\exp(jk\pi/5)$ k = 0,1,2 ….9
$\underline{v}_{1phase}$ to $\underline{v}_{10phase}$	$2/5V_{DC}2\cos(2\pi/5)\exp(jk\pi/5)$ k = 0,1,2 ….9
$\underline{v}_{31phase}$ to $\underline{v}_{32phase}$	0

The innermost space vectors of the *d-q* plane are redundant (see [8] for detailed explanation) and are therefore omitted from further discussion. In what follows, the vectors belonging to the middle region are termed medium vectors and the vectors of the outermost region of the *d-q* plane large vectors.

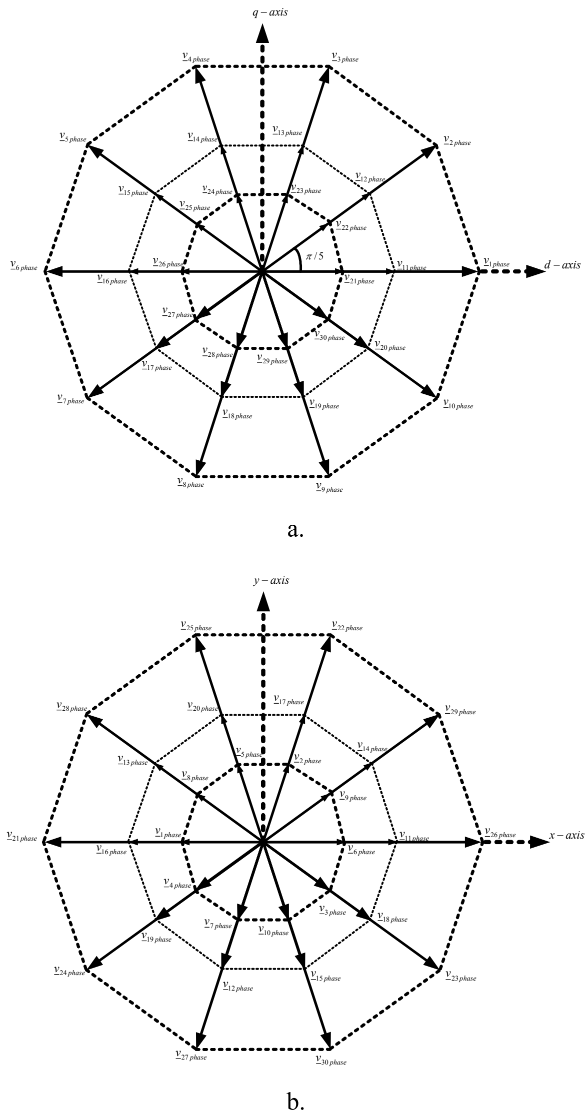

Fig. 2. Five-phase VSI phase voltage space vectors in the: a. *d-q* plane, and b. *x-y* plane.

3. SVPWM FOR SINUSOIDAL OUTPUT VOLTAGE GENERATION

The SVPWM scheme utilises large and medium length space vectors in the *d-q* plane. The input reference voltage vector is synthesised from four active neighbouring (two large and two medium length) and zero space vectors. This is in full compliance with [8], since one needs to apply four active vectors in the case of a five-phase VSI, rather than two. The maximum possible fundamental peak output voltage that can be achieved by using large vectors only ($V_{\max}$) is $V_{\max} = (2/5)2\cos(\pi/5)\cos(\pi/10)V_{DC} = 0.61554 V_{DC}$ [7]. As noted, the application of only large space vectors however produces large unwanted low-order harmonics (the 3rd and the 7th). The SVPWM scheme of this section therefore utilises neighbouring large and the medium space vectors and provides operation with sinusoidal output. Purely sinusoidal output voltages can only be obtained up to a certain value of the reference input voltage, which is smaller than the maximum reference voltage achievable with the large vectors only. Hence this SVPWM scheme is operational for reference voltage values smaller than or equal to the 85.41% of the maximum obtainable fundamental with large vectors only [7]. It has to be noted that full utilisation of the DC bus is simply not possible if the requirement is to maintain the VSI output as sinusoidal.

To calculate the time of application of different vectors, Fig. 3, depicting the position of different available space vectors and the reference vector in the first sector, is considered. The times of active space vector application are from Fig. 3

$$t_a = \frac{\left|\underline{v}_s^*\right| \sin\left(k\pi/5 - \alpha\right)}{\left|\underline{v}_l\right| \sin\left(\pi/5\right)} t_s \tag{4a}$$

$$t_b = \frac{\left|\underline{v}_s^*\right| \sin\left(\alpha - \left(k-1\right)\pi/5\right)}{\left|\underline{v}_l\right| \sin\left(\pi/5\right)} t_s \tag{4b}$$

$$t_o = t_s - t_a - t_b \tag{5}$$

Here k is the sector number (k = 1 to 10), and application times are expressed in terms of the large vector length, which is

$$\left|\underline{v}_{al}\right| = \left|\underline{v}_{bl}\right| = \left|\underline{v}_l\right| = \frac{2}{5} V_{DC}\, 2\cos\left(\pi/5\right) \tag{6a}$$

Corresponding medium vector length is

$$\left|\underline{v}_{am}\right| = \left|\underline{v}_{bm}\right| = \left|\underline{v}_m\right| = \frac{2}{5} V_{DC} \tag{6b}$$

Symbol $\underline{v}_s^*$ denotes the reference space vector, while $\left|\underline{x}\right|$ is the modulus of a complex number $\underline{x}$. Switching period is denoted with t_s and indices *a* and *b* denote the neighbouring space vectors to the right and to the left, respectively, of the reference space vector. Indices *l* and *m* stand for large and medium space vectors, respectively.

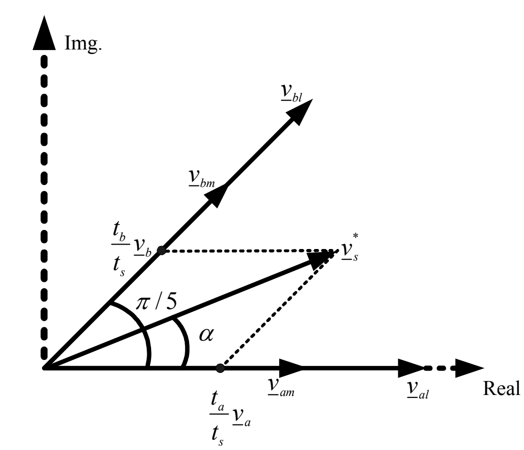

Fig. 3. Principle of time calculation for active space vector application in a five-phase VSI.

For any given reference value and position (shown in the first sector in Fig. 3), projections along the directions of the neighbouring active space vectors are the same, regardless of whether only large or large and medium vectors are used. To achieve sinusoidal output voltage, proportional (to the vector length) subdivision of time of application of large and medium space vectors is utilised.

Consider the SVPWM aimed at generation of the sinusoidal output (i.e. reference values between 0 and 85.41% of the maximum achievable). The total times of application of active space vectors are calculated using (4), where the large vector length has been utilised. In order to subdivide these times into times of application of medium and large vectors, the principle of proportionality is adopted [7]. Subdivision is performed according to the lengths of the medium and large vectors. This subdivision of the time in essence allocates 61.8% of the total time to the large space vectors and 38.2% to the medium space vectors, since the ratio of moduli of the medium to large space vectors in Table I is 38.2%. The times of application of medium and large space vectors are calculated as follows:

$$t_{al} = t_a \frac{|\underline{v}_l|}{|\underline{v}_l| + |\underline{v}_m|} \qquad t_{am} = t_a \frac{|\underline{v}_m|}{|\underline{v}_l| + |\underline{v}_m|} \tag{7a}$$

$$t_{bl} = t_b \frac{|\underline{v}_l|}{|\underline{v}_l| + |\underline{v}_m|} \qquad t_{bm} = t_b \frac{|\underline{v}_m|}{|\underline{v}_l| + |\underline{v}_m|} \tag{7b}$$

while the zero space vector application time is

$$t_o = t_s - t_{al} - t_{am} - t_{bl} - t_{bm} \tag{8}$$

In essence, subdivision of vector application times according to (7) leads to cancellation of the space vector components in the x–y plane, so that operation with sinusoidal output results.

To verify the volt-second principle, the following expression for the first sector is considered

$$|\underline{v}_s^*| t_s e^{j\alpha} = t_{al}|\underline{v}_{al}| + t_{am}|\underline{v}_{am}| + t_{bl}|\underline{v}_{bl}| e^{j\pi/5} + t_{bm}|\underline{v}_{bm}| e^{j\pi/5} \tag{9}$$

After substitution of (7) and (4) into (9) the following relationship is obtained:

$$|\underline{v}_s^*| t_s e^{j\alpha} = \frac{|\underline{v}_l|^2 + |\underline{v}_m|^2}{|\underline{v}_l|\left(|\underline{v}_l| + |\underline{v}_m|\right)} |\underline{v}_s^*| t_s e^{j\alpha} \tag{10}$$

This expression indicates that the output fundamental phase voltages are only 85.41% of the input reference voltage value (this is the value of the coefficient on the right hand side, obtained by replacing the lengths of medium and large vectors from (6) or Table I). Thus in order to obtain the output fundamental equal to the input reference, the reference value should be 17.082% larger than the required output. This means that, for any given reference equal to

$$\underline{v}_s^* = \sqrt{2} V^* e^{j\alpha} \tag{11}$$

the equality of the reference RMS value V* and the fundamental RMS in the output will be ensured if the reference given to the modulator is scaled with the factor 1/0.8541, i.e.,

$$\underline{v}_s^{*\prime} = (1/0.8541)\sqrt{2} V^* e^{j\alpha} \tag{12}$$

Since both medium and large vectors are used and medium vectors are always applied, the maximum output voltage that can be obtained with this SVPWM modulator is 0.5257 p.u. (peak), which is 85.41% of the maximum achievable with large vectors only (0.6155 p.u. peak).

The simulation is performed to obtain the maximum achievable output value (0.5257 p.u. peak), with the scaled commanded input equal to 0.6155 p.u. (according to (12)) of 50 Hz frequency, thus ensuring the equality of the fundamental output magnitude and the reference magnitude. The inverter input DC voltage is set to 1 p.u. and the switching frequency is 5 kHz. The filtered phase voltages and leg voltages are shown in Fig. 4 along with the harmonic spectrum. It can be seen from Fig. 4 that the spectrum contains only fundamental (0.372 p.u. RMS or 0.5257 p.u. peak, 50 Hz) component and harmonics around multiples of the switching frequency. The low-order harmonics (such as the third and the seventh) are completely absent. The output is sinusoidal (except for the PWM ripple) because time subdivision according to (7) is such that it cancels all the undesirable x-y components (as can be seen from Fig. 2). For lower values of the input reference than the one used in production of Fig. 4 the output phase voltages preserve the shape with a corresponding reduction in the amplitude, meaning that the low-order harmonics are absent throughout the operating region of this SVPWM modulator (0 to 0.5257 p.u. peak, or 0 to 85.41% of the maximum achievable output with large vectors only). It should be noted that the SVPWM method of [9] is characterised with an identical behaviour to the method described here, with the difference being in the expressions used to calculate application times for medium and large space vectors.

4. CARRIER-BASED PWM WITH THE FIFTH HARMONIC INJECTION

The third-harmonic injection in the leg voltage references leads to an increase in the linear modulation range of a three-phase VSI [1]. By injecting the third harmonic with amplitude of one-sixth of the fundamental harmonic, the maximum of the fundamental can be increased by 15.47% compared to pure sine-triangle carrier-based scheme, without moving into the over-modulation region. The same concept is applied here to the five-phase VSI. By analogy, the linear modulation range is extended by injecting the fifth harmonic. This increases maximum fundamental output voltage without moving into the over-modulation region. The fifth-harmonic component does not affect the phase output voltages, since the load is star connected with isolated neutral point. The fifth harmonic injection reduces the peak of the leg reference voltages and hence the modulation index can be pushed beyond the value of 1 without entering over-modulation.

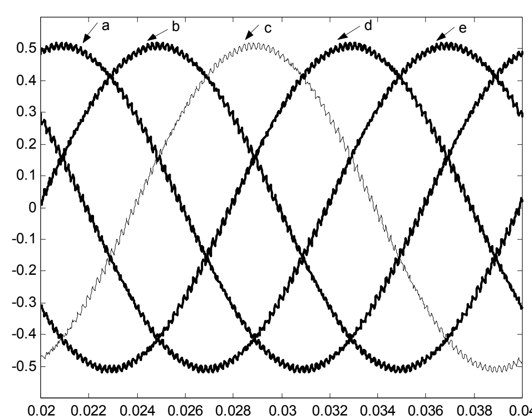

a.

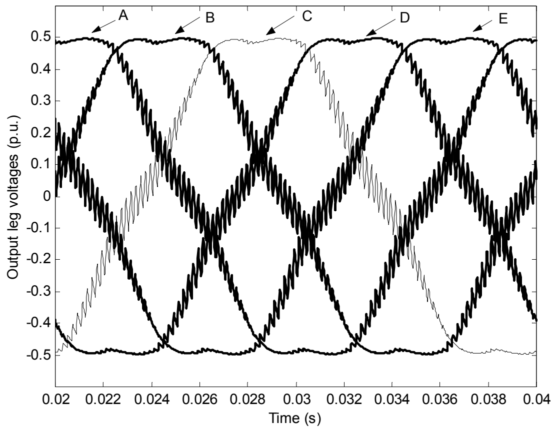

b.

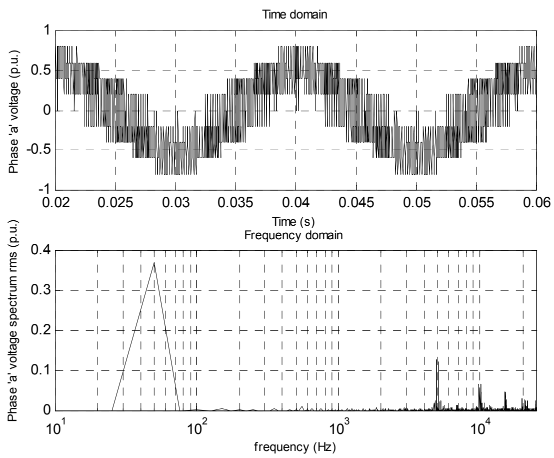

c.

Fig. 4. Output of the inverter for the maximum achievable output fundamental voltage (85.41% of the one obtainable with large vectors only) with SVPWM using proportional subdivision of time for application of medium and large space vectors: a. filtered phase voltages, b. filtered leg voltages, c. full PWM waveform and harmonic spectrum of the phase voltage.

To determine the optimum fifth harmonic injection level the five-phase inverter reference leg voltages are given as

$$\begin{aligned}
v_A^* &= M_1 0.5V_{DC}\cos(\omega t) + M_5 0.5V_{DC}\cos(5\omega t)\\
v_B^* &= M_1 0.5V_{DC}\cos(\omega t - 2\pi/5) + M_5 0.5V_{DC}\cos(5\omega t)\\
v_C^* &= M_1 0.5V_{DC}\cos(\omega t - 4\pi/5) + M_5 0.5V_{DC}\cos(5\omega t)\\
v_D^* &= M_1 0.5V_{DC}\cos(\omega t + 4\pi/5) + M_5 0.5V_{DC}\cos(5\omega t)\\
v_E^* &= M_1 0.5V_{DC}\cos(\omega t + 2\pi/5) + M_5 0.5V_{DC}\cos(5\omega t)
\end{aligned} \tag{13}$$

where M1 and M5 are the modulation indices of the fundamental and the fifth harmonic. Without the 5th harmonic injection linear modulation range is restricted to $0 \le M_1 \le 1$. For sinusoidal carrier-based PWM without harmonic injection the fundamental peak magnitude of the output voltage for M1 = 1 is 0.5VDC.

The fifth harmonic has no effect on the value of the reference leg voltage waveforms (13) when $\omega t = (2k+1)\pi/10$, since $\cos[5(2k+1)\pi/10] = 0$ for odd k. Thus M5 is chosen to make the peak magnitude of the reference (13) occur where the fifth harmonic is at maximum negative value. This ensures the maximum possible value of the fundamental. The reference voltage reaches the maximum when

$$dv_A^*/d(\omega t) = -M_1 0.5V_{DC}\sin(\omega t) - 5M_5 0.5V_{DC}\sin(5\omega t) = 0 \tag{14}$$

From (2) one further has

$$M_5 = -M_1\frac{\sin(\pi/10)}{5} \quad \text{for } \omega t = \pi/10 \tag{15}$$

Thus the maximum modulation index of the fundamental in the linear region can attain the value determinable from

$$\left|v_A^*\right| = \left|M_1 0.5V_{DC}\cos(\omega t) - \frac{\sin(\pi/10)}{5}M_1 0.5V_{DC}\cos(5\omega t)\right| = 0.5V_{DC} \tag{16}$$

This yields

$$M_1 = \frac{1}{\cos(\pi/10)} \quad \text{for } \omega t = \pi/10 \tag{17}$$

Hence the output fundamental voltage may become 5.15% higher than the value obtainable using simple sinusoidal carrier-based PWM. This requires injection of the fifth harmonic with modulation index of (15). The fifth harmonic is, naturally, in phase opposition with respect to the fundamental.

A simulation is performed in order to prove the increase in the maximum fundamental modulation index by this scheme. The DC link voltage is set to 1 p.u. and, at first, the modulation index M1 is set to 1. Next, modulation index for the fundamental is increased to $M_1 = 1/\cos(\pi/10)$, in accordance with (17). In both cases the 5th harmonic is injected, with the modulation index for the 5th harmonic being determined with (15). The switching frequency of the VSI is again 5 kHz and the reference fundamental frequency is kept once more as equal to 50 Hz. The simulation results are depicted in Figs. 5 and 6, respectively.

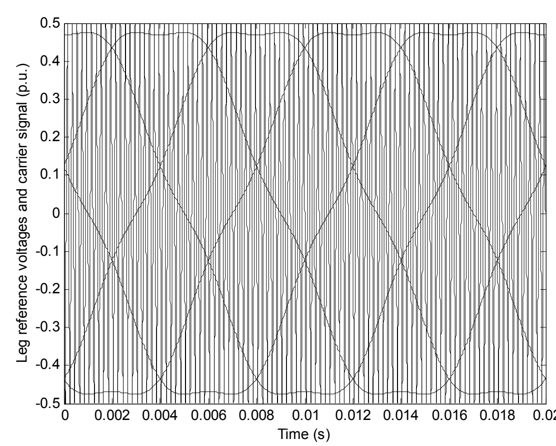

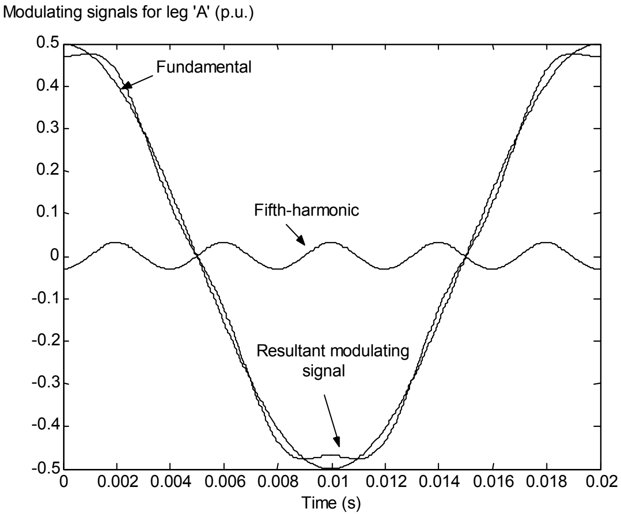

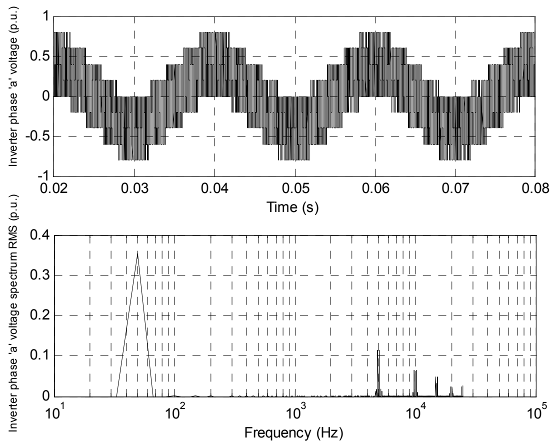

Fig. 5. Leg reference voltages and carrier (top), modulating signal components for leg A (middle), and output phase a voltage and its spectrum for M1 = 1 (bottom).

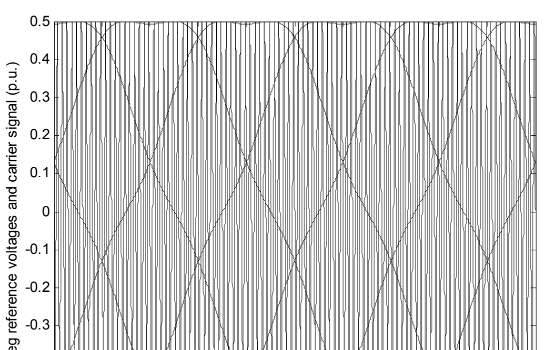

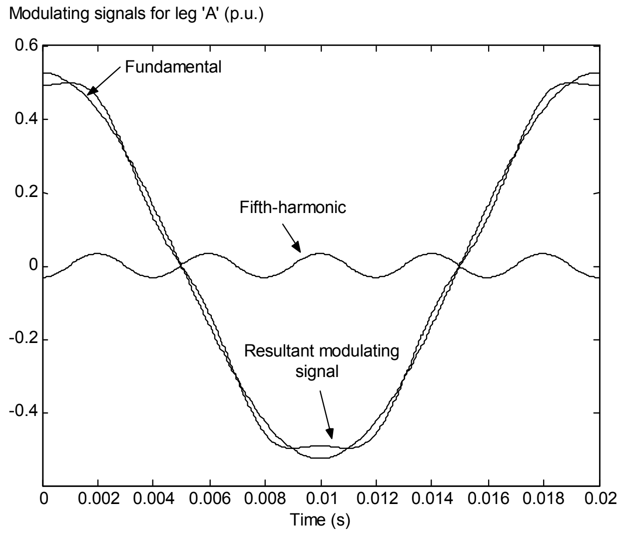

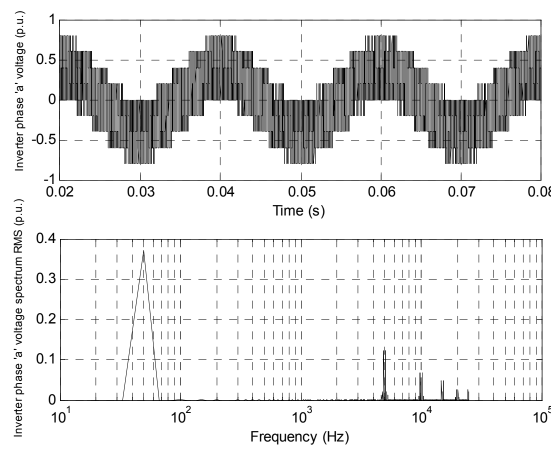

Fig. 6. Leg reference voltages and carrier (top), modulating signal components for leg A (middle), and output phase a voltage and its spectrum for $M_1 = 1/\cos(\pi/10)$ (bottom).

As is evident from the top part of Fig. 5, fundamental modulation index M1 = 1 does not lead to operation in the limit of the linear modulation region. However, when the fundamental modulation index value is set to $M_1 = 1/\cos(\pi/10)$ situation changes and now modulation signals exactly reach the values of ± 0.5 p.u. (top figure in Fig. 6). Composition of the reference signals is illustrated in the middle parts of Figs. 5 and 6. Bottom parts show the output phase a voltage and its spectrum. The spectrum of phase a voltage in Fig. 6 shows that output fundamental rms value equals 0.371 p.u. (0.5257 p.u. peak). In Fig. 5 the corresponding value is only 0.353 p.u. (0.5 p.u. peak). Thus an increase of 5.1% in the maximum fundamental output voltage results by injecting the fifth harmonic. It should be noted that the same maximum fundamental output phase voltage has been obtained using SVPWM in the previous section. Thus the maximum output voltages that can be generated using sinusoidal PWM with fifth harmonic injection and using SVPWM are the same in the linear modulation region. This is an expected results, since the same holds true for the equivalent three-phase PWM schemes [1].

5. CONCLUSION

The paper discusses PWM techniques that may be used in conjunction with a five-phase VSI when the requirement is to produce sinusoidal output voltages. A space vector PWM scheme is presented and it is shown that, by appropriately determining application times of neighboring medium and large length vectors, it becomes possible to achieve the operation with sinusoidal output. Such an operation can be sustained up to the reference voltage value equal to 85.41% of the maximum value obtainable with large vectors only. Hence, if the output is required to be sinusoidal, it is not possible to utilize the DC bus voltage to the limit. Next, a corresponding carrier-based PWM scheme with the fifth harmonic injection is introduced. It is shown that the same quality of performance and the same level of the DC bus utilization are achievable as with the SVPWM. However, since the implementation of the SVPWM requires dedicated calculation of the space vector calculation times, it is believed that the carrier-based scheme offers advantages due to simpler implementation requirements.

REFERENCES

[1] G.D.Holmes, T.A.Lipo, Pulse Width Modulation for Power Converters - Principles and Practice, IEEE Press Series on Power Engineering, John Wiley and Sons, Piscataway, NJ, USA, 2003.

[2] Y.Zhao, T.A.Lipo, Space vector PWM control of dual three-phase induction machine using vector space decomposition, IEEE Trans. on Industry Applications, vol. 31, no. 5, 1995, pp. 1100-1109.

[3] H.Xu, H.A.Toliyat, L.J.Peterson, Five-phase induction motor drives with DSP-based control system, IEEE Trans. on Power Electronics, vol. 17, no. 4, 2002, pp. 524-533.

[4] H.M.Ryu, J.H.Kim, S.K.Sul, Analysis of multi-phase space vector pulse width modulation based on multiple d-q spaces concept, IEEE Trans. on Power Electronics, vol. 20, no. 6, 2005, 1364-1371.

[5] R.Shi, H.A.Toliyat, Vector control of five-phase synchronous reluctance motor with space vector pulse width modulation (SVPWM) for minimum switching losses, Proc. IEEE Applied Power Elec. Conf. APEC, Dallas, Texas, 2002, pp. 57-63.

[6] H.A.Toliyat, R.Shi, H.Xu, DSP-based vector control of five-phase synchronous reluctance motor, IEEE Industry Applications Society Annual Meeting IAS, Rome, Italy, 2000, CD-ROM Paper 40_05.

[7] A.Iqbal, E.Levi, Space vector PWM techniques for sinusoidal output voltage generation with a five-phase voltage source inverter, Electric Power Components and Systems, vol. 34, no. 2, 2006, pp. 119-140.

[8] J.W.Kelly, E.G.Strangas, J.M.Miller, Multi-phase space vector pulse width modulation, IEEE Trans. on Energy Conversion, vol. 18, no. 2, 2003, pp. 259-264.

[9] P.S.N.deSilva, J.E.Fletcher, B.W.Williams, Development of space vector modulation strategies for five-phase voltage source inverters, Proc. IEE Power Electronics, Machines and Drives Conf. PEMD, Edinburgh, UK, 2004, pp. 650-655.

[10] O.Ojo, G.Dong, Generalized discontinuous carrier-based PWM modulation scheme for multi-phase converter-machine systems, Proc. IEEE Ind. Appl. Soc. Annual Meeting IAS, Hong Kong, 2005, CD-ROM paper no. 38P3.

ACKNOWLEDGEMENT

The author acknowledges financial support provided by the EPSRC (standard research grant EP/C007395), Semikron Ltd – UK, MOOG – Italy and Verteco – Finland.

TRENDS IN AC DRIVE APPLICATIONS

Victor R. Stefanovic

Abstract - *As the technology of AC drives developed and matured, new applications are emerging. This paper looks at the application segments and evaluates drive growth potential for each of them. Drive characteristics which are critical for each application segment are identified and technical solutions are discussed.*

Key words: *Motor Drives, Power Converters*

1. INDTRODUCTION

AC drives were traditionally first applied in process industries, such as cement, plastic, textile, etc. With development of various vector control methods, AC drives started also to replace DC drives in industries requiring high precision of speed control and good dynamic performance, such as machine tools, robotics, metal rolling, paper mill finishing lines, etc. These are all applications which must have adjustable speed, by the nature of the process. Induction motors are predominantly used, although at power below 10 KW, PM motors have been preferred in servo applications. That application has had spectacular growth over the last 20 years. For example, over that period, one manufacturer has approximately halved the time period for sale of each subsequent million units: from 9 years for the first million, 1984-1993, to two years for the 4th million[1]. However, because AC drive penetration into these applications is almost 100%, (adjustable speed drives are provided to all applications where the speed has to be regulated), the future growth in this application segment is expected to essentially track the growth of the corresponding industries.

The second market segment has been slowly developing over the last 15 – 20 years and consists of drive applications to fans, pumps and compressors. (This market is sometimes referred to as Heating, Ventilation and Air Conditioning, or HVAC, although fan and pump applications are found also in process industries and power plants). The fluid flow in these applications can be achieved also using mechanical devices, so that a switch to AC drives is based primarily on the resultant energy savings. Depending on economic situation and the prevailing interest rates, a decision to use AC drives is normally made (in the USA) if the investment can be recovered through energy savings in 1.5 – 2 years. This has been almost exclusively a retrofit market, where the already installed induction motors are retrofitted with AC drives. However, more recently, new installations start with AC drives, sometimes opening an opportunity for a new motor selection.

Aside from some niche applications, these two segments account for a vast majority of AC drives sold presently, especially in the USA, where the railway applications for fast trains play much smaller part then in Europe and Japan. Table 1 [2] gives an indication of the size and growth of the low voltage AC drive market over the last 11 years. (The values are approximate, due to the fluctuating currency exchange rates).

The biggest change in the application of AC drives will come from development of large consumer markets for products which incorporate AC drives. That market has been already growing in Japan, specifically in residential heat pumps, where out of the total market of 7 million units, (year 2000) 94% were with inverter control. The second, even larger world-wide consumer market for AC drives is in hybrid electric vehicles, an application again pioneered in Japan. Thus, we are at a threshold of consumer applications, with a very large growth potential and significantly different requirements then industrial applications of 5-20 years ago.

Table 1: World market growth of low-voltage adjustable speed drives bellow 160 KW[2] in billions of dollars.

Market	1991	2002	Annual Growth
Europe	0.616	1.512	~7.7%
North America	0.560	1.008	~5.0%
Japan	0.686	1.022	~3.4%
Rest of World	0.378	1.344	~11.1%
Total	2.24	4.886	~6.7%

This paper presents a brief survey of the state of the art of present industrial drives and then examines the required characteristics of the AC drives in the two consumer markets.

2. STATE OF THE ART, CURRENT INDUSTRIAL AC DRIVES

Many good papers [2]-[4] have been recently written on the future of adjustable speed drives, so only some salient aspects and new points will be discussed here. More important, still outstanding application problems will be also considered.

The spectacular growth of AC drives over the last 10 - 15 years, coupled with a parallel reduction in their price reflects the maturation and stabilization of that industry. The last significant technology changes were conversion to IGBT power devices and digital control about 15-18 years ago. Current low voltage (to 575 V) AC drives have now standardized on a diode rectifier - DC link - IGBT PWM inverter topology. Power devices are used without snubbers; control is μP or DSP implemented, significantly increasing drive functionality and features. (In fact, the transfer of functionality from hardware to software not only resulted in application flexibility, but also contributed to reduction in drive size and cost and increase in drive reliability.

Although the drive technology is becoming mature, the development continues, mostly directed to some form of cost reduction. Some of the most important current trends in low voltage AC drives are:

Continuing expansion of various forms of sensorless vector control to General Purpose (GP) drives, replacing previous V/Hz control (with or without slip compensation). The main reasons for this change are increasing performance requirements of GP drives, which still do not need servo grade characteristics and need for improved efficiency, resulting from better motor flux control. Current performance allows for ±10% torque regulation accuracy [5]. This trend will continue, as new research results are transferring to industry, eventually permitting a position sensorless control [6].

1. Continued inclusion of PLC functionality in drives, further increasing the drive application flexibility in process automation.
2. Continued development of motors with integrated power electronics [7]-[8], increasing the rated power from less then 10 HP to several hundred HP. The three main reasons for integrating electronics in the motor are reduced wiring, contained electro-magnetic interference (EMI) and easier application. One such motor for servo applications is shown in Fig. 1.
3. Gradual commercial justification of PWM controlled rectifiers, which help meet the current harmonic standards, EN-61000-3-2 in Europe and IEEE-519 in the USA, with smaller filters then those needed with diode rectifiers. The introduction of PWM rectifiers may permit elimination or a drastic reduction of the electrolytic DC link capacitors [9]-[10], thus improving the drive reliability while reducing its size.
4. Introduction of liquid cooled drives, with closed-circuit for (typically) de-ionized water being either part of the drive, or drive having a cold plate, which is cooled by cabinet installed liquid cooling. The obvious objective is to reduce the drive size, saving some of the precious cabinet space. The same trend towards reduced foot print can be also seen in packaged drives, which are taking the shape similar to servo drives [5].
5. Continued transition from fixed to floating point DSPs, permitting higher flexibility, faster software developments and easier maintenance.
6. Use of direct drives with linear motors in various machine tool applications, having traverse speeds exceeding 0.5 - 1.0 m/sec. (This is considered to be the limiting speed for ball screw coupling). Direct drives offer also reduced speed ripple and better precision. On the other hand, with a direct drive, one loses the benefit of gearing and torque multiplication, requiring a larger motor for a given final output torque. An example of a linear PM motor is shown in Fig. 2.

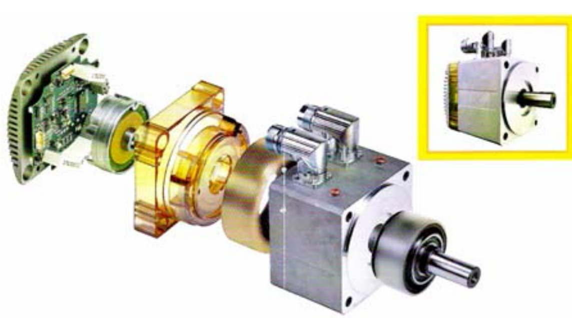

Fig. 1: Example of a servo motor with integrated electronics, containing inverter, 16-bit absolute encoder, communication, RFI filter, etc. The motor develops 2.5 – 6 Nm, 3000 RPM. The yellow piece provides a temperature shield between motor and \electronics. Courtesy of Phase Motion Control S.r.l

Expansion of the application range of PM motors to much higher power, as high as 500 hp. The main reason for this trend is dramatically reduced motor size and a significant increase in its efficiency. The motor size is further reduced by liquid cooling of the motor. The price difference compared to induction motors is smaller then expected and is often justified by better PM motor characteristics. Table 2 shows representative efficiency, power/weight and power density numbers for large PM and high efficiency induction motors. Figures 3-5 show representative large PM motors.

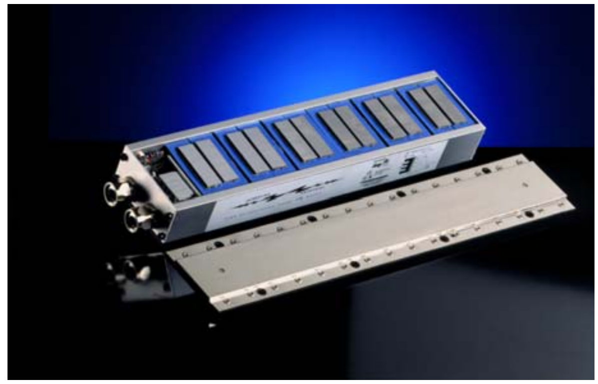

Fig. 2: Linear PM motor, with continuous trust of 400 N, peak trust of 1000 N, speed of 5 m/sec, for Cartesian robot applications. Courtesy of Phase Motion Control S.r.l

Table 2: Representative motor characteristics

Power Range 100-500 HP	Efficienc y	HP/in^3	HP/lb
PM motors	95 - 98%	0.15–0.2	1.5 – 1.7
Induction motors	90 – 93%	0.05–0.08	0.21 - 0.44

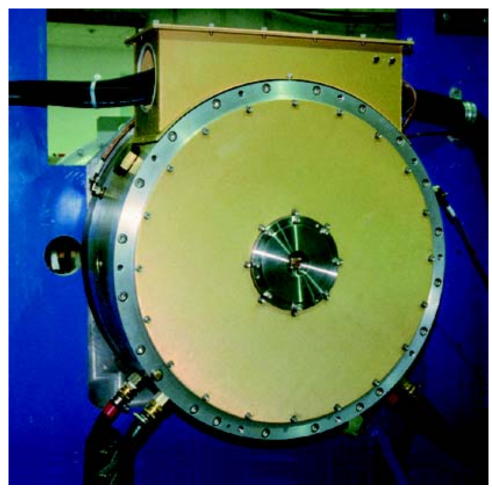

Fig. 3 1000 HP, liquid cooled PM motor, 96% efficiency, 4,000 RPM, 36 poles, 780 lb, continuous torque at stall: 2660 N-m. Courtesy of DRS Electric Power Technologies, Inc.

Fig. 4: 450 HP, axial flux, liquid cooled PM motor, with 28 poles, maximum speed of 3600 RPM, 2000 Nm continuous torque at stall, 395 lb, 95% efficiency. Courtesy of DRS Electric Power Technologies, Inc.

Fig. 5: 500 HP PM motor, introduced as competition to induction motors, with clearly visible liquid cooling connection points. It has 20 poles, 95% efficiency and weights 500 lb. Courtesy of DRS Electric Power Technologies, Inc.

The large PM motors (such as those shown here) are typically used in applications requiring high torque, especially at low speed, compact size or high efficiency. This means high torque vehicle drives, mining, large air-conditioning compressors, oil and gas drilling, mobile generators, cranes, wind turbine generators, etc. On the other hand, the PM motors either need a shaft position sensor or sensorless control, which usually cannot provide the full available torque at standstill.

Remaining Problems

Although AC drives have evolved to advanced level of maturity and although their acceptance is universal, there are still technical problems which hinder drive applications. Three most important problems are listed here, in descending order of importance:

1. Motor bearing and insulation problems.

These problems, as well as some of the solutions have been well documented (11-16). While the failure mechanism is complex, the winding insulation problem is essentially, caused by fast IGBT switchings (high dv/dt) and long motor cables, while the bearing failures are caused by high dv/dt, capacitive coupling between stator and rotor and high frequency common mode voltages. Of these two, insulation problem is much better understood and can be normally solved. The bearing problem is much more complex and is still a cause of significant number of motor failures, impacting the drive reliability. It is interesting that PM motors do not show bearing failure problem, possibly because of the large equivalent air-gap and thus weak stator-rotor capacitive coupling.

2. EMI and line-side harmonics.

Although very much related, these two phenomena are not identical. EMI includes not only line harmonics, but also the effects of inverter switching and specifically differential and common mode noise. These problems have been also well documented (17-20). Their solutions are also well known, especially regarding line harmonics and involve either filters or PWM rectification with some high frequency filtering. While still more expensive, the PWM rectification is gradually becoming almost competitive with the traditional diode bridge solution at powers bellow ~100 KVA. But, either solution lowers the drive efficiency [2]. The EMI is more difficult to control, especially in common mode and knowledgeable selection and placement of filters becomes very important [18].

2. Acoustic noise.

The availability of fast IGBTs has almost solved the noise problem, as the switching frequency is pushed outside of the audio range. In cases where this is not practical, the alternate approach is to vary the switching frequency over each fundamental cycle [21], so that the acoustic energy is spread over the frequency spectrum, creating a form of “white noise”. In both cases, the price for reducing the acoustic noise is also reduced drive efficiency.

3. CONSUMER APPLICATIONS

Two most significant applications of AC drives to consumer products are in residential heat pumps and in passenger automobiles. Both markets are huge and their full development will affect also the technology of industrial AC drives. In Japan, the inverter driven residential heat pumps represent already a mature product [20]. In fact, 94% of all heat pumps sold in Japan in a year 2000 had an inverter. Table 3 gives the evolution of the use of adjustable speed drives in Japanese heat pumps [20], showing already a mature market. In a process of increasing the market share of inverter driven pumps, significant advances were made in reducing the EMI, the acoustic noise and above everything the inverter cost, while increasing the inverter reliability.

Table 3: Residential heat-pump units sold in Japan with percentage of those with an inverter drive.

YEAR	HEAT PUMP UNITS SOLD IN JAPAN (MILLIONS)	% HAVING INVERTER DRIVE
1990	6.1	45%
1991	7.0	55%
1992	6.0	61%
1993	5.1	60%
1994	7.1	60%
1995	7.7	68%
1996	7.9	72%
1997	7.0	75%
1998	6.6	91%
1999	6.6	95%
2000	7.0	94%

There are several reasons which explain why Europe and America have not followed the Japanese trend in use of variable speed heat pumps. One is that both have, in general, less temperate climate then Japan and that heat pumps are not so widely accepted, as in Japan. Another one is that the power rating of central air-conditioning in the USA is several times higher then the rating of split systems typically used in Japan, so that the inverter cost is also much higher. Yet another reason is that the energy cost in the USA is lower then in Japan,reducing the incentive to switch to inverter driven compressors. One could continue listing these reasons, not all of which are convincingly valid. Hopefully, with changing economic conditions, the rest of the world may start to enjoy the same comfort offered by inverter driven heat pumps.

The use of inverter driven motors in the automotive applications was also pioneered in Japan, but that trend is spreading throughout the world. From drive design point of view, the main challenge is to provide the required drive reliability in the presence of extreme temperature changes and vibrations. That reliability has to be an order of magnitude greater then the reliability of standard industrial drives, currently around 0.5 – 1%. The system challenge is to control the drive EMI so that the inverter operation is not a source of noise disturbance. But the overall challenge is to reduce the drive cost, so that the premium for hybrid vehicles becomes acceptable. (The increasing fuel prices are helping there!)

The approach in the USA is a little different then in Japan, to the extend that the hybrid systems have been first developed for buses and heavy vehicles, with hybrid passenger cars being introduced now and over the next 2 years. Fig. 6 shows 5th generation inverter package, developed for hybrid buses. The inverter operates with 5 KHz switching frequency and provides vector control to an induction motor. The communication is via CAN bus, SAE J1939 protocol. The unit's weight is 135 lbs, the water flow is 15lpm@70^{0}C, the input DC voltage can vary between 500 and 900 V and the total losses are about 7 KW. The package is designed to withstand continuous vibrations with 5g and momentary shocks of 40g. With the cover removed, the package from Fig. 6 is shown in Fig. 7. The control and signal electronics are on the bottom of the package, as shown in Fig. 8. The inverter package shown in Fig. 6 is also used with fuel cell powered buses, Fig. 9, which shows the inverter placement, providing an idea about the environmental conditions. (The inverter is exposed to splashing from the road and has to be adequately packaged). The inverter of Fig. 6 represents the current technology, the development of which started in 1991 with a DC chopper drive. Over 1000 units were supplied during that period. The key problems solved over that period were reduction of the inverter package size (essentially by going from air to liquid cooling), protection from the environmental conditions (by providing IP 67 package) and containment of the generated EMI, coming primarily from the inverter-motor connection cables.

Fig. 6: 220 KW water cooled inverter drive for hybrid buses, using induction motor. Control and signal connection is at the bottom (square covers). The cooling water is supplied through the two yellow connectors. On the top are three motor connectors, two (black), connectors for external braking resistor and two connectors for ± DC link. Courtesy of Saminco, Inc.

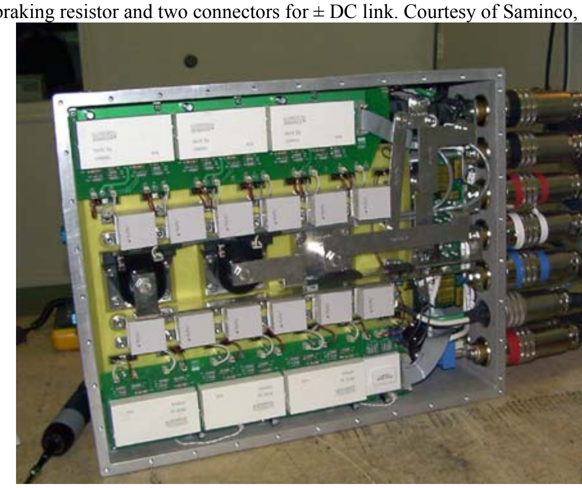

Fig. 7: The inverter package shown in Fig. 6, with the top cover removed. The connecting cables are visible on the far right. Courtesy of Saminco, Inc.

Based on the gained experience, this manufacturer is planning for the 6th generation to have inverter integrated with the motor, thus eliminating the power cables. It is interesting that the new Ford Escape, which offers a hybrid solution and which became available at the end of 2004, also has the drive integrated with the motor, giving elimination of cables and HV connectors as the main reason [23].

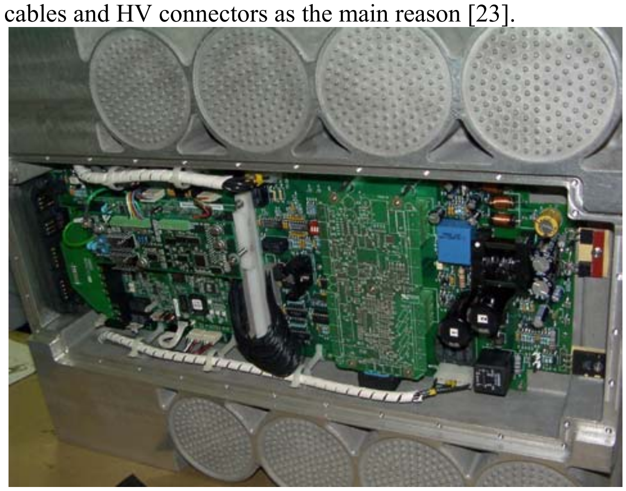

Fig. 8: The bottom side of the package shown in Fig. 6, with the cover removed. The capacitor cooling bays are on the top and the bottom of the photo. Courtesy of Saminco, Inc.

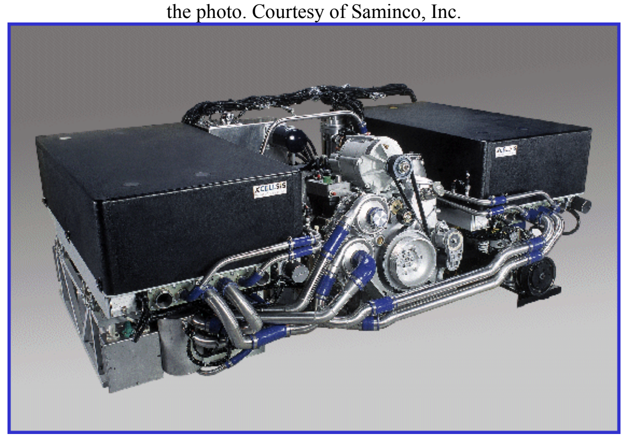

Fig. 9: Fuel cell drive for an all electric bus. The fuel cells are in two black boxes on the top. The inverter package (Fig. 6) is below the black box on the left. The oil-cooled motor is to the right of the inverter, exactly were the Diesel engine would be. Courtesy of Saminco, Inc.

Table 4: An overview of current programs and introduction dates of hybrid passenger cars using split architecture. (Courtesy of J-N-J Miller Design Services)

Introduct. Date	Company	Hybrid Brand	Vehicle Segment	Engine Power, kWpk	Power Split Type	M/G1 rating, kWpk	M/G2 rating, kWpk	System voltage, V	Electric Fraction, Ef
2000	Toyota	Prius-I	car	53	I	10	30	288	0.36
2004	Toyota	Prius-II	car	57	I	30	50	500	0.47
2005	Toyota	RX400H	Lt-SUV	100	I	35	60	500	0.38
2005	Toyota	Highlander	F-SUV	100	I	35	60	650	0.38
2004	Ford	Escape	Lt-SUV	98	I	45	70	300	0.42
2006	Mercury	Mariner	Lt-SUV	98	I	45	70	300	0.42
2007	Mazda	Tribute	Lt-SUV	98	I	45	70	300	0.42
2008	Ford	Fusion	Lt-SUV	98	I	45	70	300	0.42
2007	GM-DCX	Tahoe	F-SUV	164	C	60	60	300	0.27
2007	GM-DCX	Yukon	F-SUV	164	C	60	60	300	0.27
2008	GM-DCX	Durango	F-SUV	164	C	60	60	300	0.27
2008	GM-DCX	Mercedes	F-SUV	164	C	60	60	300	0.27
2006	Nissan	Altima	Car	57	I	30	50	500	0.47
?	FAW	THS-II	car	57	I	30	50	500	0.47
2007	Porsche	Cayenne	Lt-SUV						

Highlighted data: vehicle is in the market and ratings are published.
Non-highlighted data: vehicle introductions are published, but ratings are not.
FAW=First Auto Works, China GM-DCX=GM-Daimler Chrysler joint venture
Legend:
I Input split system. This is the Toyota power split of the single planetary gear type.
C Compound split system. This is the GM (Allison) power split of the double planetary gear type.
Ef Electric fraction = Peak M/G power/(Peak M/G power + Peak ICE power)

Table compiled by J-N-J Miller Design Services, from available public data or using engineering approximations

Table 4 [24] shows an overview of the hybrid vehicle programs of the world's main automotive manufacturers. (Table 4 addresses only vehicles with split hybrid architecture. For that reason, Honda, which uses parallel architecture, is not shown in Table 4).

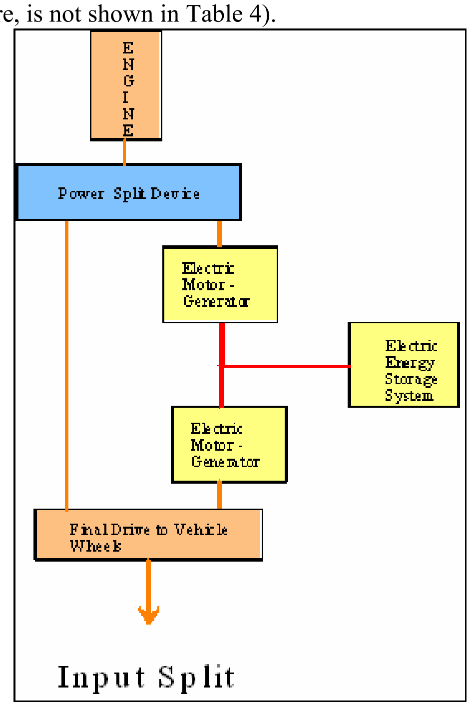

Fig. 10: Schematic diagram of an input split hybrid system [24].

Fig. 10 illustrates the input split system, characterized by having the engine power as input to the power split device, which is normally a planetary gear. Essentially, the speed and torque of the electric motor determine the mechanical output from the planetary gear. The result is that the engine operates at essentially constant speed, while the torque transmitted to the wheels is regulated by the speed of the electric motor.

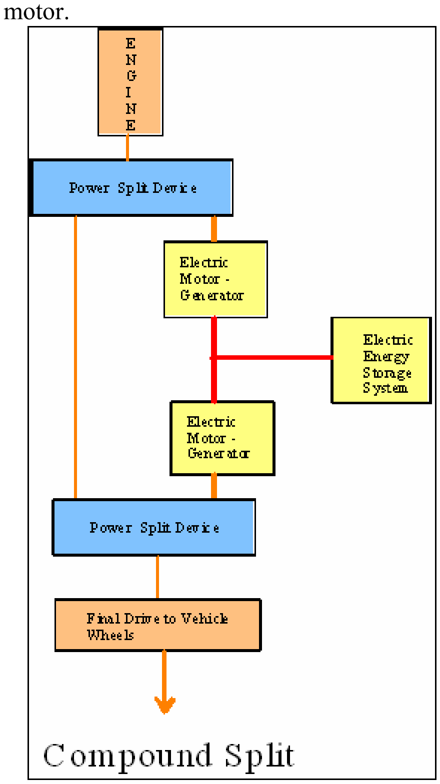

Fig. 11:Schematic diagram of a compound hybrid split system [24].

Fig. 11 shows the concept of the compound split, which is characterized by having the engine power as the input to the first power split device AND output to the wheels is via the second power split device. This architecture, developed by GM offers added flexibility in selecting modes of hybrid operation.

4. CONCLUSION

The market for AC drives is expanding as the result of improvements in drive reliability, reduction in drive cost, ease of operation and enhanced functionality. While the traditional, industry applications of AC drives are showing a robust growth, the main expansion over the next 5-10 years will come from use of AC drives in consumer products, primarily inverter driven heat pumps and fuel cell/hybrid vehicles. Development of these applications is already influencing, by the sheer volume of the drives used, the development, integration and cost of the components used in the industrial drives. At the same time, the requirement for increased power/volume in automotive drives is helping develop liquid cooled industrial drives and motors.

This paper showed some of the technical trends in both traditional, industrial applications and in hybrid vehicles. While there are still a few of technical problems remaining, the main trust in the future development of AC drives will be reduction in cost and further improvements in reliability, both being driven by the consumer market. On a system level, selection of the best architecture for integration of a drive and internal combustion engine into a hybrid vehicle is an on-going process, where the consensus on the best solution may be reached over the next 5-10 years.

REFERENCES

[1] www.yaskawa.co.jp/en/ >AC Servo Shipments

[2] F. Blaabjerg and P. Thoegersen: “Adjustable Speed Drives – Future Challenges and Applications” Proceedings of the 4th International Power Electronics and Motion Control Conference, August 2004, Xi’an, China.

[3] R.J. Kerkman, G.L. Skibinski, D.W. Schlegel. "AC Drives: Year 2000 (Y2K) and Beyond". Proc. of IEEE-APEC '99, Vol. 1, 1999, pp. 28-39.

[4] T.M. Jahns, E.L. Owen. "AC Adjustable-Speed Drives at the Millennium: How did we get here?" IEEE Trans. on Power Electronics, Vol. 16, No. 1, 2001, pp. 17-25.

[5] www.danfoss.com/BusinessAreas/Drives Solutions/ >products>frequency converters > VLT®5000 FLUX

[6] Joachim Holtz and Juntao Quan: ”Drift- and parameter-compensated flux estimator for persistent zero-stator-frequency operation of sensorless-controlled induction motors” IEEE Trans.-IA Jul-Aug 2003 pp.1052-1060

[7] www.danfoss.com/BusinessAreas/DrivesSolutions/ >products>frequency converters>low power modules

[8] www.phase.it/eng/index.html> ultract TW

[9] P.D. Ziogas, Y.G. Kang and V.R. Stefanovic: "Rectifier Inverter Frequency Changers with Suppressed DC Link Components," IEEE-IAS Trans. Vol. IA-22, No. 6, Nov./Dec. 1986, pp. 1027-1036.

[10] I. Takahashi and Y. Itoh: “Electrolytic Capacitor-less PWM Inverter”, IPEC 1990, Tokyo, pp. 131 – 138.

[11] Austin H. Bonnet: “Analysis of the impact of pulse-width modulated inverter voltage waveforms on AC induction motors”; IEEE Trans-IA Mar/Apr. 1996 pp.386-392

[12] J. Erdman, R.J. Kerkman, D. Schlegel, G. Skibinski: “Effect of PWM Inverters on AC Motor Bearing Currents and Shaft Voltages”; IEEE Trans-IA Mar/Apr. 1996 pp. 250-259.

[13] D. Busse, J. Erdman, R.J. Kerkman, D. Schlegel, and G. Skibinski: “Bearing Currents and Their Relationship to PWM Drives”; IEEE Trans. on Power Electronics, March 1997, pp. 243 – 252.

[14] R.Kerkman, D.Leggate, G.Skibinski: “Interaction of Drive Modulation & Cable Parameters on AC Motor Transients”; IEEE Trans.-IA May-June 1997, pp. 722-731

[15] D.Rendusara, P.Enjeti: “An Improved Inverter Output Filter Configuration Reduces Common and Differential Modes dv/dt at the Motor Terminals in PWM Drive Systems”; IEEE Trans. on Power Electronics, November 1998, pp. 1135-1143

[16] S. Bhattacharya, L. Resta, D.M. Divan, D.W. Novotny, T.A. Lipo: “Experimental Comparison of Motor Bearing Currents with PWM Hard and Soft Switched Voltage Source Inverters”; IEEE PESC 1996

[17] Y. Murai, T. Kubota and Y. Kawase: ”Leakage Current Reduction for a High-Frequency Carrier Inverter Feeding an Induction Motor”; IEEE Trans.-IA, July/August 1992, pp. 858 – 863.

[18] E. Zhong and T. Lipo: “Improvements in EMC Performance of Inverter-Fed Motor drives” IEEE Trans.-IA, Nov./Dec. 1995, pp. 1247 – 1256.

[19] S. Ogasawara, H. Akagi: ”Modeling and Damping of High-Frequency Leakage Currents in PWM Inverter-Fed AC Motor Drive Systems”; IEEE Trans.-IA Sept./Oct. 1996, pp. 1105 – 1114.

[20] S. Ogasawara, H. Ayano and H. Akagi: ”Measurement and Reduction of EMI Radiated by a PWM Inverter-Fed AC Motor Drive System”; IEEE Trans.-IA Jul/Aug 1997, pp. 1019-1026.

[21] A. Trzynadlowski, S. Legowski and R. Kirlin: “Random Pulse Width Modulation Technique for Voltage-Controlled Power Inverters” Conf. Rec. IEEE-IAS 1987, pp. 863-868.

[22] A. Hiruma, H. Kanazawa, T. Uchida and Y. Yamanashi: “Inverter Air-Conditioner in Japan”, Conf. Record, PCIM 2003, P.R. China.

[23] A. Sankaran: “Introducing Power Electronics in Ford Hybrid Escape Vehicle”, Power Electronics Society Newsletter, Vol. 16, No. 3, 2004.

[24] Communication with John Miller, J-N-J Miller Design Services.

ON –LINE RESOLUTION SWITCHING OF THE RESOLVER TO DIGITAL CONVERTER WITHIN A POSITIONING SERVO DRIVE COMPRISING SIMULATED ENCODER

Slobodan N. Vukosavić

Abstract: *The paper deals with the position and speed sensing in an environment of industrial servo drives equipped with resolver-type sensors. Problems of limited R/D converter resolution are outlined along with their influence on overall drive performance. Novice method for on-line R/D resolution change is proposed, and its software and hardware aspects are thoroughly examined. Primarily software based, proposed approach adapts the R/D resolution according to current shaft speed, so as to reduce the noise in feedback signals and optimize the drive performance. Experimentally verified, the method is proposed to potential users in the form of clear design guidelines.*

Keywords: *Resolver-to-Digital Converter, Servo Drive*

1. INTRODUCTION:

Advanced servo drives with synchronous and induction motors demand high precision shaft sensors for the speed and the position measurement. Harsh industrial environment might include elevated temperatures, dust, oil vapors, noise and vibration that prevent the use of common optical transducers. When highly reliable operation in a severe environment is required, the shaft sensor commonly used is the robust electromagnetic resolver.

Resolver *sine* and *cosine* signals contain the information on the shaft position in an analog form. Ratiometric resolver to digital (R/D) converters are used for transforming the shaft position data in digital form, suitable for further processing. The resolution of conversion process might be preset from 10 to 16-bit with most of available R/D chips available on the market. High resolution gives the best precision of the position measurement and the lowest speed feedback ripple. Though, due to the finite topmost frequency of the VCOs and counters comprised within a R/D IC, the maximum shaft speed practicable in high resolution mode is limited. Hence, as the top speed of the drive increases, a lower R/D resolution must be preset, resulting in lower overall drive performance.

The drive performance might be significantly increased with variable resolution scheme, allowing the R/D converter's resolution to be adapted to the current shaft speed. In this paper, the method and application of novice, software implemented R/D resolution switching is proposed. Basic analytical consideration and design guidelines are accompanied with experimental results, illustrating clearly visible improvement of overall drive performance.

2. R/D CONVERTER OPERATION WITH FIXED RESOLUTION:

Resolver-to-digital converters obtain the digital word related to the shaft position from analog signals coming from the *SINE* and *COSINE* detection windings of the resolver. Conversion process is ratiometric [1], and involves closed loop position tracking. Assumed position is present in an UP/DOWN counter (Fig.1) in the form of a digital word with 10, 12 14 or 16 bits. Resolver is normally excited by a low power, high frequency signal [2], having the frequency at least an order of magnitude higher than required bandwidth of the R/D tracking loop. Resistive network in Fig. 1 switches in and out internal resistors according to the status of corresponding counter bits. At its analog input, resistive net is connected to the *sine* and the *cosine* signals, obtained from the resolver detection windings. The net is arranged in such a way that an AC-error signal appears at the output. The error signal is proportional to the difference between the actual shaft position and the estimation contained as a word within the counter.

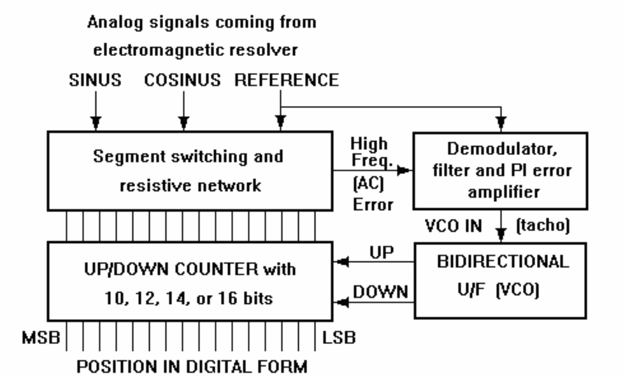

Fig. 1: Basic operation of the R/D converter with fixed resolution

High (excitation) frequency AC error is filtered demodulated, and processed through a PI (proportional - integral gain) block. Amplified error is used as the driving signal for a Bi-directional Voltage Controlled Oscillator; the BVCO generates the pulses at the "UP" output for positive values of VCO_IN signal (see Fig. 1); or, alternatively at the "DOWN" output in the cases whence the VCO_IN has a negative value. In both cases, the pulse frequency varies with the absolute value of the input signal. The BVCO is mostly [1] implemented as current controlled device.

The tracking loop is closed by feeding the BVCO output signals to the counter, providing for corrective action that forces the digital position estimate to track the actual shaft position. "UP" and "DOWN" pulses from the BVCO will increment or decrement the counter attempting to zero the error. The frequency of BVCO output is proportional to the rate of change of the shaft position, and hence, proportional to the shaft speed. The same way, the input to BVCO may be used as an analog representation of the shaft speed; the "tacho" signal.

Most of resolver-to-digital converters available [1] comprise a BVCO with the maximum pulse frequency below f_{max} = 1 MHz. Hence, the R/D converter will not be able to track the shaft position at a speed higher than ω_{max}[rps] = f_{max} [Hz] / 2^N; where N stands for the counter length in bits, and the $\square_{max}$ designates the top speed in revolutions per second, assuming that resolver has one pair of poles.

Generally, the top mechanical speed is obtained by dividing the value ω_{max} by the number of resolver pole pairs. The counter lenght *N* determines the resolution of the R/D converter, and might assume values of 10, 12, 14 or 16.

The best precision of the position measurement is obtained having *N*=16. In this case, full counter lenght is used (from b15=MSB to b0=LSB), the BVCO pulses affect the bits starting with b0, and the top speed $\square_{max}$ is very small (example: with *N*=16, f_{max} = 1 Mhz and a 6-pole resolver, n_{max} = 305 [rpm]). In order to achieve higher speed, the R/D resolution has to be decreased to 14, 12 or 10, depending on the application requirements. For *N*=10, the resolution is at the minimum and the top shaft speed is n_{max}= 19531 [rpm] for 6-pole resolvers, and 58593 [rpm] for 2-pole devices. The BVCO clocking pulses do not affect six least significant bits within the 16-bit counter (b5-b0). The effect of one pulse is addition/subtraction of one (1) to/from a 10-bit digital word consisting of the bits b15..b6.

Accuracy and response speed of the tracking loop depends upon the excitation frequency, resistive net accuracy, the PI error gains and the counter lenght (10 - 16 bits). Generally, tracking loop bandwidth of the order of one tenth the excitation frequency may easily be achieved. The counter length *N* is preset by the user; two dedicated pins of the R/D chip has to be connected to logical 0 or pulled up to logical 1. Four possible combination will set *N* to 10,12, 14 or 16. Along the drive operation, the resolution remains fixed.

The resolution of position measurement is directly determined by the counter length. Hence, it varies from $2^{-10} * 2\pi$ to $2^{-16} * 2\pi$. The speed signal is most frequently obtained from the position information by means of a speed observer. Due to the fact that the speed observers intrinsically bring in the differentiation and filtering of the position signal, the speed feedback noise will increase as the R/D resolution decreases. Consequently, lower R/D resolution will limit the speed loop bandwidth, since the gains of the loop must be reduced due to the noise contained in the feedback signal.

Plenty of servo drive applications require both high precision at a low speed and the possibility to reach very high speed with lower precision. Machine tools application frequently calls for a high speed, rough cutting mode; followed by final low speed, high precision cutting. Spindle drives with automatic tool exchange call for extremely high top speeds at which the precision is not essential, but need as well high precision position measurement in the tool exchange mode. If the resolver with the R/D converter is used as the shaft sensor, the overall drive performances will be bonded by the necessity to choose and keep fixed one resolution of the R/D converter. When the top drive speed is high, so has to be the value of ω_{max}, and the user must select a low R/D resolution. Consequently, low speed performances will worsen; the speed loop bandwidth, suppression of the torque disturbances and the precision of the positioning will be inferior with respect to the case of a higher *N;* that would have been applied if the high speed requirement were not imposed.

The method and the means for a software based on-line resolution adaptation are analyzed and proposed in this paper, with the aim to achieve better utilization of the resolver and the R/D converter; and allow simultaneously high precision low speed operation as well as high operational speeds with decreased accuracy of the position measurement. The method with both hardware and software aspects of proposed on-line resolution switching has been thoroughly tested and build into the digital multiaxes servoamplifier [3], showing excellent results field test results.

3. ON-LINE RESOLUTION SWITCHING: HARDWARE ASPECTS

Drawbacks of the fixed resolution operation of R/D converter might be eliminated by selecting the resolution *N* lower at high shaft speeds, while switching to 14- or 16-bit resolution in low-speed high-precision mode of operation. The pins of the R/D (named SC1 and SC2 in the case of 2S82 part [1]) provided for hardware selection of R/D resolution might be software controlled, in which case their status, and hence, the R/D resolution might be changed on-line, during the drive operation.

On-line change of the R/D resolution basically means the change of the counter length; that is, a 10 => 12 resolution switching changes the counter format from [b15 ... b6] - 10 bit word, to 12 bit [b15...b4] word. Due to the fact that the shaft speed does not change significantly during the switching interval, and taking into account that the BVCO frequency is given f_{BVCO} [Hz] = 2^N □[rps], the 10 => 12 resolution change must be followed by an increase of f_{BVCO} by four. The same way, reciprocal 12 => 10 resolution switching must be followed by a drop in the BVCO frequency by four.

The output frequency of the BVCO is controlled by the voltage level at the oscillators input (VCO IN signal in Fig. 1). This signal, in turn, is the output of an analog PI regulator, having the tracking error at the input. The VCO IN signal cannot change instantly, due to an inherently limited slope and response time of the PI block. Hence, inability to augment and diminish the VCO IN four times at the instant of the resolution switching will make impossible sudden changes in BVCO frequency. Therefore, a large tracking error will occur at the instant of SC1:SC2 switching, followed by the transient response of the tracking loop. In an environment of a servo drive with the speed loop, transient phenomena caused by the resolution change will provoke large torque spikes, speed errors, and the position error that is not acceptable. Severity of the problem might be observed better if the magnitude of the R/D internal speed error is considered: at each resolution change, the internal speed error is initially 400% - 100% = 300%.

It might be concluded from the above discussion that a means of step-changing the BVCO frequency by 4 must be found in order to obtain error-free, smooth resolution switching process; avoiding in such a way the interference with the speed and position loops. Solution to the problem is proposed hereafter, and applied on a 2S82 [1] R/D converter. Hardware details are given in Fig. 2.

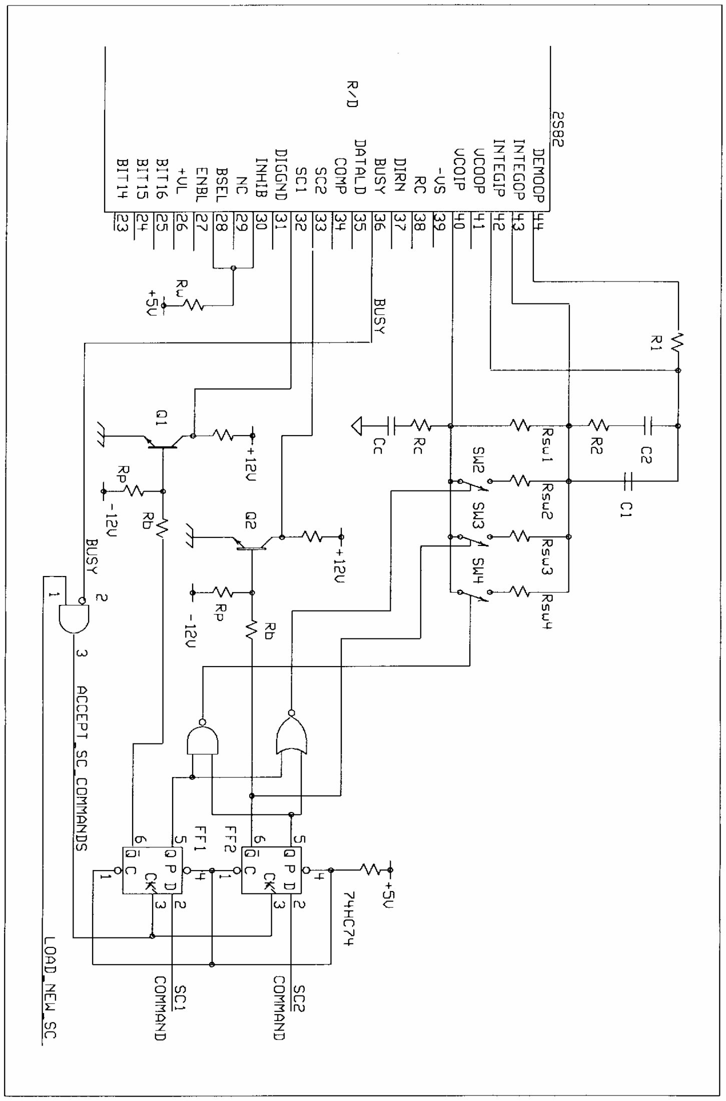

Fig. 2. On-line R/D resolution switching: Hardware modification.

The output of the PI block in Fig. 1 (the VCO IN signal) is labeled as the INTEGOP pin of 2S82 in Fig. 2. The BVCO within the 2S82 R/D converter is a current controlled device; that is, the frequency of the clock pulses varies with the current supplied into the VCOIP input pin. Under assumption that the INTEGOP output is at a constant value, the BVCO pulse frequency is determined by the resistance connected between the INTEGOP and the VCOIP pin. Step change in the BVCO frequency might be obtained by changing this resistance four times at the instants of the resolution change. For this purpose, resistors R_{sw1}, R_{sw2}, R_{sw3}, and R_{sw4} are introduced in Fig. 2, along with associated analog switches SW2, SW3, and SW4.

Analog switches SW2, SW3, and SW4 should be set ON and OFF in function of the current resolution of the R/D converter. To avoid transient response of the tracking loop and reduce the risk of a large tracking error, equivalent resistance should always change by the factor of 4. For 10-bit resolution, all the analog switches should be OFF, and the value of equivalent resistance between INTEGOP and VCOIP pins is $R_e = R_{sw1}$. Passing to 12-bit resolution, the switch SW2 must close at the same instant when the code signals SC1 and SC2 change to 12-bit status. Since R_e in this state must be exactly 1/4 of the previous R_{sw1}, the value of R_{sw2} might be found as $R_{sw2} = 1/3\ R_{sw1}$. In such a way, equivalent resistance for the 12-bit resolution will be 1/4 R_{sw1}. Increasing further the resolution and passing from 12-bit to 14-bit resolution, the switch SW2 remains closed, while SW3 closes in exactly at the instant of the commutation on SC1-SC2 pins. In order to get $R_e = 1/16\ R_{sw1}$, the value of R_{sw3} must be exactly 1/12 R_{sw1}. Going further to 16-bit, the analog switch SW4 must be turned on, and both SC1 and SC2 control signals must be driven to the logic 1 level at the same time. Since the equivalent resolution in such case must be 1/64 R_{sw1}, the value of R_{sw4} is calculated as 1/48 R_{sw1}.

The resolution change basically modifies the format of the UP/DOWN counter. Hence, the effect of one BVCO pulse expressed in terms of estimated position in [rad] changes from $2\pi/2^{10}$ for 10-bit resolution to $2\pi/2^{16}$ that we have for 16-bit resolution. Potentially, this might change the closed loop gain of the R/D tracking loop 64 times, and significantly affect the position measurement accuracy and dynamics. The tracking loop gain variation is avoided by inserting $R_{sw1}..R_{sw4}$ and commutating the analog switches in the prescribed way. Along with the resolution change imposed by SC1-SC2 signals, the value of equivalent resistance between the INTEGOP and VCOIP pins is changed four times; causing the same INTEGOP level to provoke four times higher/lower BVCO frequency. In such a way, considering the signal flow from the INTEGOP pin to the counter, whatever the resolution the same level at the INTEGOP pin will produce always the same rate of change of the estimated position expressed in [rad/s]. Example: one BVCO pulse affects the estimated position 4 times less at 12-bit resolution that the same pulse when the resolution is 10-bit; but the INTEGOP - VCOIP equivalent resistance is 4 times smaller at 12 bit resolution, and the same INTEGOP voltage level makes BVCO count 4 times faster. As the consequence, the bandwidth and dynamics of the tracking loop does not change with the R/D resolution, the loop performs always in the same way.

At hardware design stage, care must be taken to the internal timing of the R/D device. Namely, after each BVCO clocking pulse, the data contained in the counter change, and the transition state may last 300-400 ns. During this interval, the counter outputs invalid data that should not be used. For this reason and due to internal R/D timing problems, the resolution must not be changed during the transition interval. Rather than that, the command for the resolution switching should be issued during the time interval when the counter data is stable. Even at the top (1MHz) BVCO frequency, there are 600-700 ns left to perform the resolution change.

The R/D converter marks the transition intervals by establishing high level at the BUSY pin (Fig. 2). In order to ensure that the R/D resolution changes are performed at the beginning of a "data stable" interval, flip-flops FF1 and FF2 are used. At their D inputs, the digital microcontroller outputs the code for SC1 and SC2 lines. The new status of SC1 and SC2 will determine the R/D resolution, as soon as FF1 and FF2 latch the data. For that to happen, the digital microcontroller must confirm the request by setting high the LOAD_NEW_SC line. Now, next falling edge of BUSY signal will provoke a rising edge at the FF's clock input, and new values for SC1 and SC2 will appear at Q outputs. These outputs will consequently set the status of SC1 and SC2 pins of the R/D, and determine the state of SW2, SW3, and SW4 analog switches. In the prescribed way, the resolution change will begin when the transition period ends, and adverse effects of switching during the transition will be avoided.

With the hardware prerequisites outlined above, the R/D tracking loop will suffer no error due to on-line resolution change, providing that components used in Fig. 2 are ideal ones. Some parasitic effects though, might provoke a small tracking error to occur at the switching instant, and these are listed in section 5. The next section deals with the software aspects of the resolution switching, and explains when and how the SC1, SC2 and LOAD_NEW_SC commands should be issued.

4. SOFTWARE IMPLEMENTATION

The basic requirements with respect to the counter length N (that is, the resolution in terms of the number of bits) are to use the maximum possible resolution, while taking care not to exceed the BVCO maximum frequency. Basic rules might be inferred from the relation that connects the shaft speed and the BVCO frequency: $\square_{max}$[rps] = f_{max} [Hz] / 2^N . When the shaft speed is in a decline, the BVOC frequency will reduce as well. For values $f_{BVCO} < 0.25 f_{max}$, the resolution might be increased. Setting the next higher resolution in such a situation, the BVCO frequency will increase by a factor of 4. Since the previous value was $f_{BVCO} < 0.25 f_{max}$, the change will not pass over the BVCO top frequency, and the integrity of the position measuring system will be preserved.

During the acceleration phase of the drive, the shaft speed will increase along with the BVCO pulse frequency. When coming close to the top BVCO frequency, the R/D resolution must be decreased to the next lower value, in order to allow for further shaft speed rise. The resolution drop will divide the f_{BVCO} by 4, making continued acceleration possible.

Decision on when and how to change the R/D resolution is made by the digital controller. Thresholds might be determined in terms of the shaft speed, or alternatively judged from the BVCO frequency. If the shaft speed were to determine the switching, a set of 6 thresholds would be necessary. For 12- and 14- bits both the upper and the lower limit would be necessary, while the minimum 10-bit and the maximum 16-bit resolutions will need only one threshold: lower (10-bit) and upper (16-bit).

Deriving the switching instants from the frequency of the BVCO pulses is natural choice, and much simpler to implement. It is sufficient to count the BVCO pulses, measuring in such a way the frequency. Only two limits have to be established: the minimum frequency (below which the resolution will be increased) and the maximum frequency (above which the resolution should be decreased).

The action of the digital controller consist in keeping the LOAD_NEW_SC signal in a passive state until the moment when the resolution change is required. At the instant of change, the lines SC1_COMMAND and SC2_COMMAND must be set first. Following that action, the LOAD signal should go into its active state, and remain active until at least on BUSY period passes; making sure in such a way that the flip flips latch the data.

5. PARASITIC PHENOMENA AND REMEDIES

Previous discussion assumed a linear relation between the BVCO input current and its output frequency. This linearity is essential for the proper operation of the proposed method. Namely, since each resolution change calls for a BVCO frequency change by a factor of 4.

We designed the hardware in such a way that the change of the BVCO input current is ensured to be correct (that is, the BVCO input current will also change by a factor of 4). Now, if the BVCO input/output characteristics is linear, its output frequency will perform accordingly. Any error in the BVCO linearity will cause the pulse frequency to change at the instant of resolution switching by a factor higher or lower that 4. As a consequence, as explained above, the switching cause the tracking error and the transient response of the tracking loop. In order to avoid this problem, the switching thresholds (in terms of the BVCO pulse frequency) should be chosen in such a way that the corresponding points on the BVCO_IN / BVCO_OUT characteristics have the same ratio between the BVCO input current and the corresponding BVCO output frequency.

Special care should be taken in selecting the bipolar transistors Q1 and Q2 in Fig. 2, used for level-shifting the TTL signals up to the 12 V logic level; as well as their polarization resistors R_p, and R_b. Namely, the turn-on delay must be longer or equal to their turn-off delay; and that might be obtained by choosing the pull-up resistors, R_b and R_p. Having the turn-on delay longer, any transition on SC1 and SC2 pins of the R/D such as 10 => 01 will pass through the 11 state. Notice that the same transition will pass through the 00 state, providing that the turn-on is faster than turn-off. Due to the internal logic of the 2S82 R/D converter, it is essential to avoid passing through the 00 state. More specifically, 10 => 01 and 01 => 10 transitions correspond to the resolution change from 12 to 14 and vice versa. If transition passes shortly through the 00 state (that corresponds to the 10-bit resolution), the R/D converter will reset those counter bits that are not being used by the 10-bit resolution configuration. There are two bits that are being used by the 12- and 14-bit resolution, and not being used by 10-bit resolution. Hence, a short 00 interval will reset these bits and damage the data in the counter. In turn, the tracking loop will exhibit a transient response, attempting to correct the error. Having $\tau_{TURN\text{-}ON} < \tau_{TURN\_OFF}$ will completely eliminate the risk of generating the tracking error.

6. CONCLUSION

The paper proposes a software-based, simple to implement method of increasing the resolution of position feedback signal in an environment of the servo drive with electromagnetic resolver and the resolver-to-digital converter. The method requires minor hardware modifications that do not involve expensive parts and do not increase the hardware cost. Experimental verification shows and increase of the speed loop performance parameters by roughly 25%. The method is build into the series-produced DBM03 line of digital multiaxes servoamplifiers where it showed an excellent performance.

7. LITERATURE

[1] Analog Devices Inc., “Design-in reference manual: Data converters, amplifiers, special linear products, support components”, 1994.

[2] Hanselman, D.C.: “Resolver signal requirements for high accuracy resolver-to-digital conversion”, IEEE Transactions on Industrial Electronics, IE-37, 1990, pp 556-561

[3] Vickers Polymotor: “DBM03 installation guide and users manual”, 1994.

ON LINE ADAPTATION OF THE ROTOR TIME CONSTANT IN SENSORLESS AC DRIVES

Darko P. Marčetić

Abstract: *High performance servo applications of an induction motor can be made possible by implementing the vector control technology. The vector control allows decoupled control of the torque and flux components equivalent to that of a separately excited dc machine. This advance in control technology, coupled with consistent price reduction in power electronics, made the vector controlled induction motor highly competitive on the low cost motor systems market. Further advance in the induction motor drives technology is also feasible, and it is coupled with the elimination of the sensors needed for the drive to operate. Especially, the development of a shaft-sensorless induction drive is the best answer for the persistent demand from the market place for less expensive and yet more robust drives. However, in applications where the safety regulations apply, shaft-sensorless operation is acceptable only in cases where a robust, reliable speed estimation is available, not being prone to thermal drift or any other secondary effect that may endanger correct speed estimation. Therefore, to insure robust speed estimation, every known sensorless scheme should be upgraded with a machine parameter on-line identification mechanism. This paper discusses the new technique for on-line identification of the rotor time constant suitable for speed-sensorless control of induction motor. Proposed parameter correction action is very easy to implement in already existing MRAS based speed estimator. Its implementation has the minimum impact on a processor power and memory needs. This work demonstrates that proposed technique has potential to eliminate certain drawbacks of the previously published works.*

Keywords: *AC drives, Sensorless, Rotor Time Constant Adoptation*

1. INTRODUCTION

Different schemes for speed estimation are proposed [1]. The substantial part of the reported schemes relies on utilization of an induction machine model with the speed estimator either the open- or closed- loop type. Especially good results are reported for the speed estimators based upon the full order nonlinear observer [2], [3]. However, vast majority of speed-sensorless drives are used in low-cost drive applications where high-end processor associated with expensive peripherals and power supply should be avoided. On the other hand, the program and data memory limitations of a low-cost processor, together with the relatively low clock frequency, make most sensorless schemes that require intensive numerical calculations and memory usage inapplicable. In [4] Schauder investigates the rotor flux based MRAS for the speed estimation in drives with indirect field oriented control (IFOC). The method is rather simple to implement and uses minimum processor time and memory. Still, it employs open-loop flux estimator that requires the terminal voltage integration and it is also sensitive to stator circuit parameter errors, especially stator resistance (R_s) variations. Listed problems with the reference model can be reduced using the speed estimators proposed in [5]. Nevertheless, the sensitivity of the adjustable model used in MRAS to an error in the rotor circuit parameters must also be considered. In particular, if the rotor time constant parameter (T_r^*) is not equal to its actual value (T_r) an error in the estimated rotor speed will be introduced. The problem gets more significant in the low rotor speed region, where estimated slip value holds significant part of the rotor speed information. For these applications, it is essential that speed estimator has integrated an on-line T_r identification mechanism.

Variation of T_r is caused mainly by the change in rotor resistance due to temperature and also by the change in rotor inductance due to saturation. Following a fast rotor speed transient to the field weakening range, significant flux saturation level change can take place within 1 second. But, this variation in actual T_r value does not need to be tracked, rather it can be predicted and included in the feedforward flux model [6]. On the other hand, unpredictable thermal drift induced changes in the T_r value cannot be fast, yet slow-tracking T_r adaptation algorithm is still required.

In the case of the IFO controller with a shaft sensor, an error in T_r^* greatly affects an open-loop slip estimator and leads to undesirable cross coupling and deterioration of overall drive performance. This sensitivity is well recognized in the literature and different T_r identification mechanisms are reported [7]. Two major approaches were used, the schemes with and without injected test signals. Typical representative of the first group is given in [8]. Methods from the second group explore the use of different motor states within the MRAS parameter update model: stator voltages [9], reactive power [10] or special rotor flux based criterion function [11] designed to minimize the influence of R_s thermal drift and dead-time error on the T_r identification result. The difference between the measured and stator current estimated within the adaptive flux observer was also used in [12] for the simultaneous estimation of the rotor and stator resistances. The algorithm based on sensitivity analysis of the recursive leakage inductance estimation was reported in [13].

In the case of the shaft-sensorless drives, the T_r identification problem is almost completely overshadowed by the stator circuit parameter update and reference flux estimation problems. One of the reasons for it is that most of the sensorless schemes are more sensitive to the changes in the stator circuit parameters. Also, the steady state equations of the speed-sensorless drive do not offer enough information for the simultaneous estimation of the rotor speed and parameters, and finding the update mechanism for the unpredictable T_r^* variations cannot be a straightforward task [14].

The only way to estimate T_r and the speed together is to use the transient stage of drive operations. To initiate transient state, several authors use a test signal superimposed in the field current [15]. Akatsu and Kawamura in [14] show that test signals are not necessary and recommend the usage of rotor flux transients. Avoiding the unwanted test signal is the best path towards the optimal parameter estimation solution but also creates many new issues. First, significant rotor flux change can be caused by speed transient only, and the method cannot be used around a constant speed. Also, the converging time of the algorithm varies with amplitude of available signal. Finally, sensitivity of the T_r identification to an error in other machine parameters usually increases with the test signal cancellation.

The aim of this paper is to introduce a new possible source of information for the T_r identification, suitable for the use in speed-sensorless ac drive. First, we refer to the MRAS based speed estimator proposed in [4]. In section III, the small signal dynamics of a detuned sensorless drive is closely analyzed. The work is done in order to find the useful information about the error in T_r^*. It is assumed that the values of T_r^* used in the slip calculator and in the MRAS estimator are equal, but not accurate. As a result, new elements were added to the small signal propagation model. Further, the effect of the closed loop within the speed estimator is taken in consideration while deriving the final small signal dynamic equations. Section IV presents the novel algorithm based on the small signal model of a detuned MRAS based speed estimator. The algorithm achieves on-line correction of T_r^* based on the phase delay between some spectral components of the q stator current and the first derivative of MRAS speed estimator error. It is tested using computer simulations and the results are presented. Finally, specific small signal discovered for the motor delta connection only is investigated and used in a practical example of the T_r identification.

This paper will demonstrate that proposed T_r identification method can be utilized within the rotor flux based MRAS speed estimator. However, the scope of the proposed scheme is not limited to the unique MRAS speed estimator type. The same parameter update scheme would work using different rotor flux reference models. Also, with modest modifications this approach can be reused for the estimator proposed in [5].

2. MRAS SPEED ESTIMATOR

The speed estimation based on the MRAS makes use of two machine models with different structures that estimate the same motor state. In case of a sensorless induction drive, the primary used state variable is the rotor flux vector. The reference voltage and the adjustable current rotor flux models are given in (1) and (2). The error signal used to tune estimated speed value is phase angle between two vectors (3).

$$p\begin{bmatrix}\psi_{\alpha r}^{vi}\\ \psi_{\beta r}^{vi}\end{bmatrix}=\frac{L_r}{L_m}\left(\begin{bmatrix}v_{\alpha s}\\ v_{\beta s}\end{bmatrix}-\begin{bmatrix}R_s+\sigma L_s p & 0\\ 0 & R_s+\sigma L_s p\end{bmatrix}\begin{bmatrix}i_{\alpha s}\\ i_{\beta s}\end{bmatrix}\right) \quad (1)$$

$$p\begin{bmatrix}\psi_{\alpha r}^{\omega i}\\ \psi_{\beta r}^{\omega i}\end{bmatrix}=\begin{bmatrix}-\dfrac{1}{T_r} & -\omega_r\\ \omega_r & -\dfrac{1}{T_r}\end{bmatrix}\begin{bmatrix}\psi_{\alpha r}^{\omega i}\\ \psi_{\beta r}^{\omega i}\end{bmatrix}+\frac{L_m}{T_r}\begin{bmatrix}i_{\alpha s}\\ i_{\beta s}\end{bmatrix} \quad (2)$$

$$\varepsilon=\psi_{\alpha r}^{\omega i}\psi_{\beta r}^{vi}-\psi_{\beta r}^{\omega i}\psi_{\alpha r}^{vi} \quad (3)$$

where

$\vec{\psi}_r^{vi}=[\psi_{\alpha r}^{vi}\ \psi_{\beta r}^{vi}]^T$, $\vec{\psi}_r^{\omega i}=[\psi_{\alpha r}^{\omega i}\ \psi_{\beta r}^{\omega i}]^T$, $\vec{v}_s=[v_{\alpha s}\ v_{\beta s}]^T$, $\vec{i}_s=[i_{\alpha s}\ i_{\beta s}]^T$ are outputs of the rotor flux voltage model, current model, stator voltages and currents, respectively. ω_r is rotor angular frequency, L_m, L_s and L_r are magnetizing, stator and rotor inductance and $\sigma=1-L_m^2/L_sL_r$ is the total leakage factor. All in two-axis, stationary reference frame.

In order to match the phase angle between two estimated rotor flux vectors, the MRAS error signal is used via PI regulator (Fig. 1) to tune estimated speed variable and therefore to make correction of the model (2) result.

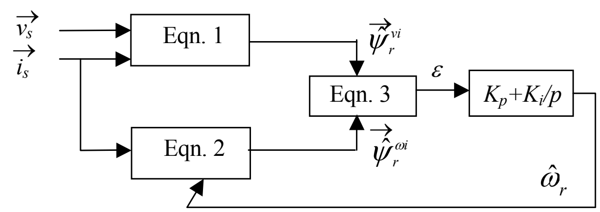

Fig. 1. Block diagram of MRAS based speed estimator

The reference voltage model is an open-loop flux estimator and therefore is sensitive to different machine parameter variations, the stator voltage estimation and integration errors. In order to insure robust work of this structure, the stator voltage estimation must include all the inverter nonlinearity effects, such as the switching devices dead-time and conducting voltage drop [18]. Furthermore, the stator resistance thermal drift must be compensated [15], [18], [19]. The R_s identification used in [14] compares amplitudes of two estimated rotor flux vectors and it is well suited for MRAS. The error in σL_s also affects the MRAS. For the squirrel cage motor σL_s changes insignificantly with the stator current value and it can be set off-line. For the motor with the closed rotor slots or double squirrel cage the on-line identification algorithm proposed in [21] could be used.

Feedforward correction of L_m and T_r^* parameters due to the main flux saturation level variation should also be included in the both flux models used in MRAS. An appropriate correction method is presented in [17] and it is summarized in the following. First, using the estimated stator voltages and measured currents, the magnetizing flux $\vec{\psi}_m^{vi}$ is estimated,

$$p\begin{bmatrix}\psi_{\alpha m}^{vi}\\ \psi_{\beta m}^{vi}\end{bmatrix}=\begin{bmatrix}v_{\alpha s}\\ v_{\beta s}\end{bmatrix}-\left(R_s+pL_{\sigma s}\right)\begin{bmatrix}i_{\alpha s}\\ i_{\beta s}\end{bmatrix},\ \psi_m=\sqrt{\psi_{\alpha m}^2+\psi_{\beta m}^2} \quad (4)$$

where $L_{\sigma s}$ is stator leakage inductance. Next, via the off-line defined function, value of the magnetizing flux is used for on-line update of the magnetizing inductance (L_m) parameter

$$L_m^*=f(\psi_m^2). \quad (5)$$

Finally, using (4) and (5), correct value of the reference rotor flux vector can be estimated,

$$\begin{bmatrix}\psi_{\alpha r}^{vi}\\ \psi_{\beta r}^{vi}\end{bmatrix}=\left(1+\frac{L_{\sigma r}}{L_m^*}\right)\begin{bmatrix}\psi_{\alpha m}^{vi}\\ \psi_{\beta m}^{vi}\end{bmatrix}-L_{\sigma r}\begin{bmatrix}i_{\alpha s}\\ i_{\beta s}\end{bmatrix} \quad (6)$$

where $L_{\sigma r}$ is rotor leakage inductance.

MRAS based speed estimation also depends upon the correct work of the adjustable rotor flux model (2). The model has two parameters (L_m^*, T_r^*) that should be altered with the change of the main flux saturation level. Magnetizing inductance parameter can be directly updated using (5).

The T_r^* value should be modified to follow the magnetizing inductance change, but care must be taken to include the thermal drift induced variation also. Latter change in T_r cannot be predicted, and the only way to compensate it is to use an on-line parameter identification mechanism. Taking into account both sources of the rotor parameter variation, the optimal structure for T_r^* update is shown in the Fig. 2.

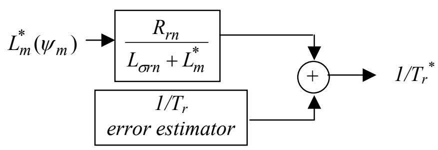

Fig. 2. On line identification of the rotor time constant

Within the proposed T_r parameter update structure, T_r identification algorithm needs to deal only with the unpredicted rotor parameter variations. That liberates it from the need to react to possible rapid flux saturation level changes and hence allows it to react slowly and more robustly to the R_r changes, originate in the thermal drift.

Based upon the collection of the previously published papers, the MRAS surrounding parameter update structure is almost completed and well known. However, the part of the aforementioned structure that is still lacking is a mechanism that can detect thermal induced T_r variations. One of the possible solutions is discussed in the following chapters.

3. DYNAMIC RESPONSE OF DETUNED MRAS SPEED ESTIMATOR

Since the steady state equations contain no information about the T_r^* error, the corrective system under the consideration is addressing small signal dynamics, as new possible source of information.

Let us consider an induction motor with the rotor time constant T_r. The utilized IFO controller and MRAS estimator use the same detuned value of the T_r^* parameter. In any practical application of this drive, different transient states are expected. The change of the rotor speed reference, or the change in the mechanical load will force a speed estimator to track the new rotor speed and thereby forcing a speed regulator to react. Even if that is not the case, speed estimator is always in quasi steady state due to the PWM inverter noise and/or limited number of current A/D converter bits. Furthermore, the interactions between the speed estimator and speed loop sampling can create additional torque jitter and may lead to the quantization-induced oscillations [20]. Dynamic analysis of the different small signal variations can be done by linearizing system equations around the chosen steady state point [4]. The system transfer function describes the dependence between the small MRAS error signal ($\Delta\varepsilon$) and the rotor speed:

$$\Delta\varepsilon = \frac{\left(\Psi_{dro}^2+\Psi_{qro}^2\right)\left(p+\frac{1}{T_r}\right)}{\left(p+\frac{1}{T_r}\right)^2+\omega_{so}^2}\left(\Delta\omega_r-\Delta\hat{\omega}_r\right) \qquad (7)$$

where $\hat{\omega}_r$ is estimated rotor angular frequency, Δ is small signal symbol, $\vec{\psi}_{ro}=[\psi_{dro}\ \psi_{qro}]^T$ is steady state rotor flux.

Equation (7) is derived with assumption that T_r is well known. This paper investigates the influence of T_r^* parameter error on the same small signal dynamic. First, steady state of the detuned drive ($T_r^* \neq T_r$) was examined using the variables in the rotor flux reference frame. Using the steady state equation of adjustable model $\hat{\omega}_{so}\hat{\psi}_{dro}-(1/T_r^*)\hat{\psi}_{qro}=(L_m/T_r^*)I_{qso}$, and the value of calculated slip $\hat{\omega}_{so}=L_m I_{qso}/(T_r^*\hat{\psi}_{dr0})$, one can conclude that the estimated q axis rotor flux will always be close to zero. If the reference model is correct, due to the MRAS feedback, actual q rotor flux will also be close to zero. However, based upon $\omega_{so}\psi_{dro}-(1/T_r)\psi_{qro}=(L_m/T_r)I_{qso}$, attained and estimated slip could be different $\omega_{so}T_r=\hat{\omega}_{so}T_r^*$.

Around any steady state point, MRAS flux models respond to small signal changes at their inputs. Presuming no errors, the dynamic of the voltage reference model can be modeled with the adjustable current model using the true rotor speed as input and correct T_r as parameter ($\vec{\psi}_r^{vi}=\vec{\psi}_r$). The linearized version of described model is given in (8),

$$p\begin{bmatrix}\Delta\psi_{dr}\\ \Delta\psi_{qr}\end{bmatrix}=\begin{bmatrix}-\frac{1}{T_r} & \omega_{s0}\\ -\omega_{s0} & -\frac{1}{T_r}\end{bmatrix}\begin{bmatrix}\Delta\psi_{dr}\\ \Delta\psi_{qr}\end{bmatrix}+\frac{L_m}{T_r}\begin{bmatrix}\Delta i_{ds}\\ \Delta i_{qs}\end{bmatrix}+\begin{bmatrix}\Psi_{qro}\\ -\Psi_{dro}\end{bmatrix}\Delta\omega_s \qquad (8)$$

The linearized equations of the detuned MRAS adjustable model ($\vec{\psi}_r^{\omega i}=\vec{\hat{\psi}}_r$) are given in (9),

$$p\begin{bmatrix}\Delta\hat{\psi}_{dr}\\ \Delta\hat{\psi}_{qr}\end{bmatrix}=\begin{bmatrix}-\frac{1}{T_r^*} & \hat{\omega}_{s0}\\ -\hat{\omega}_{s0} & -\frac{1}{T_r^*}\end{bmatrix}\begin{bmatrix}\Delta\hat{\psi}_{dr}\\ \Delta\hat{\psi}_{qr}\end{bmatrix}+\frac{L_m}{T_r^*}\begin{bmatrix}\Delta i_{ds}\\ \Delta i_{qs}\end{bmatrix}+\begin{bmatrix}\hat{\Psi}_{qr0}\\ -\hat{\Psi}_{dr0}\end{bmatrix}\Delta\hat{\omega}_s \qquad (9)$$

where ω_{so} and $\hat{\omega}_{so}$ are the steady state values of actual and estimated slip frequency, $\vec{\psi}_{ro}=[\hat{\psi}_{dro}\ \hat{\psi}_{qro}]^T$ is the steady state value of the estimated rotor flux , $\vec{i}_s=[i_{ds}\ i_{qs}]^T$ is stator current. All variables are in two-axis, rotating reference frame.

Two models have the different T_r and different steady state slip frequency value, and in the event of the small signal changes ($\Delta\omega_r$ or Δi_{qs}) these models should react differently. The adjustable model within the controller as the input has the estimated slip frequency variations,

$$\Delta\hat{\omega}_s=\frac{L_m}{T_r^*\hat{\Psi}_{dr0}}\Delta i_{qs} \qquad (10)$$

while the actual rotor flux follows the actual slip frequency variations ($\Delta\omega_s$). Difference between two frequencies is

$$\Delta\omega_s = \Delta\hat{\omega}_s + \left(\Delta\hat{\omega}_r - \Delta\omega_r\right). \tag{11}$$

Provided that the same T_r^* parameter value is used in the IFOC slip estimator and in the MRAS adjustable flux model, latter becomes insensitive to the changes in the q axis stator current. As a consequence, if there is no change in d axis current (Δi_{ds}=0), the change in the q stator current alone does not trigger any change in estimated flux components. Quite the opposite of above, if $T_r^* \neq T_r$, the actual flux does vary and that should be seen in reference model.

Neglecting second order small signals, $\Delta\psi_{dr}\Delta\varepsilon_{qr} \approx 0$ and $\Delta\psi_{qr}\Delta\varepsilon_{dr} \approx 0$, where $\Delta\varepsilon_{dr}$ and $\Delta\varepsilon_{qr}$ are small rotor flux deviations, the linearized MRAS error function becomes

$$\Delta\varepsilon = \psi_{dro}\Delta\varepsilon_{qr} - \psi_{qro}\Delta\varepsilon_{dr} \approx \psi_{dro}\Delta\psi_{qr}. \tag{12}$$

Based on (8) and discussion above, the resulting linearized MRAS error function is given in (13):

$$\Delta\varepsilon = \frac{\Psi_{dro}^2\left(p + \frac{1}{T_r}\right)}{\left(p + \frac{1}{T_r}\right)^2 + \omega_{s0}^2}\left(\left(\Delta\omega_r - \Delta\hat{\omega}_r\right) + \frac{L_m}{\Psi_{dro}}\left(\frac{1}{T_r} - \frac{1}{T_r^*}\right)\Delta i_{qs}\right) \tag{13}$$

The detuned rotor parameter T_r^* obviously introduces an additional feedforward path in the MRAS error model. That path represents the direct influence of the small signal variations in q stator current component (Δi_{qs}) on the actual rotor flux q axis component. The resulting dynamic model of detuned MRAS estimator is given on Fig. 3.

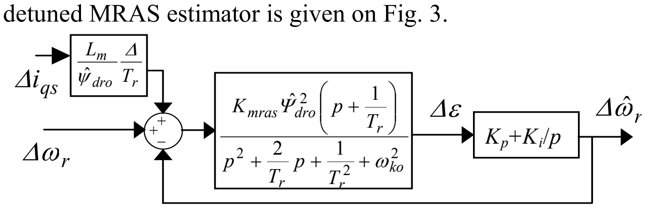

Fig. 3. MRAS estimator dynamics with detuned T_r parameter

The feedforward path for the small signals from input is canceled for T_r^*=T_r. But, if the parameter error does exist, additional small signal propagation will take place via extra-introduced block.

The feedback, estimated rotor speed ($\hat{\omega}_r$) is a function of MRAS error variable. In order to track actual rotor speed, the estimator continuously regulates that variable through typical PI regulator action. Analyzing the entire system dynamics, this closed loop action was taken into consideration,

$$\Delta\varepsilon = K(p)\left[\Delta\omega_r + \frac{L_m}{\Psi_{dro}}\left(\frac{1}{T_r} - \frac{1}{T_r^*}\right)\Delta i_{qs}\right],$$

$$K(p) = \frac{K'_{mras}\, p\left(p + \frac{1}{T_r}\right)}{p\left(\left(p + \frac{1}{T_r}\right)^2 + \omega_{so}^2\right) + K'_{mras}\left(pK_p + K_i\right)\left(p + \frac{1}{T_r}\right)} \tag{14}$$

where $K'_{mras} = K'_{mras}\Psi_{dro}^2$.

The filter action of $K(p)$ depends on the MRAS gains. In [16], MRAS PI regulator gains are set for the specified dumping factor (ξ) and natural angular frequency (ω_c):

$$K_i = \omega_c^2 / K'_{mras}, \quad K_p = (-1/T_r + 2\xi\omega_c)/K'_{mras}. \tag{15}$$

Resulting MRAS closed loop equations (16) is valid for zero slip condition only, but similar filter action of $K(p)$ is present for any value of the steady-state slip frequency

$$\Delta\varepsilon = \frac{K'_{mras}\, p}{p^2 + 2\xi\omega_c + \omega_c^2}\left[\Delta\omega_r + \frac{L_m}{\Psi_{dro}}\left(\frac{1}{T_r} - \frac{1}{T_r^*}\right)\Delta i_{qs}\right]. \tag{16}$$

The MRAS error closed loop transfer function has two independent small signal inputs, the true rotor speed and the q stator current. The first part of the function describes the MRAS dynamics while tracking an actual rotor speed. The second part is the function of the rotor circuit parameter error and may be used as the source for the parameter correction.

4. PROPOSED ESTIMATION TECHNIQUE

As it is shown in the previous section, the small signal of speed estimator error is the function of the variations in the actual rotor speed ($\Delta\omega_r$) and small signal variations in the q stator current (Δi_{qs}). Due to the limited frequency range of machine's mechanical subsystem, it is expected that $\Delta\omega_r$ contains none of the significant high frequency components. On the other hand Δi_{qs} does, and it has major influence on high frequency components of the MRAS error signal.

The proposed T_r error identification mechanism uses the relationship between the first derivative of the MRAS estimator error ($p\cdot\Delta\varepsilon$) and Δi_{qs},

$$p\Delta\varepsilon\big| = \frac{K'_{mras}\, p^2}{p^2 + 2\xi\omega_c + \omega_c^2}\left[\Delta\omega_r + \frac{L_m}{\Psi_{dro}}\left(\frac{1}{T_r} - \frac{1}{T_r^*}\right)\Delta i_{qs}\right]. \tag{17}$$

For the high signal frequency range, transfer function (17) has almost constant gain and introduces insignificant signal phase shift. If we also take into consideration that the mechanical rotor speed variations can be neglected for relatively high frequencies, the correlation between the signals Δi_{qs} and $p\cdot\Delta\varepsilon$ can be used to estimate the sign of T_r parameter error.

$$p\Delta\varepsilon\big|_{f\to\infty} \approx K_{mras}\Psi_{dro}L_m\left(\frac{1}{T_r} - \frac{1}{T_r^*}\right)\Delta i_{qs} \tag{18}$$

Equation (18) presents the direct link between the sign of the first derivation of the MRAS estimator error signal and the error in the rotor time constant parameter. This connection is valid only for the signal frequencies that are not influenced by the change in the mechanical rotor speed and also are out of the MRAS closed loop dynamic range.

Figs. 4-5 illustrate the rotor parameter identification scheme that is derived from previously presented equations. The T_r estimation block is integrated in typical IFOC structure with MRAS based speed estimator as it is shown on Fig. 4. Rotor parameter is on-line calculated using the model on Fig. 2. The updated value of $1/T_r^*$ parameter is used in MRAS adjustable model as well in the IFOC slip calculator. The proposed $1/T_r$ error estimation block (Fig. 5) uses simple multiplication for the phase delay sign extraction. Phase delay sign between the $i_{qs}(t)$ and $p\varepsilon(t)$ signals is then used as the $1/T_r$ error update signal. Integral action forces the parameter error to go to zero. Shown high pass filters are necessary to cancel low frequencies that are in MRAS estimator close loop dynamics range, and do not depend on T_r^* error only.

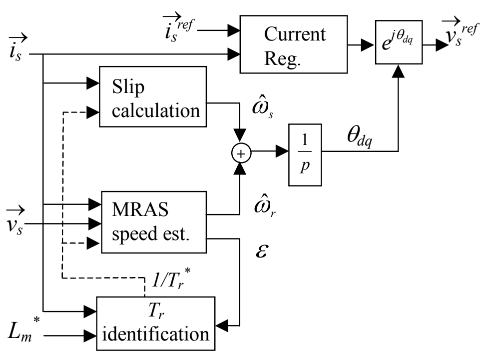

Fig. 4. IFOC with MRAS speed estimator and T_r on-line identification block.

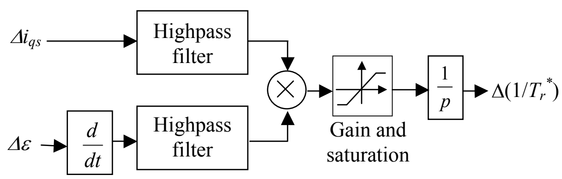

Fig. 5. Simplified block diagram of proposed $1/T_r$ error estimator.

The presented technique was initially verified using the computer simulations. The simulations of the speed controlled IFOC system with MRAS speed estimator and proposed T_r estimator are performed in Matlab, Simulink Toolbox. First, for the new model verification purpose only, the white noise test signal was added in q stator current signal. Second, PWM block was modeled and simulations are repeated with the PWM noise only. It was shown that both signals produce enough small signals needed for the T_r estimator block to operate. Simulation results are shown in the Figs. 6 and 7. The T_r^* parameter was initially set to an incorrect value in the both, IFOC and MRAS models. Five seconds after the start of the simulation, T_r^* update block was enabled. Simulation results are presented for the rotor speed signal at the motor model output ω_r, the estimated rotor speed $\hat{\omega}_r$, updated parameter $1/T_r^*$, phase error signal – *err* and filtered error signal – err_f.

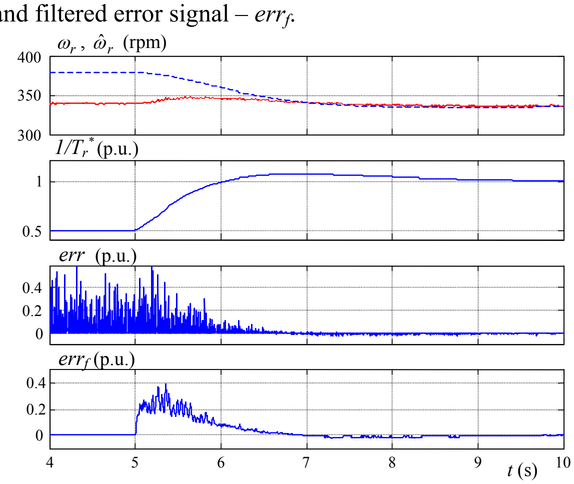

Fig. 6. T_r identification - simulation results for $1/T_r^* = 0.5\ 1/T_r$.

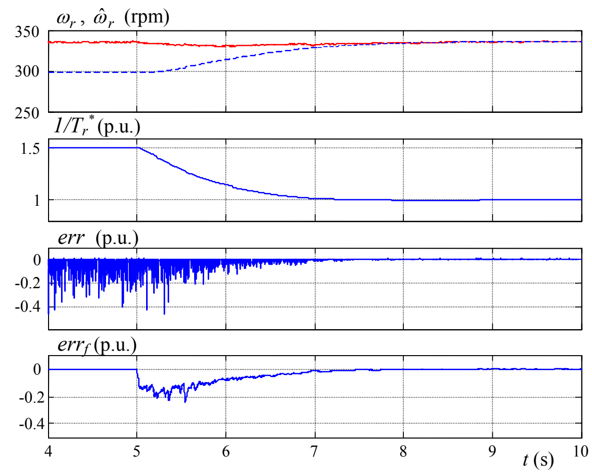

Fig. 7. T_r identification - simulation results for $1/T_r^* = 1.5\ 1/T_r$.

5. EXPERIMENTAL RESULTS

The experimental setup is presented on Fig. 8. The induction motor (parameters given in appendix) was loaded with MAGTROL 5410 dynamometer. Three-phase voltage source inverter was controlled digitally, using the low cost DSP ADMC341. The current measurement is performed via three shunts placed in inverter legs. The current signals are processed using DSP internal analog front-end with current sensing bipolar amplifiers and ADC based on the single slope technique. The rotor speed was monitored via an incremental encoder. The motor voltage was estimated using dc bus samples and the PWM pulses. The dead-time and conducting voltage drop of the switching devices are compensated in the software. The PWM frequency was set to 10 KHz, which is the same frequency used to sample inverter leg currents and dc bus voltage as well as speed estimator sampling rate. The estimator equations are made discrete using simple backward Euler formula. First order filters were used instead of pure integrators to suppress oscillations in the estimated flux values and in the MRAS error signal. In order to keep the same small signal dynamic input signals of the adjustable model and T_r estimation block were likewise corrected, $i_{\alpha\beta}' = p/(p+\omega_l) * i_{\alpha\beta}$, $i_{dq}' = i_{\alpha\beta}' * e^{-j\theta dq}$. In addition, some low-pass filters were included on the T_r estimator front-end in order to cut off the non-modeled signal dynamics at very high frequencies. The MRAS closed loop bandwidth was set to 100 *rad/s*, relative low frequency range comparing with the current loop actions.

With the feedforward parameter correction present (section II), the proposed T_r error estimator does not need to follow potentially fast flux transients. Consequently, the feedback might be enabled only when a stable flux level is reached, with the parameter corrective gains set to relatively low values. Even more important, the gains should be set according to the application specific signal that is going to be use in the identification process. In this practical example, corrective gains were set experimentally based upon the output of simple phase sensing algorithm prompted with a specific small signal discovered for the motor in delta connection only.

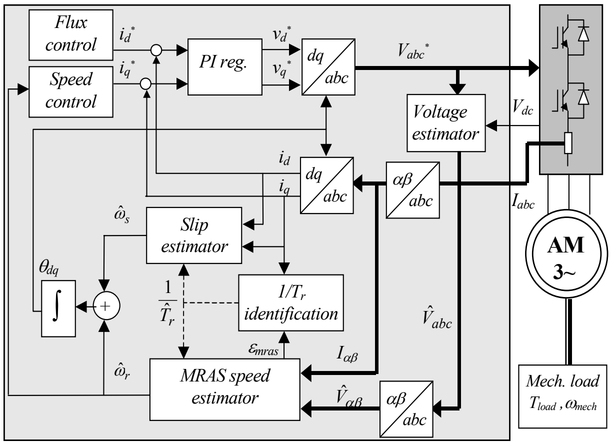

Fig. 8. Experimental setup, the shaft-sensorless IFOC with T_r update block.

The rotor speed and flux commands were set to constant values, and small signals in the q stator current were observed. Oscilloscope trace of motor line current that is the source of these signals is shown on the Fig. 9 for motor with and without mechanical load, both at 1000 rpm rotor speed. For both cases, instantaneous and filtered signal traces are shown.

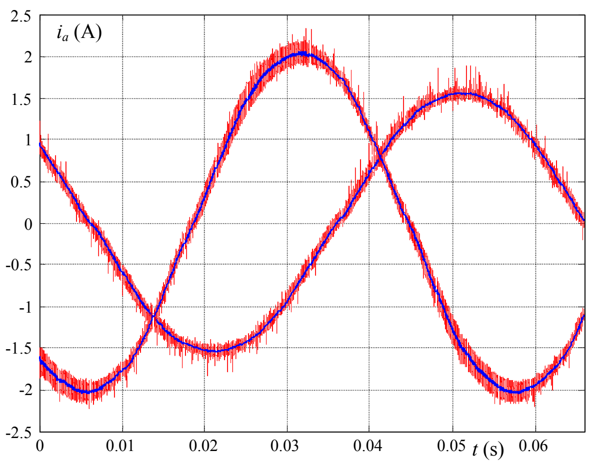

Fig. 9. Oscilloscope trace of line currents for no-load and load condition.

After the rotating transformation removes the fundamental component from the line current signals, the majority of the q and d stator current signals energy is contained within the dc and PWM frequency component. However, in the case of motor windings in delta connection (shown), relatively small sixth harmonic can also be noticed in line current. That signal creates corresponding oscillation in dq reference frame. Resulting signals measured for the d and q stator currents are shown on the upper traces of Fig 10. and Fig 11. for no-load and load condition. All presented signals were stored on-line with 1KHz sampling rate and then transferred via serial link. Although there is some PWM signal aliasing with each signal, appearance of sixth harmonic in q stator current is very clear. It is believed that presumed windings symmetry during the motor phase current reconstruction together with imperfect current measurement block is the root cause of parasite sixth harmonic in the q stator current signal.

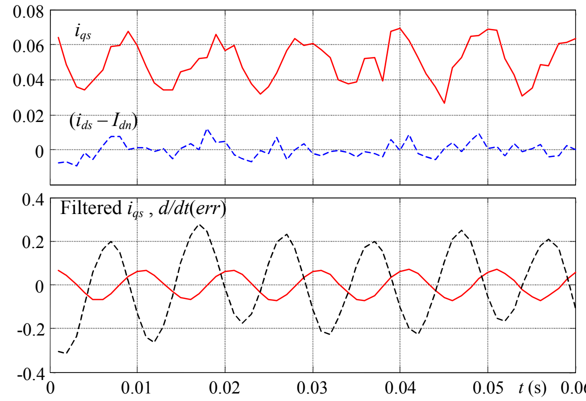

Fig. 10. Small signals utilized for T_r^* on-line correction. Stator current i_{ds} and i_{qs}, no-load. Amplified and band pass filtered *d/dt (err)* and i_{qs} signals.

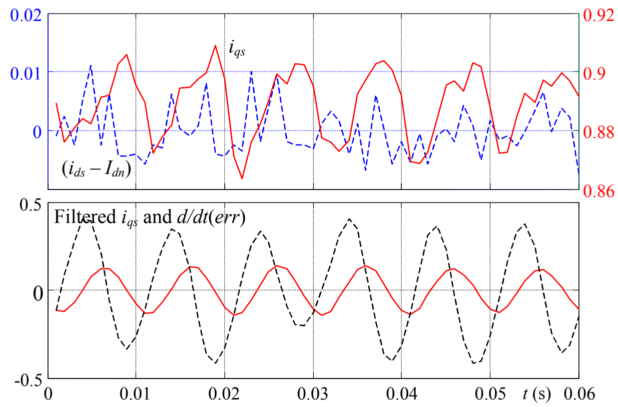

Fig. 11. Small signals utilized for T_r^* on-line correction. Stator current i_{ds} and i_{qs}, 50 % load. Amplified and band pass filtered *d/dt (err)* and i_{qs} signals.

Discovered small signal is relatively small amplitude (2-3% of nominal current value) and there was no observable oscillation in the rotor speed. Similar small signals are acceptable for most of the drive application, provided that their existence does not affect specified output speed and torque range.

To investigate this signal further, it can be separated and amplified using a band pass filter with the central frequency six times higher than fundamental. Lower traces of Fig. 10. and Fig. 11. show the resulting band-pass filtered q current and first derivation of MRAS error signal (dashed). Most of the small signals within the q stator current have corresponding oscillation in the MRAS error signal. In the MRAS error signal only, first and second harmonic of the stator frequency were also present, especially if flux integrators were not set correctly and the inverter nonlinearities were not compensated in full. These signals can create oscillations in the T_r estimator result and should be minimized and then canceled after the band-pass filter.

The first experimental result demonstrates that proposed T_r identification technique can extract the parameter error information from the small signal described above. All the data on Fig. 12. was transferred on-line via serial link from the DSP to the PC. Bandwidth of the serial link allowed 1 KHz sampling rate for the 8 monitored variables. Fig. 12 shows the T_r identification results for the drive in the speed-controlled mode (10Hz) and dynamometer set for the 50% of the motor nominal load torque.

The reference value for the d axis stator current was set to provide the nominal rotor flux. The central frequency of utilized band-pass filters was set to 60 Hz, in order to separate specific small signal around the chosen rotor speed (600 rpm). The parameter identification was enabled. Ten seconds after the data acquisition start, T_r^* was set to incorrect value, $1/T_r^*$=[0.5,0.75,1.25,1.5]·$(1/T_r)$. Figure displays the measured and estimated rotor speed (dashed line), normalized $1/T_r^*$ trace and filtered phase error signal.

The Fig. 12 demonstrates that small signal present in the system carry enough information for rotor parameter update. The estimator response is relatively slow, but seems adequate presuming that only the temperature-induced changes in the rotor time constant are to be tracked.

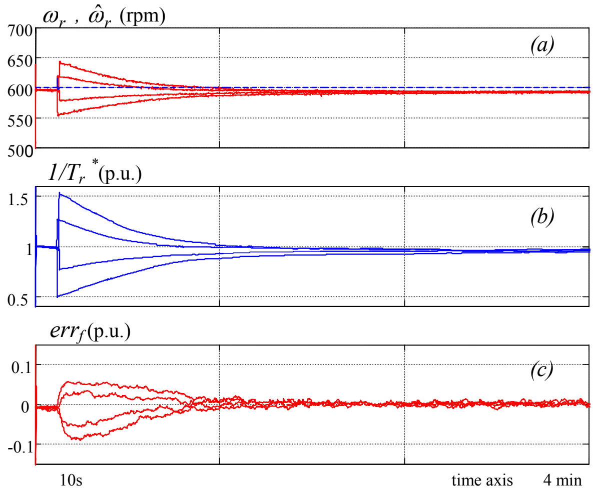

Fig. 12. Speed control mode, 50% rated torque: a) measured and estimated (dashed line) speed, b) $1/T_r^*$ parameter update and c) filtered phase error.

In order to explore the algorithm sensitivity to the steady state point change, another set of experiments was performed. Algorithm for the T_r^* update was disabled and rotor parameter was set first to 50%, then to 150% of its nominal value. Parameter update error signal was observed for variety of speed transients and steady speed commands. Taking into account variable frequency of the discovered small signal, during the following experiments a band-pass filter with variable central frequency was used. Consequently, similar amount of information about the T_r^* error was available throughout the whole speed range. Results for the motor without the mechanical load (free shaft) are shown on the Fig. 13. The estimated (dashed) and measured speed are displayed on the upper trace, while the lower trace shows the T_r estimation error signal. The same signals are shown on Fig. 14. for the motor loaded with the 75% of the rated torque.

Experimental results demonstrate that the right information for the parameter update holds for the most of the examined operational points. Ones enabled, driven by the displayed error signal algorithm would correct the T_r^* parameter and achieved rotor speed would match its reference value. However, the error in the reference flux estimation increases as the shaft approaches the speeds close to zero, especially when load applied. Although the MRAS speed estimator was able to work stable for all requested speeds, it can be noticed that the very low shaft speeds together with the high load applied can lead to the sign change in the T_r error signal. That would create the unstable feedback and the rotor parameter estimation would fail. This is believed to be the direct result of increased reference flux error due to the voltage inverter nonlinearity.

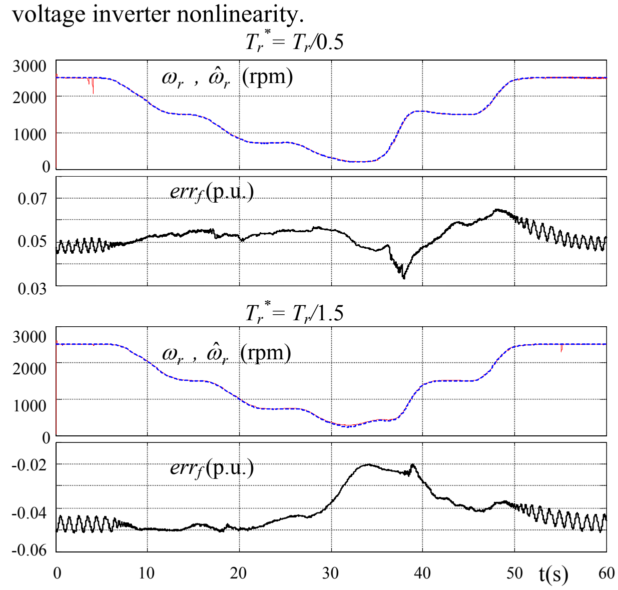

Fig. 13. Different speed transients and operating points, free shaft, 1) measured and estimated (dashed line) rotor speed, 2) filtered phase error.

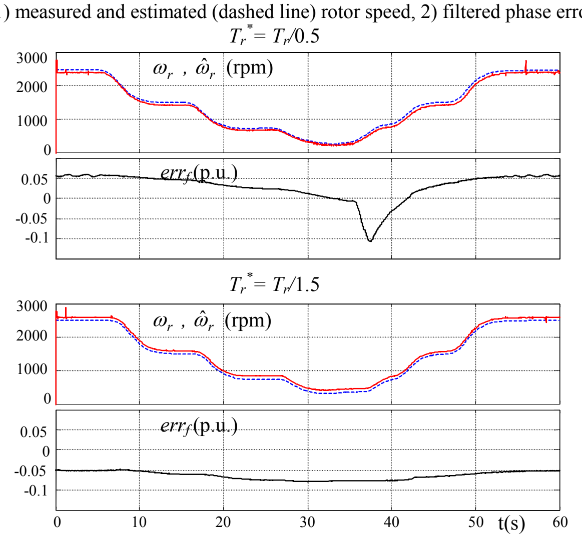

Fig. 14. Different speed transients and operating points, 75% nominal load, 1) measured and estimated (dashed line) rotor speed, 2) filtered phase error.

As it is shown, for the accurate work of the proposed T_r identification algorithm it is required that the MRAS reference model works correctly. That becomes impossible for the rotor speeds very close to zero and the low speed limit for the proposed algorithm employment must be set. For any other speed range, additional care must be taken while setting the parameters of the MRAS reference model. Previously demonstrated experiments were performed for the speeds within the nominal range and magnetizing inductance was kept constant. The same is valid for the σL_s parameter that was estimated while the drive at rest and also kept constant. In order to keep the rotor and stator resistances close to nominal values the motor temperature was monitored and controlled via external ventilation. In addition, in the regular time intervals the R_s^* parameter was updated using the algorithm used in [14].

In the next set of experiments parameter sensitivity of the proposed T_r update algorithm is explored. Under the scope were possible errors in the voltage rotor flux model parameters R_s^* and σL_s^*. Each parameter was individually set to the incorrect value and algorithm operation was observed. Fig. 15a shows sensitivity to the R_s variation. Ten seconds after the data acquisition start, parameter R_s^* was artificially set to the incorrect value, R_s^*=[0.5, 0.75, 1.25, 1.5]$\cdot R_s$. Fig. 15b shows the influence of the σL_s^* error, σL_s^*=[0.8, 0.9, 1.1, 1.2]$\cdot \sigma L_{sn}$.

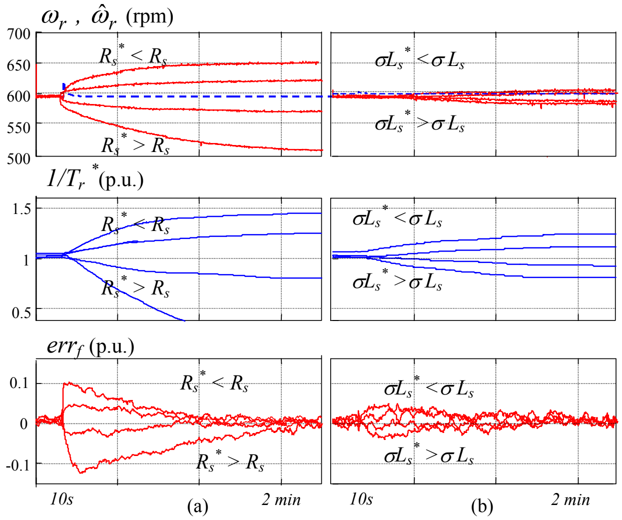

Fig. 15. Speed control mode with T_r update and the error in R_s^* and σL_s^*: 1) measured and estimated (dashed line) rotor speed, 2) $1/T_r^*$ parameter update trace and 3) filtered phase error.

As it was expected from (1), proposed algorithm is sensitive to the error in the MRAS reference model parameters. While sensitivity to the R_s error does not change with load, sensitivity to the σL_s error does, making method almost insensitive for light loads. It can be also noted that estimation result changes with the voltage estimation error and also with the error in the current measurement offset. On the other hand, small error in the current measurement calibration constants does not affect the results. All of the mentioned system imperfections affect the estimated rotor flux value and introduce unwanted output offset that leads to an error in the estimated rotor time constant.

6. CONCLUSION

This paper discusses the new technique for on-line identification of the rotor time constant suitable for speed-sensorless control of induction motor. Proposed parameter correction action is very easy to implement in already existing MRAS based speed estimator. Its implementation has the minimum impact on a processor power and memory needs. This work demonstrates that proposed technique has potential to eliminate certain drawbacks of the previously published works. It can use various small signals in stator current as an inherent test signal for the rotor parameter update. Although existing small signals vary and are application specific, these can be found in most known practical sensorless drive applications. Especially favorable target application for this algorithm can be the washing machine, where the inherent high load torque ripple always insures enough information for the T_r update. Also, the advantage of this technique is that is based upon the relative correlation between two selected small signals, which can be independent of the steady-state rotor speed and torque. However, there are still many open issues. Technique does require correct value of the stator resistance and stator leakage inductance parameters. Its result of rotor time constant update is also sensitive to the error in stator voltage estimates. Listed problems increase low speed limit for possible use of this technique. However, better rotor flux estimation solutions are already available and this technique with some modest modifications may be a possible path towards robust solution for the speed-sensorless rotor time constant parameter update.

APPENDIX

TABLE I – MOTOR PARAMETERS

800 W, 195 V, two pole, 4200 rpm/min, Δ connection
R_s = 9.1 Ω , R_r = 5.73 Ω , L_m = 0.585 H *, L_s = 0.615 H* , L_r = 0.615 H*, σL_s = 0.058 H* *Under rated conditions.

REFERENCES

[1] Joachim Holtz, "Methods for speed sensorless control of AC drives", *Sensorless Control of AC motors, IEEE Press Book*, 1996.

[2] Hisao Kubota, Kouki Matsuse and T. Nakano, "DSP-Based Speed Adaptive Flux Observer of Induction Motor", *IEEE Trans. Ind. Applicat.*, vol. 29, No 2, pp 344-348, March/April, 1993.

[3] Surapong Suwankawin and Somboon Sangwongwanich, "A Speed-Sensorless IM Drive With Decoupling Control and Stability Analysis of Speed Estimation ", *IEEE Trans. Ind. Applicat.*, vol. 49, No 2, pp 444-455, April, 2002.

[4] Colin Schauder, "Adaptive speed identification for vector control of induction motors without rotational transducers", *IEEE Trans. Ind. Applicat.*, vol. 28, No 5, pp 1054-1061, Sept/Oct, 1992.

[5] Fang-Zheng Peng, Tadashi Fukao and J. S. Lai, "Low speed performance of robust speed identification using instantaneous reactive power for tacholess vector control of induction motors", *IEEE Industry Applications Society*, pp 509-514, 1994.

[6] E. Levi, S. N. Vukosavić and V. Vučković, " Study of main flux saturation effects in field oriented induction motor drives ", in *Conf. Rec. IEEE Ind. Electron. Soc. Ann. Meet. , IECON* '89, pp 219-224.

[7] R. Krishnan, A. S. Bharadwaj, "A Review of Parameter Sensitivity and Adaptation in Indirect Vector Controlled Induction Motor Drive Systems", *IEEE Trans. Power Electron*, vol. 6, pp. 695–703, Oct. 1991.

[8] R. Schmidt, "On - line identification of the secondary resistance of an induction motor in the low-frequency range using a test vector", *Proc. ICEM '88*, Pisa, pp. 221-225, 1988.

[9] T. Rowan, R. Kerkman and D. Laggate, "A simple on-line adaptation for indirect field orientation of an induction machine ", *IEEE Trans. Ind. Applicat.*, vol. 37, pp 720-727, July/Aug. 1991.

[10] L. Garces, "Parameter Adaptation for the Speed-Controlled Static AC Drive with a Squirrel-Cage Induction Motor Operated with Variable Frequency Power Supply", *IEEE Trans. Ind. Applicat.*, vol. IA-16, pp 173-178, Mar./Apr.1980.

[11] S. N. Vukosavic and M. R. Stojic, "On-line tuning of the rotor time constant for vector-controlled induction motor in position control applications," *IEEE Trans. Ind. Electron.*, vol. 40, pp. 130–138, Feb. 1993.

[12] S. Ho Jeon, K. Kyo Oh, and Jin Young Choi, "Flux Observer With Online Tuning of Stator and Rotor Resistances for Induction Motors", *IEEE Trans. Ind. Electron.*, vol. 49, No 3, pp 653-664, June 2002.

[13] D. Telford, M. W. Dunnigan and B. W. Williams, "Online Identification of Induction Machine Electrical Parameters for Vector Control Loop Tuning", *IEEE Trans. Ind. Electron.*, vol. 50, No 2, pp 253-261, April 2003. K. Akatsu and A. Kawamura, "Online rotor resistance estimation using the transient state under speed sensorless control of induction motor", *IEEE Trans. Power Electron*, vol. 15, No 3, pp 553-560. May, 2000.

[14] K. Akatsu and A. Kawamura, "Online rotor resistance estimation using the transient state under speed sensorless control of induction motor", *IEEE Trans. Power Electron*, vol. 15, No 3, pp 553-560. May, 2000.

[15] H. Kubota and K. Matsuse, “Speed sensorless field-oriented control of induction motor with rotor resistance adaptation“, *IEEE Trans. Ind. Applicat.*, vol. 30, No 5, pp 1219-1224, September/October, 1994.
[16] Hirokazu Tajima and Yoichi Hori, “Speed sensorless field-orientation control of the induction machine“, *IEEE Trans. Ind. Applicat.*, vol. 29, No 1, pp 175-180, Jan/Feb, 1993.
[17] E. Levi and M. Wang, “A Speed Estimator for High Performance Sensorless Control of Induction Motors in the Field Weakening Region“, *IEEE Trans. Power Electron.,* vol. 17, No 3, pp 365-377, May, 2002.
[18] Joachim Holtz and Juntao Quan, “Drift- and Parameter-Compensated Flux Estimator for Persistent Zero-Stator-Frequency Operation of Sensorless-Controlled Induction Motors“, *IEEE Trans. Ind. Applicat. ,* vol. 39, No 4, pp 1052-1060, July/August, 2003.
[19] Maurizio Cirrincione, Marcello Pucci, Giansalvo Cirrincione, and Gérard-André Capolino, “A New TLS-Based MRAS Speed Estimation With Adaptive Integration for High-Performance Induction Machine Drives“, *IEEE Trans. Ind. Applicat.*, vol. 40, No 4, pp 1116-1137, July/August, 2004.
[20] Li Ran and Yong Liao, “ Sampling-Induced Resonance in an Encoderless Vector-Controlled Induction Motor Drive“, *IEEE Trans. Ind. Electron.*, vol. 51, No 3, pp 551-557, June 2004.
[21] Toshihiko Noguchi, Seiji Kondo, and Isao Takahashi “Field-Oriented Control of an Induction Motor with Robust On-Line Tuning of Its Parameters“, *IEEE Trans. Ind. Applicat.,* vol. 33, No 1, pp 35-42, January/February, 1997.

DESIGN OF MICROPROCESSOR-BASED SPEED SERVOMECHANISM WITH AC MOTOR AND ELECTROMAGNETIC RESOLVER

Zlatan A. Hadzimurtezic

Abstract. *This paper describes a novel procedure for optimal tuning of the speed controller parameters in the presence of a position sensor and an actuator performance limits. The proposed speed servo system is AC motor based and uses a resolver-type sensor for position measurement. The effectiveness of this analytical tuning procedure is confirmed by computer simulations.*
Keywords: *AC Motor Drive, Speed Servomechanism, Resolver.*

1. INTRODUCTION

In recent years, AC-motor based speed servo systems have been widely used in numerous automated factory systems. Such environments usually involve elevated temperatures which makes the use of conventional optical transducers very difficult. A significant progress has been made in this field ever since robust resolver-type sensors were introduced to the market. Resolver has a form of an electrical machine and is used along with resolver-to-digital (R/D) converter to produce the digital position feedback. The resolution of the R/D converter is presented by the user and can be changed on-line thus making it suitable even for high performance tasks such are robot servos and precise tools machine. On the other hand, control system designers should pay attention on certain details when designing servo systems with a resolver feedback. Namely, R/D converter has the finite bandwidth which brings in a certain delay in the position feedback. Along with the finite bandwidth of the electromagnetic torque controller it can be source of unacceptable overshoot in the speed loop response. For this reason, performance limits of the R/D converter and the torque controller should be taken into account when designing the speed servomechanism.

In this paper, a straightforward tuning method of controller gains is proposed. Section 2 gives a brief description of the conventional R/D converter. The quantization effect and the finite bandwidth of R/D's tracking loop are investigated along with their influence on overall drive performance. Section 3 discusses the internal structure of the conventional torque controller. A closer insight should help the reader to model the presence of the torque controller in the speed control loop. The derivation of the criterion for the optimal tuning of controller parameters is presented in Section 4. The effectiveness of this analytical tuning procedure is confirmed by computer simulations. Concluding remarks are given in Section 5.

2. NOISE AND THE DELAY OF THE RESOLVER FEEDBACK

Advanced servo drives demand high precision shaft sensors for the needs of closing the speed and the position feedback. In practice, two types of shaft sensors are commonly used: optical encoders (absolute and incremental) and electromagnetic resolvers. Absolute optical encoders do not require any external counter logic and the shaft position is obtained directly as a digital word from the sensor. On the other hand, incremental encoders are equipped with a bidirectional (UP/DOWN) counter. Encoder pulses, with a frequency directly proportional to the shaft speed are used as a clock for the counter. Thus the counter contains a digital word representing the shaft position at every reading.

The potential weakness of both optical transducers is inability to operate in harsh industrial conditions especially when high temperature, dust, oil vapors and mechanical vibrations are involved. In such an environment, the position transducer widely used is the robust electromagnetic resolver.

The electromagnetic resolver generates sinusoidal analog voltages at the *SINE* and *COSINE* detection windings. Amplitudes and phases of these voltages contain the information on the shaft position. Resolver-to-digital converter produces a digital position estimate derived from *sine* and *cosine* signals coming from detection windings of the resolver. Conversation process is ratiometric [1], and involves closed loop position tracking. Estimated shaft position is present in an UP/DOWN counter (Fig. 1) in the form of a digital word having 10, 12, 14 or 16 bit accuracy.

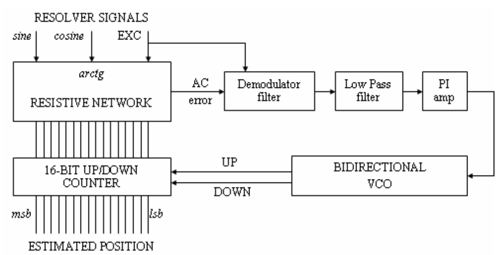

Fig. 1. Internal structure of the R/D converter.

The internal structure of the R/D converter comprises both analog and digital sections. Resolver is excited by a low power, high frequency (EXC) signal having the frequency at least an order of magnitude higher than required bandwidth of the R/D tracking loop. The *arctg* resistive network is connected to analog signals coming from electromagnetic resolver. The net is arranged in such a manner that an AC-error signal appears at the output. The error signal is proportional to the difference between the actual shaft position and the estimated shaft position contained as a word within the counter. High frequency AC error is first filtered demodulated and further processed through a PI (proportional – integral) gain block. Amplified error is used as the driving signal for a Bidirectional Voltage Controlled Oscillator (BVCO). Finally, the tracking loop is closed by feeding the BVCO output pulses to the UP/DOWN counter, thus providing with a corrective action that forces the digital position estimate to track the actual shaft position. It should be noted that R/D converter is incomplete as an observer. In general, observers should have two inputs: a feedforward input and a tracking signal *command* input. Since this feedforward input in the form of an acceleration signal is not included R/D converter produces tracking errors and the lagging estimate of the shaft position. Therefore, delay in the resolver feedback must be modeled and taken into account when tuning the speed control loop.

The R/D converter has a third order transfer function and the user definable bandwidth ranging from 520 Hz up to a few kHz. According to [1] the closed-loop transfer function of the R/D converter is given by

$$\frac{\theta_{out}}{\theta_{in}} = \frac{14(1+s_N)}{(s_N+2.4)(s_N^2+3.4s_N+5.8)} \tag{1}$$

where, s_N denotes the normalized frequency variable

$$s_N = \frac{2}{\pi}\frac{s}{f_{bw}} \tag{2}$$

and f_{bw} is the closed-loop -3 dB bandwidth.

By neglecting high frequency terms in (1), the transfer function could be rewritten as follows

$$\frac{\theta_{out}}{\theta_{in}} \approx \frac{1}{(\tau_{1n}s_N+1)(\tau_{2n}s_N+1)} \tag{3}$$

where, τ_{1n} = 1/2.4 and τ_{2n} = 3.4/5.8 are normalized time constants. The transfer function (3) could be further simplified using the Eq.(12) derived in Section 4. Thus the resulting normalized time constant τ_{rdn} can be found as

$$\tau_{rdn} = \sqrt{\tau_{1n}^2 + \tau_{2n}^2} = 0.7192. \tag{4}$$

Finally, with the respect to (2) the resulting time constant τ_{rd} becomes

$$\tau_{rd}[\mathrm{s}] = \tau_{rdn}\frac{2}{\pi f_{bw}[\mathrm{Hz}]} = \frac{0.4578}{f_{bw}[\mathrm{Hz}]}. \tag{5}$$

If the corner frequency f_{bw} is set than, we adopt the following first order transfer function as a model of the R/D converter

$$\mathrm{W_{rd}}(s) = \frac{1}{1+\tau_{rd}s}. \tag{6}$$

Step response curves for transfer functions (1) and (6) are shown in Fig.1 assuming the typical 1 KHz corner frequency of the R/D converter.

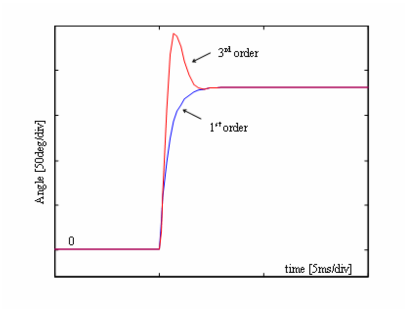

Fig. 2. Step response of the 3rd order and the simplified 1st order transfer functionof the R/D converter.

The simplified first order transfer function (6) represents the low frequency model of the third order transfer function (1). However, due to the fact that missing high frequency modes are suppressed by the low-pass nature of the speed control loop the difference between "exact" and modeled dynamic is negligible and therefore acceptable.

Another important aspect common to all position transducers is the quantization noise. In general, the resolution of the position measurement $\Delta\theta$ is determined by the number of bits N used to track the shaft position and is found to be as $\Delta\theta$ [rad] = $2\pi/2^N$. Depending on how we obtain the estimated shaft speed the speed feedback will be more or less contaminated by the quantization noise. In case of the least complicated speed estimation (back difference), the resolution of the speed measurement is $\Delta\omega$ [rad/s] = $\Delta\theta/T$ where T denotes the sampling period of the speed control loop. If the conventional PI controller is used for regulating of the motor shaft speed than, the ripple in the torque reference can be found as Δm [Nm] = $(Kp + Ki)\Delta\omega$ where Kp and Ki denote respectively proportional and integral gain of the controller. As a result, ripple in the torque reference produces oscillations of the motor shaft and increases power losses due to the pulsating current. Better results can be achieved if the speed estimate is obtained by means of software velocity estimation [2]. The proposed speed observer presents an optimal third order low-pass filter. Since the speed observer intrinsically brings in the differentiation and a filtering of the position signal, the estimated speed contains an undesirable noise as well. In both cases, the resolution of the speed measurement $\Delta\omega$ appears to be source of "chattering" in the torque reference command. Therefore, the only way to essentially reduce the quantization noise in the speed feedback is to increase the resolution of the position measurement. Due to optical problems the number of markers on the encoder disc is limited and the highest possible resolution is 11- to 12-bits. Better results can be obtained using the R/D network for sensing the shaft position.

R/D converter has a unique feature that allows the resolution to be set by the user. Furthermore, the resolution can be changed on-line [3]. Thus, the lower N resolution is used at high shaft speeds, while switching to higher N resolution in low-speed mode of operation. Most of R/D converters available have four possible combinations and the resolution N can be set to 10, 12, 14 or 16-bits. Each resolution determines the range of the shaft speeds that R/D converter is able to track. This limitation comes from the limited pulse frequency of BVCO which is typically f_{max} = 1 MHz [1]. Hence, the R/D converter is not able to track the shaft position at a speed higher than ω_{max} [rps] = f_{max} [Hz] / 2^N where ω_{max} denotes the top speed in revolutions per second, assuming that resolver has one pair of poles. Generally, the top mechanical speed is obtained by dividing the value ω_{max} by the number of resolver pole pairs.

Resolver and R/D converter appear to be the best suited solution when both robustness and high precision of the position measurement is required. A variable resolution scheme increases the drive performance allowing a wide range of operational speeds and the significant noise rejection in the low speed operational mode. The R/D network brings in a certain delay in the position feedback and must taken into account when designing the speed servo mechanism. As shown, it is reasonable to adopt the simplified model (6) of the R/D network.

3. MODELING OF THE ELECTROMAGNETIC TORQUE CONTROLLER

The electromagnetic (EM) torque controller is the key component of all speed servomechanisms. Generally, it generates the feedforward voltage that forces stator currents to follow desired current references. In case of AC-motor based speed servo systems the current references are obtained in the IFO control algorithm [4]. The EM torque controller is usually assumed to be ideal and therefore the generated electrical torque proportional to the torque reference command. This is true when EM torque controller comprising the hysteresis current regulator in the stationary reference frame is used. Due to the instantaneous response to the current error, the stator currents trace current references with an error inferior to the hysteresis. The major drawback of this non-linear approach is the variable switching frequency dependant on the motor leakage inductance. When changed due to the parasitic capacity of power lines, the increasead switching frequency can cause a burnout of power switches. Therefore a linear current regulator operating in the synchronous d-q reference frame is preferable and is used along with the Pulse Width Modulation (PWM) scheme to drive an AC motor.

The reason to concentrate on the linear d-q synchronous field oriented regulator is based on the well known fact that the control of the three phase currents in the synchronous reference frame has the ability to operate with zero error. The PWM technique implies the fixed switching frequency which resolves the synchronization problem in the DC bridge and reduces the switching losses and an audio noise. Disadvantage of this approach is the design complexity and a lack of performance when compared with the non-linear one. Therefore, performance limits of a real EM torque controller must be investigated and taken into account when tuning the speed control loop.

Fig. 3 shows the block diagram of a typical EM torque controller comprising a synchronous d-q field oriented regulator and the PWM inverter.

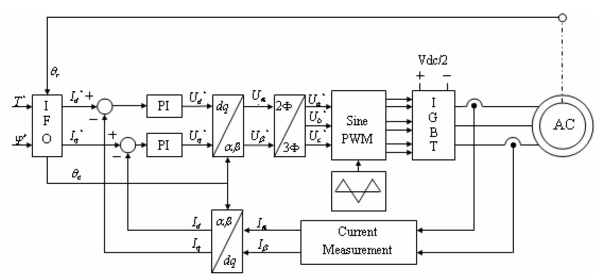

Fig. 3. Typical configuration of the EM toque controller.

Current references I_d^* and I_q^* for the synchronous d-q field oriented regulator are obtained in the IFO control algorithm processing the torque reference command T^* and the flux reference Ψ^*. The conventional PI control law is used to obtain feedforward voltage references U_d^* and U_q^*. The references are then converted from the d-q system into a three phase set of sinusoidal voltages using θ_e as an argument for vector rotator calculations. Position of the d-q reference frame θ_e is determined in the IFO control algorithm. Finally, the voltage references U_a^*, U_b^* and U_c^* are compared with a single triangle oscillator in order to obtain firing pulses for the DC bridge. In order to close both current loops, stator currents need to be measured and brought into the processor as shown in Fig. 3. In practice, two different methods are used to obtain the digital current feedback signals I_α and I_β.

First method uses a fast A/D conversion with the doubled sampling frequency. Two current samples are taken for each current component in every period of PWM. Samples are taken at the center of t_{on} and t_{off} periods. Digital feedback signals I_α and I_β are then determined as an average value of the current samples thus eliminating the influence of the current ripple.

Second method uses two VCOs and two digital counters to obtain the digital current feedback signals I_α and I_β . Here, analog voltages proportional to the measured current components in the α-β reference frame are sent to VCOs. The pulses generated, with a frequency directly proportional to the measured currents, are used as a clock for counters. Thus counters contain, at every reading, values directly proportional to the ampere seconds flowing to the load. The time derivative of these measurements results in I_α and I_β components of the measured current. Digital feedback signals I_α and I_β are then processed through the vector rotator calculations thus closing the current loop.

Both methods outlined above use some sort of averaging to produce the current feedback. It can be said that the digital representation of the measured current represents the value of the fundamental current waveform at the center of the integrated period. In other words, the obtained digital current feedback can be treated as a value of the sampled current having a latency of $\Delta T/2$, where ΔT denotes the sampling period of the current loop. The PWM inverter and processor calculations involve additional time delays in the current loop and can be modeled with a resulting latency of $3\Delta T/2$ (ΔT for processor calculations and additional $\Delta T/2$ due to the nature of PWM). For relatively short time of the PWM period, the simplification could be made that the voltage across the main inductance remains constant. For these frequencies, the influence of the stator resistance is negligible so we could use the equivalent leakage inductance $L\sigma$ as the model of an AC motor when driven by the PWM inverter. Considering these facts it is possible to adopt the model of the current loop as shown in the following Figure:

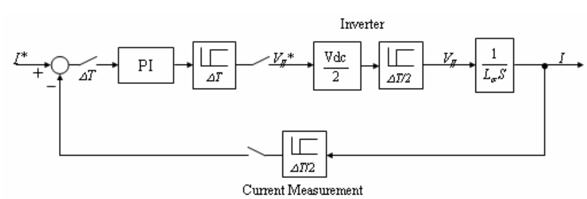

Fig. 4. Block diagram of the current loop for d or q axis.

The PI regulator in the Fig. 4 can be easily tuned to give a well damped aperiodical step response. Obviously, the current loop bandwidth is sampling period dependant. Since the sampling period ΔT is related with the PWM period T_{pwm} as $\Delta T = kT_{pwm}$ (k = 1, 2, 3, …) this configuration of an EM torque controller have a relatively slow response when compared with non-linear one. Therefore, the finite bandwidth of the EM torque controller must be taken into account when tunung the speed control loop. If the regulator in Fig. 4 is tuned for the required bandwidth than, we adopt the following first order transfer function as a model of the EM torque controller

$$\mathrm{W_{em}}(s) = \frac{1}{1+\tau_{em}s}\,, \tag{7}$$

where, τ_{em} is the resulting time constant.

Such a simplification is allowed since the bandwidth of the EM torque controller is much higher then the bandwidth of an optimally tuned speed control loop. Also, the simplified model (7) enables the derivation of the criterion for optimal tuning of speed controller parameters.

4. THE SPEED CONTROLLER PARAMETER SETTING

Fig. 5 shows the detailed structure of the speed servo system with the resolver feedback and mechanical subsystem having inertia J. In the plant of the system in Fig. 5 ω_{ref}, ω, T_L and T denote respectively the speed reference, the shaft speed, the load torque disturbance and the sampling period.

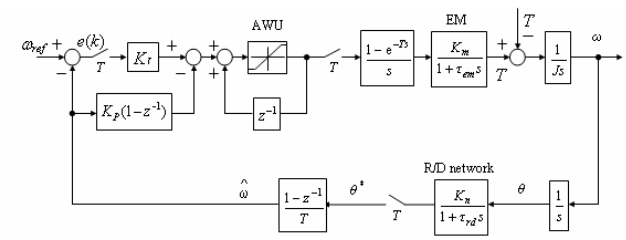

Fig. 5. Block diagram of the speed servomechanism.

For the control of the motor shaft speed the conventional digital PI (proportional-integral) controller is used. Due to the integral action the proposed speed servomechanism operates with zero steady-state speed error in the presence of a constant or a slow-varying torque disturbance. The digital PI controller is implemented in the incremental form suitable for implementation of an Anti-Windup (AWU) mechanism. The speed feedback is obtained using the least complicated method of velocity estimation – the backward difference. In the plant of the system in Fig. 5 parameters K_p and K_i denote the proportional and the integral gain of the speed controller. Also, we introduce the coefficient C, comprising the motor inertia J, the static gain of the EM torque controller K_m, the sampling period T and the ratio $K_n = 2^N/2\pi$ of the R/D converter

$$C = \frac{K_m K_n T}{2J}\,. \tag{8}$$

Since the PI controller in the plant with double integrator allows only one degree of freedom, transfer functions (6) and (7) of the R/D network and the EM torque controller respectively must be substituted with the equivalent one as follows

$$\mathrm{W_e}(s) = \frac{1}{1+\tau_e s}\,. \tag{9}$$

The resulting time constant τ_e can be found from the following identity:

$$20\log\left|\mathrm{W_e}(s)\right| = 20\log\left|\mathrm{W_{rd}}(s)\cdot \mathrm{W_{em}}(s)\right| = -3 \text{ dB}. \tag{10}$$

After substituting (6) and (7) in (10), we obtain

$$\begin{aligned}&\frac{1}{\sqrt{1+\tau_e^2\omega^2}} = \\ &= \frac{1}{\sqrt{1+(\tau_{rd}^2+\tau_{em}^2)\omega^2+(\tau_{rd}\tau_{em})^2\omega^4}} = \frac{1}{\sqrt{2}}\end{aligned}\,. \tag{11}$$

From the above identity we conclude that resulting time constant τ_e is given by

$$\tau_e = \sqrt{\tau_{rd}^2 + \tau_{em}^2}\,. \tag{12}$$

For these frequencies, the fourth order term in (11) can be neglected which justifies the simplification made in (12). Finally, the transfer function (9) can be transformed from continuous into the z–domain as follows

$$\mathrm{W_e}(z) = \mathrm{Z}\{\mathrm{W_e}(s)\} = \frac{1-\beta}{1-\beta\, \mathrm{z}^{-1}}\,. \tag{13}$$

The coefficient β in (13) is given by $\beta = \exp(-T/\tau_e)$.

From the system block diagram in Fig. 5 the speed error $E(z)$, with respect to the step input $\omega_{ref}(z)$ can be derived as

$$E(z) = \frac{z\left[(z-1)(z-\beta)+K_pC(1-\beta)(z+1)\right]}{f(z)}\omega_{ref} \tag{14}$$

where, $f(z)$ represents the closed-loop system characteristic polynomial

$$\begin{aligned}&\mathrm{f(z)} = \mathrm{z}^3 + z^2\left[-2-\beta+(\mathrm{K_pC}+\mathrm{K_iC})(1-\beta)\right]+ \\ &+\mathrm{z}\left[1+2\beta+\mathrm{K_iC}(1-\beta)\right]-\beta-\mathrm{K_pC}(1-\beta)\end{aligned}\,. \tag{15}$$

It is desired to obtain the aperiodical step response of the torque reference command and the regulated shaft speed. Due to proposed controller structure in Fig. 5, the speed error will not change the sign and therefore optimal values of the controller parameters K_p and K_i may be determined by minimizing the performance index

$$\xi = \sum_{k=0}^{+\infty} e(kT)\,. \tag{16}$$

The performance index (16) can be calculated as

$$\xi = E(1) = \frac{2K_pC(1-\beta)}{f(1)}\omega_{ref} = \frac{K_p}{K_i}\omega_{ref}\,. \tag{17}$$

Hence, the adjusting of the controller parameters is reduced to the problem of determining the minimal value of (17) under the constraint that all closed-loop system poles are real, positive and inside the unit disc of the z-plane. Let us assume that system closed-loop poles are σ_1, σ_2 and σ_3. Then, according to (15), we have

$$\sigma_1\sigma_2\sigma_3 = \beta + K_pC(1-\beta) \tag{18a}$$

$$\sigma_1\sigma_2+\sigma_1\sigma_3+\sigma_2\sigma_3 = 1+2\beta+K_iC(1-\beta) \tag{18b}$$

$$\sigma_1+\sigma_2+\sigma_3 = 2+\beta-(K_pC+K_iC)(1-\beta) \tag{18c}$$

or, after summing (18),

$$\sigma_1\sigma_2\sigma_3+\sigma_1\sigma_2+\sigma_1\sigma_3+\sigma_2\sigma_3+\sigma_1+\sigma_2+\sigma_3 = 3+4\beta\,. \tag{19}$$

Substituting (18a) and (18b) into the (17), the performance index can be calculated as

$$\xi = \frac{\sigma_1\sigma_2\sigma_3-\beta}{\sigma_1\sigma_2+\sigma_1\sigma_3+\sigma_2\sigma_3-1-2\beta}\omega_{ref}\,. \tag{20}$$

The minimum of (20) is obtained by analytical search to be for

$$\sigma_1 = \sigma_2 = \sigma_3 = \sigma_{opt} = \sqrt[3]{4+4\beta} - 1 . \qquad (21)$$

Finally, from equations (18a) and (18b), the optimal values of controller parameters are found to be

$$K_p = \frac{\sigma_{opt}^3 - \beta}{(1-\beta)C} \qquad (22a)$$

$$K_i = \frac{3\sigma_{opt}^2 - 1 - 2\beta}{(1-\beta)C} . \qquad (22b)$$

Equation (22) was used to calculate numerical values of optimal controller gains for frequencies $1/\tau_{rd}$ and $1/\tau_{em}$ and for the sampling period T given in Table 1. For the sake of simplicity, parameters K_m and K_n are taken to be $K_m = K_n = 1$. The inertia of the mechanical subsystem in Fig. 5 is $J = 0.001$ kgm^2. The calculated values are put in Table 1.

Table 1. Optimal values of controller gains.

$1/\tau_{rd}$ [rad/sec]	$1/\tau_{em}$ [rad/sec]	T [s]	β	C	σ_{opt}	K_p	K_i
2000π	500π	0.001	0.2179	0.5	0.6952	0.3020	0.0362
		0.0003	0.6331	0.15	0.8693	0.4349	0.0203

Note that optimal controller gains K_p and K_i can be easily calculated if some of the parameters within the synthetical C parameter are changed. This can be particulary usefull in speed servo systems where inertia J is subject to change. In such cases, optimal controller gains K_p and K_i can be recalculated on-line thus eliminating the use of memory-consuming look-up tables.

For the pertinent value of the parameter C and for corresponding optimal values of controller parameters K_p and K_i, the system in Fig. 5 was simulated, and the simulation results are given in Fig. 6 and Fig. 7. Evidently, the results are in agreement with expected step responses.

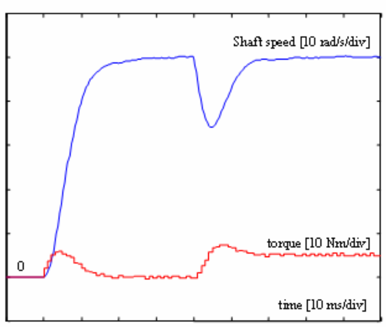

Fig. 6. Step response of the system with the sampling period T = 0.001 s.

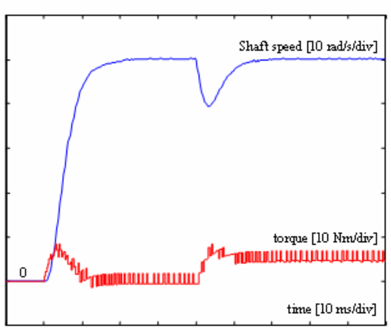

Fig. 7. Step response of the system wih the sampling period T = 0.0003 s.

The simulations are made on the system in Fig. 5 taking into account the 12-bit resolution of the R/D converter. In both cases, the strictly aperiodical step responses of the speed control loop are obtained using controller gains from Table 1. A zero steady-state speed error in the presence of a step torque disturbance is achieved in both cases as well. At the same time, Fig. 7 shows that the permissible sampling rate T is bounded for the basic configuration such as one proposed in Fig. 5. Due to the high sampling frequency, the torque reference contains an unacceptable "chattering" as shown in Fig. 7. As proposed in Section 2, a well estimated peak-to-peak values of the torque ripple are $\Delta m_1 \approx 0.5$ Nm and $\Delta m_2 \approx 2.32$ Nm for the torque reference traces in Fig. 6 and Fig. 7 respectively. To resolve the problem of torque reference pulsations, the speed feedback can be obtained using the extended speed observer as proposed in [2]. Thus the basic configuration shown in Fig. 5 with an optimally tuned PI gains can serve as a starter point for implementation of high-performance industrial speed servo drives.

5. CONCLUSIONS

The structure of the speed servo system and the novel method for optimal setting of controller parameters are proposed in this paper. The conventional PI controller is tuned to give a strictly aperiodical step response of the speed control loop when finite bandwidts of EM torque controller and R/D converter are taken into account. Results of analytical design are verified by computer simulations. Note that the suggested tuning procedure can be applied, with minor modifications, to speed servo systems with different kind of electrical motors.

REFERENCES

[1] Analog Devices Inc.: *Design-in-reference manual: Data converters, amplifiers, special linear products, support components,* 1994.

[2] Milic Stojic and Slobodan Vukosavic: *Design of the observer-based speed controller applied in servo drives with limited resolution of position sensors,* Facta Universitatis, Nis, 1995.

[3] Franco Talpone, Mario Salano, Slobodan Vukosavic, Ljiljana Peric: *On-line resolution switching of R/D converter,* Proceedings of the ANAE Conf. on Variable Speed Drives, Bresanone, Italy, 1996.

[4] Luis J. Garcés: *Current Control of Field Oriented AC Induction Motor Drives,* in *Field Orientation Control and High Performance AC Drives*, chapter V, IEEE Tutorial Course, 1989, Victor R. Stefanovic (editor).

ELIMINATING INSTABILITIES IN COMPUTER CONTROLLED MOTION CONTROL SYSTEMS CAUSED BY TORSIONAL RESONANCE

Milan Matijević, Slobodan Vukosavić, Kurt Schlacher

Abstract: *Torsional resonances are encountered in high performance motion control systems because the mechanical coupling between the motor and the load has finite stiffness. The presence of torsional resonance in motion control systems limits the maximum achievable performance and causes undesirable oscillations in the control system response. The correct application of the IMPACT (Internal Model Principle and Control Together) can eliminate the instability introduced by the torsional resonance and therefore permit higher performance levels to be achieved. This paper outlines the control strategies for compensating torsional resonance in high performance servo drives, and illustrates advantages of the proposed IMPACT structure. The special case of the IMPACT structure is proposed in order to establish the damping effect on the mechanical part.*

Keywords: *Torsional resonance, Oscillation suppression, IMPACT strucutre, Controlled electrical drives, Robust control, Distrubance rejection..*

1. INTRODUCTION

Most of the machine centers, industrial robots, servomechanisms and other rotating machinery have the geared reduction mechanisms between output shafts of motors and driven machine parts. The insufficiency of the torsional stiffness of the geared reduction mechanism often induces transient vibrations mainly related to eigenvalues of the mechanical parts in the lower-frequency range when the motor starts or stops. Elastic couplings and joints within the machine system are major impediments to the performance enhancement, since high loop gains often destabilize torsional resonance modes associated with the transmission flexibility. Vibration suppression of rotating machinery is an important engineering problem [1-7].

The problem on torsional oscillation suppression and disturbance rejection in flexible system originates in steel rolling mill systems, where the load is coupled to the driving motor by long shaft. The small elasticity of the shaft is magnified and has a vibrational effect on the load speed. Vibrations caused by the load impact and the step input endanger the integrity of the mechanical structure and detriorate the product quality. This vibration is not only undesirable but also the origin of th instability of the system in some cases. As the newly required speed response is very close to the first resonant frequency, the conventional controllers are not longer effective [3,5,6].

To overcome the problem, various control strategies have been proposed, that may be divided into the following three groups [3]: 1) control strategies based on the direct measurement of motor- and load- side variables, 2) strategies involving only one feedback device attached to the motor and the observer that estimating remaining states [5,6], and 3) vibration supression strategies based upon the notch filtering and phase-lead compensation applied in conventional control structures [3]. In this paper, a brief review of them will be given. Next, a new control strategy based on IMPACT structure will be proposed as a simple and practical control algorithm. The proposed control technique should be to satisfy new requirements in the quality of control, i.e., 1) faster speed control response, 2) disturbance rejection on the load speed, and 3) robustness to parameter variations including gear backlash. This paper will show that the IMPACT structure [7-10] is suitable for suppressing of torsional oscillations in servo drives with flexible coupling. The special case of the IMPACT structure will be proposed.

2. TORSIONAL RESONANCE AND SERVO SYSTEM WITH FLEXIBLE COUPLING

Resonance is a steady state phenomenon that occurs when motor's natural resonant frequencies are excited at particular velocities. For example, if we slowly increase motor's speed, we may notice „rough“ spots at certain speeds. The „roughness“ is resonance (Fig.1). But, it is not caused by transient reference inputs. Resonance is affected by the load. Some loads are resonant, and can make motor resonance worse. Other loads can damp motor resonance. Unlike resonance, ringing is a transient phenomenon, that can be caused both by accelerating or decelerating to a reference velocity. Namely, when controlled to quickly accelerate to a given velocity, the motor shaft can „ring“ about that velocity, oscillating back and forth. As resonance, ringing causes error in motor shaft position. Also, ringing (or vibration) can cause audible noise.

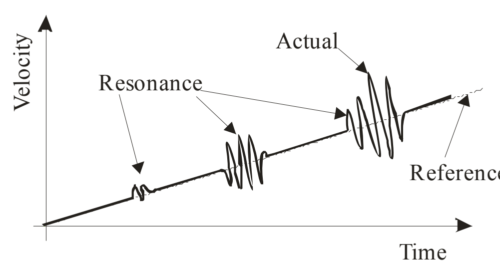

Fig.1 Ilustration of a resonance phenomenon in servo drives

In order to slove these problems, system designers will sometimes attach a damping load, such as an inertial damper, to the back of the motor. However, such a load has the undesired effects of decreasing overall performance, and increasing system cost. Again, designers of the control part of a servo system, usually use the simplest motor/load models that haven't information about resonance modes and fast dynamics.

The more realistic model of an AC motor with load is illustrated on Fig.1. and Fig.2, as a two-mass motor/load system with flexible coupling.

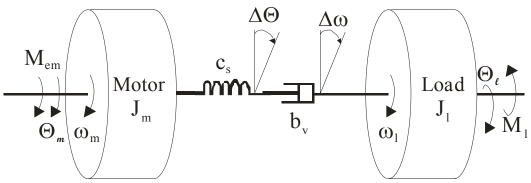

Fig.2. Flexible coupling of the motor shaft and load

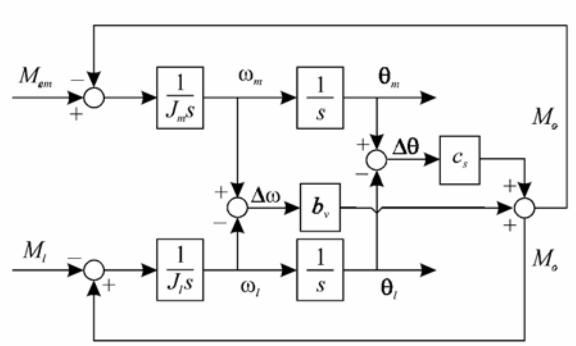

Fig.3. Block diagram of the servo system's plant with flexible coupling

The electromagnetic torque M_{em} is control variable, and the tork on loaded shaft M_l presents disturbance. The motor inertia J_m and load inertia J_l are coupled by the shaft or the transimssion system having a finite stiffness coeficient c_s. The friction coefficient b_v generally assumes very low values, giving rise to weakly damped mechanical oscillations [3]. The torsional torque M_o equals the load torque M_l only in the steady state. During transients, the speeds of motor and load differ, and torsional torque M_o is given by

$$M_o = c_s \Delta\theta + b_v \Delta\omega \quad (1)$$

Contrary to the traditional model $W_m(s)=1/(J_l+J_m)s$, if the shaft sensor is mounted on the motor, the transfer function of the mechanical subsystem is defined by

$$W_m(s) = \frac{\omega_m(s)}{M_{em}(s)} = \frac{1}{(J_m + J_l)s} \frac{1 + \frac{2\varsigma_z}{\omega_z}s + \frac{1}{\omega_z^2}s^2}{1 + \frac{2\varsigma_p}{\omega_p}s + \frac{1}{\omega_p^2}s^2} \quad (2)$$

where undamped natural frequencies (ω_p, ω_z) and relative damping coefficients (ζ_p, ζ_z) are given by

$$\omega_p = \sqrt{\frac{c_s(J_m + J_l)}{J_m J_l}},\ \omega_z = \sqrt{\frac{c_s}{J_l}},\qquad \varsigma_p = \sqrt{\frac{b_v^2(J_m + J_l)}{4c_s J_m J_l}},\ \varsigma_z = \sqrt{\frac{b_v^2}{4c_s J_l}} \quad (3)$$

Undamped natural frequency ω_p and ω_z of the pole- and zero-pairs in (2) are refered as the resonance and antiresonance frequencies [2,3], and their quotient is known as the resonance ratio

$$R_r = \frac{\omega_p}{\omega_z} = \sqrt{1 + \frac{J_l}{J_m}} \quad (4)$$

In the case under consideration, a low value of resonance ratio reduces the influence of torsional load on dynamics of the speed control loop. With $J_m>>J_l$, oscillations of torsional torque are filtered by a large motor inertia J_m and their influence on the control of the motor speed becomes smaller. A damped control of Θ_m and ω_m is favorable, but most applications require fast and precise control of the load variables Θ_l and ω_l [3]. Also, in that case, the estimation of resonance modes from detected signals (Θ_m and ω_m) is not possible, and the load speed and position might exhibit weakly damped oscillations that cannot be disclosed and compensated from the feedback signals [3].

In the case that sensor is mounted on the load shaft, the mechanical subsystem of the drive has the transfer function $W_l(s)$ given by

$$W_l(s) = \frac{\omega_l(s)}{M_{em}(s)} = \frac{1}{(J_m + J_l)s} \frac{1 + \frac{2\varsigma_z}{\omega_z}s}{1 + \frac{2\varsigma_p}{\omega_p}s + \frac{1}{\omega_p^2}s^2} \quad (5)$$

where undamped natural frequencies (ω_p, ω_z) and relative damping coefficients (ζ_p, ζ_z) are given by (3), too.

3. STRATEGIES FOR COMPENSATING TORSIONAL RESONANCE

Many controllers already exist in the field of motion control, but all most of them are designed by assuming an ideal, rigid transmission train [3]. However, the desired speed-loop bandwidth in modern machining centres approaches the frequency of torsional resonance and coincides, at the same time, with most disturbing statistical and deterministic noises. Under these condition, P&I control laws are not suitable. Standard improvement of conventional motion control laws and structures is based on antiresonant compensator inclusion as it is shown on Fig.4. Also, in the literature are proposed model based control approaches, control tehniques based on the disturbance observers, as well as approaches based on two freedom structure based on H_2 control, etc. [2-6,11].

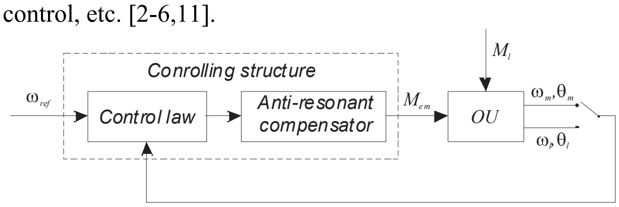

Fig.4. System with antiresonant compensator

H_2 two freedom controller (Fig.5) minimizes functional

$$\min \int_0^\infty \left(e(t)^2 + \lambda^2 u(t)^2 \right) e^{2\alpha t} dt \quad (6)$$

The software for calculation of H_2 controller (G_{fb} and G_{ff}) is available on the cite [11]. In this manner is possible to get more appropriate PI control law ($G_{fb} \equiv G_{ff}$, $G_d \equiv 1$, see Fig.5). But, as one drawback, we can note that H_2 controller design uses trial and error method in tuning parameters to meet the performance specifications (by choosing of different λ and α_h values in the simulation trials).

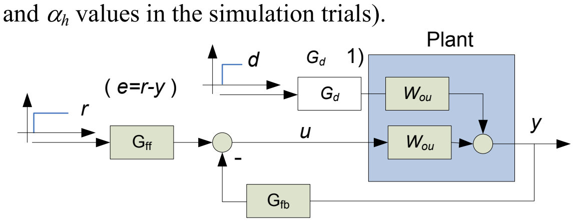

Fig.5. H_2 controlling structure

The notch filter compensator

$$W_{notch}(s)=\frac{s^2+2\varsigma_{zz}\omega_{nf}s+\omega_{nf}^2}{s^2+2\varsigma_{pp}\omega_{nf}s+\omega_{nf}^2}, \qquad (7)$$

$$\varsigma_{pp} \gg \varsigma_{zz}$$

as antiresonance comensator (Fig.4) is most frequently used in practice. The notch filter zeros cancels critical poles (of the torsional load), while the poles of the filter become a new pair of conjugate complex poles with increased relative damping ($\varsigma_{pp} \gg \varsigma_{zz}$). Digital implementation of notch filter ($\varsigma_{pp}=\varsigma_p, \varsigma_{zz}=\varsigma_z, \omega_{nf}=\omega_p$) is given by discrete transfer function

$$W_{notch}(z^{-1})=$$

$$\frac{e^{-(\varsigma_p-\varsigma_z)\omega_p T}-2e^{-\varsigma_p\omega_p T}\cos(\omega_p T\sqrt{1-\varsigma_z^2})z^{-1}+e^{-(\varsigma_p+\varsigma}}{1-2e^{-\varsigma_p\omega_p T}\cos(\omega_p T\sqrt{1-\varsigma_p^2})z^{-1}+e^{-2\varsigma_p\omega_p T}z^{-}} \qquad (8)$$

For an exact cancellation of resonance modes, both the resonance frequency and damping factor must be known while tuning all parameters of the notch filter [3]. But, the exact location of critical poles is unknown and, thus, the cancellation is generally imprecise. The notch filter (7) suppresses the resonant mode by the ratio $\varsigma_{pp}/\varsigma_{zz}$. Since a low damping coefficient of zeros increases greatly the snesitivity to parameter variations, the ratio $\varsigma_{pp}/\varsigma_{zz}$ is limited. Hence, the excitation of resonance modes can be only reduced, but not eliminated completely, by the notch serial compensator. The notch compensator si very sensitive to parameter variation, and it presents a serious problem in tuning and implementation the notch filter [3].

As a more robust and more practical solution of vibration supression strategy based upon the structure on Fig.4; in [3] is proposed antiresonance compensator

$$W_{NF}(z^{-1})=\frac{1+z^{-n}}{2},\ n=\frac{T_{osc}}{2T} \qquad (9)$$

where the n stands for the ratio between the resonance mode half-period ($T_{osc}/2$) and the sampling time (T) of the discrete time controller. The oscillation period of the resonance mode T_{osc} is given by

$$T_{osc}=\frac{2\pi}{\omega_p\sqrt{1-\varsigma_p}} \qquad (10)$$

and it is adjustable parameter of the FIR filter (8), that could be experimentally defined. The idea of the synthesis of filter (8) was elaborated in [3]. The conceived cascade antiresonance compensator is simpler, less sensitive to parameter changes, and requiring a setting of only one parameter, but parameter n have to be identified precisely. The theoretical value of the suppression at $\omega_{osc}=1/T_{osc}$ frequency is infinite, rather then a finite ζ/ζ_p notch filter suppression value.

The resonance ratio control is proposed as an improvement of model-based control techniques (i.e. model following control, application of disturbance observer, time derivate feedback, state feedback control).

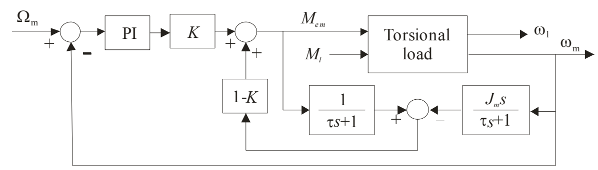

Fig.6. Resonance ratio control

The resonance ratio is defined by relation (4), and should be about $\sqrt{5}$ because of effective vibration suppression. In [6], as a simple and practical strategy, it is proposed the resonance ratio control based on the fast disturbance observer (see Fig.6 and Fig.2), with optimal resonance ratio $0.8\sqrt{5}$. In conventional disturbance observer applications 100% of the estimated disturbances is feed back. In the case on Fig.6, 1-K of the estimated disturbances is used. Parameter K ($0<K\le 1$) and time costant τ (which defines observer's cutoff frequency) are adjustable parameter for vibration suppression. But, as it is previous commented, this control strategy cannot efficiently provide vibration suppression on the load side.

A good review of control strategies of vibration supression is given in [3], where FIR antiresonant filter (9) is proposed as improvement of previous approaches. This solution is investigated and compared with IMPACT structure possibilities in [7].

4. IMPACT STRUCTURE

Fig.7 depicts the special case of IMPACT controlling structure that corresponds to control plants without the transport lag (dead time). Thus the structure may be conveniently applied for digitally controlled electrical drives [7]. In that case, signal w_M modeled the influence of load torque disturbance on system output y which may be shaft speed or angular position depending on the type of servomechanism.

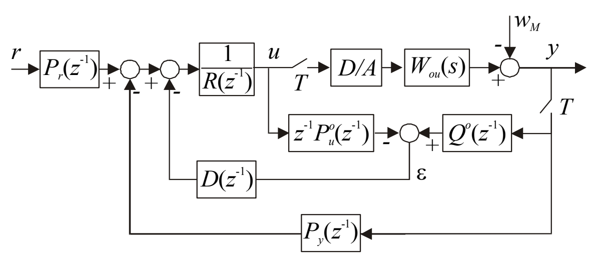

Fig. 7. IMPACT structure of digital control system

The control portion of the system of Fig.7 is given by polynomials in complex variable z^{-1}. In the IMPACT structure, the control plant $W_{ou}(s)$ is given by its simplified nominal discrete model

$$W^o(z^{-1})=\frac{z^{-1-k}P_u^o(z^{-1})}{Q^o(z^{-1})}$$

developed at the low-frequency band. This model is included into the control part of the IMPACT structure as a two-input internal plant model. Signal ε estimates effects of generalized external disturbance and uncertainness of nominal plant model on the system output. Uncertainness of nominal plant model can be adequately described by the multiplicative boundary of uncertainness.

$$W(z^{-1}) = W^o(z^{-1})(1+\delta W(z^{-1}))$$
$$\left|\delta W(e^{-j\omega T})\right| \le \alpha(\omega), \;\; \omega \in [0, \pi/T] \tag{11}$$

Then the system in Fig. 7 satisfies the condition of robust stability if the nominal system is stable and if the following inequality is fulfilled

$$\alpha(\omega) < \left| \frac{Q^o(z^{-1})R^o(z^{-1}) + z^{-1}P_u^o(z^{-1})P_y(z^{-1})}{z^{-1}P_u^o(z^{-1})(P_y(z^{-1}) + Q^o(z^{-1})D(z^{-1}))} \right|_{z^{-1}=e^{-j\omega T}}, \omega \in [0, \pi/T]$$

The robust performance is achieved by the local minor loop of the system in Fig. 7. Namely, the main role of this loop is suppression of effects of the generalized disturbance on the system output. This loop comprises internal model of disturbance implicitly and two-input nominal plant model determined by polynomials $z^{-1}P_u^o(z^{-1})$ and $Q^o(z^{-1})$, explicitly. In the case of a control plant without the dead time, the internal model of disturbance is reduced to the prediction polynomial $D(z^{-1})$.

$$(1 - D(z^{-1}))\varepsilon(z^{-1}) = 0, \; t = nT \ge (\deg(1 - D(z^{-1})))T$$

The choice of this polynomial affects the robust performance of the system and effectiveness in absorption of the given class of disturbance. For example, for constant and ramp disturbances, the proper choice of prediction polynomials are $D(z^{-1}) = 1$ and $D(z^{-1}) = 2 - z^{-1}$, respectively. Smaller sample period, has justification in the linear approximation of arbitrary signal on a limited time range. Thus, polynomial $D(z^{-1}) = 2 - z^{-1}$ refers on calsses of slowly-changing disturbances, too. In that manner, principle of absorption in IMPACT structure is implemented in the minor loop, that enables - estimation of influence of generalized disturbance, its prediction and feedforward compensation [7-10].

According to the standard procedure of IMPACT structure synthesis, for a minimum phase control plant, polynomial $R(z^{-1})$ should be taken on as $R(z^{-1}) = P_u^o(z^{-1})$.

The polynomials $P_r(z^{-1})$ and $P_y(z^{-1})$ in the main external loop of the controlling structure in Fig. 7 determine the dynamic behavior of closed-loop system and these polynomials are determined independently from the design of local inner control loop of the structure. The desired pole spectrum of the closed-loop control system may be specified by the relative damping coefficient ς and undamped natural frequency ω_n of the system dominant poles. In doing so and taking into account the required zero steady-state error for step reference signal, the desired second order discrete closed-loop system transfer function becomes

$$G_{de}(z^{-1}) = \frac{(1-(z_1+z_2)+z_1z_2)z^{-2}}{1-(z_1+z_2)z^{-1}+z_1z_2z^{-2}} \left(= \frac{z^{-1}P_r(z^{-1})}{Q^o(z^{-1}) + z^{-1}P_y(z^{-1})} \right)$$

where

$$z_{1/2} = e^{s_{1/2}T}, \quad s_{1/2} = -\varsigma\omega_n \pm j\omega_n\sqrt{1-\varsigma^2} \tag{12}$$

Then polynomials $P_r(z^{-1})$ and $P_y(z^{-1})$ are calculated in a straightforward manner from

$$P_r(z^{-1}) = (1-(z_1+z_2)+z_1z_2)z^{-1} \tag{13}$$
$$P_y(z^{-1}) = 1-(z_1+z_2)+z_1z_2z^{-1}$$

However, like it was noticed in [7,10], internal model of control structure (Fig.7) increases sensitivity of the system on quantization noise, specially in speed servosystems. As one solution of this problem, it can be suggested usage of prediction polynomials filters [8] instead the classical prediction polynomials. Generally, the predictive filter is defined as an algorithm that estimates future values of the input signal and suppresses the noise contamination [12]. The relatively simple forms of digital predictive filters corresponding to polynomial disturbances are treated. In this paper we present structure consisting of the simplest RLSN (Recursive Linear Smoothed Newton) predictor (Fig. 8) instead prediction polynomial. Parameter c_p<1 enables that the RLSN predictor has amplitude-frequent characteristic of NF filter. In [7] is shown that changes of this parameter (c_p) could influence on expansion of robust stability area in the field of medium frequencies.

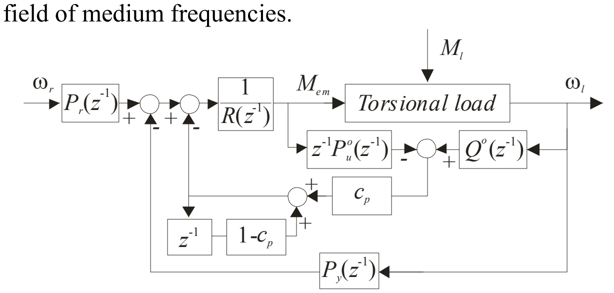

Fig.8. Modified IMPACT structure of digitally controlled speed servosystem

Synthesis of IMPACT structure starts from following plant model (see Fig.2 – flexible coupling is neglected)

$$W_{ou}(s) = \frac{1}{Js} = \frac{1}{(J_m+J_l)s}, W_{ou}(z^{-1}) = \frac{T}{J_m+J_l}\frac{}{1} \tag{14}$$

Selection of sampling period is coupled with period of torsional oscillation, so

$$T = \frac{T_{osc}}{8} = \frac{\pi}{4\omega_p\sqrt{1-\varsigma_p^2}} \tag{15}$$

Inner countour of the structure on Fig.8 contains a model of step disturbances. Because very small sampling period is selected, this internal model of disturbance is adequate solution for wider class of disturbance. Adjustment of parameters c_p simply influences on efficiency of absorption of disturbance effects or expansion of area of robust stability and suppression of torsional oscillations. The presented structure is simple with small number of adjustable parameters that could be easily set to achieve the desired robust, filtering, and dynamic properties of the system.

However, possibilities of the structure on Fig.8 to meet robust stability condition by changing parameter c_p are limited. From this reason, on Fig. 9 is proposed modified IMPACT structure.

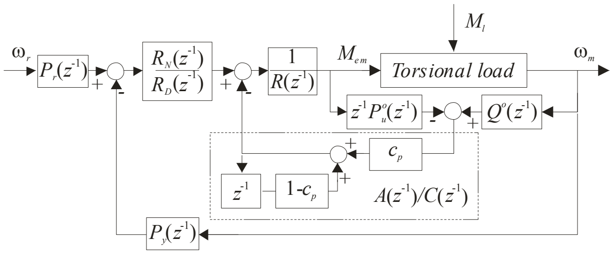

Fig.9. Modified IMPACT structure

Practically, because of elastic drive train, our goal is wide robust stability area about resonant frequency ω_p. In order to lift up frequency curve of the multiplicative bound of uncertainties of IMPACT structure about resonant frequency ω_p, we can choose following polinomial $R_N(z^{-1})$

$$R_N(z^{-1}) = 1 - 2e^{-\varsigma\omega_p T}\cos(\omega_p T\sqrt{1-\varsigma^2})z^{-1} + e^{-2\varsigma} \quad (16)$$

where, smaller paremeter ς means wider robust stability area about resonant frequency ω_p. In the special case, in oreder to expand robust stability area about resonant frequency ω_p, polinomial (16) can be factor of implicit disturbance internal model $A(z^{-1})$, too.

The polynomials $P_r(z^{-1})$, $P_y(z^{-1})$ and $R_D(z^{-1})$ in the main external loop of the controlling structure in Fig.9 determine the dynamic behavior of closed-loop system and these polynomials are determined independently from the design of local inner control loop of the structure

$$G_{de}(z^{-1}) = \frac{(1-(z_1+z_2)+z_1z_2)z^{-2}}{1-(z_1+z_2)z^{-1}+z_1z_2z^{-2}}\frac{T_p(z^{-1})}{T_p(z^{-1})}$$
$$\left(= \frac{z^{-1}P_r(z^{-1})R_N(z^{-1})}{Q^o(z^{-1})R_D(z^{-1})+z^{-1}P_y(z^{-1})R_N(z^{-1})} \right) \quad (17)$$

Selection of $T_p(z^{-1})$ is free, but poles of polinomial $T_p(z^{-1})$ should be stable and good damped.

As in previous case, according to the standard procedure of IMPACT structure synthesis, for a minimum phase control plant, polynomial $R(z^{-1})$ should be taken on as $R(z^{-1}) = P_u^o(z^{-1})$.

5. ILLUSTRATIVE EXAMPLE

The proposed control algorithms based on IMPACT structure are tested by simulation trials, under the same conditions as performed in [3]. In [2], two identical motors are interconnected by elastic hollow shaft. Motors are independently controlled and used as a motor and a load. The electromagnetic resolver is placed on both of them. We distinguish following important data (see Fig.2) J_m=0.000620kgm^2, J_m=0.000220kgm^2, $c_s = 350 Nm/rad$, $b_v = 0.004 Nms/rad$.

Fig.10 shows simulation results of IMPACT structure presented on Fig.8. Results presented on Fig.10 are slightly better then analog simulation and experimental results concerning with antiresonance compensator (9), presented in [3]. The system simulation is performed when the sensor is placed on loaded shaft (Fig.8), with selected characteristic c_p=0.2, and following polynomials of control structure: $R(z^{-1}) = P_u^o(z^{-1}) = 0.636881$, $Q^o(z^{-1}) = 1 - z^{-1}$, $P_r(z^{-1}) = 0.03941938z^{-1}$ and $P_y(z^{-1}) = -0.702 + 0.741z^{-1}$. As in [3], the same input signals ($\omega_r(t)$=3·h(t-0.05) [rad/s], $M_l(t)$=1·h(t-0.1) [Nm]) are used (see Fig.3 and Fig.8). The desired close-loop system transfer function is specified by undamped natural frequency ω_n=400 rad/s and relative damping coefficient ζ=0.7.

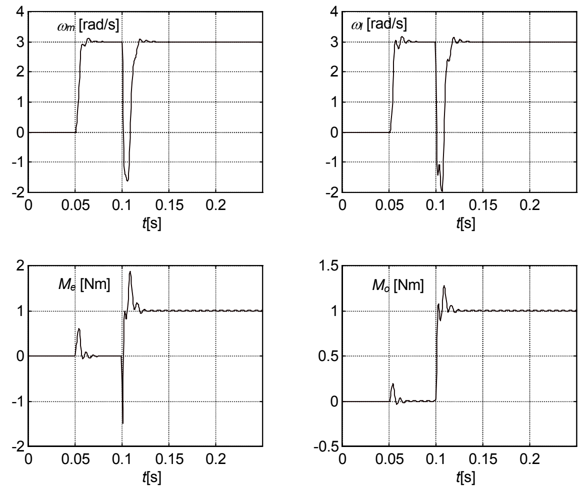

Fig.10. Operation of IMPACT structure on Fig.8 (c_p=0.2, ω_n=400 rad/s, ζ=0.7, $\omega_r(t)$=3·h(t-0.05) [rad/s], $M_l(t)$=1·h(t-0.1) [Nm])

But, our aim is to control the load shaft speed in the presence of torsional vibration, system parameter variation, disturbance torque, and in the absence of a dedicated loadside speed sensor. Robustness and efficinecy of IMPACT structure proposed on Fig.9 is illustrated on Fig.11. and Fig.12. As on Fig.9 illustrated, the sensor is mounted on motor shaft, and in that case the system simulation is performed.

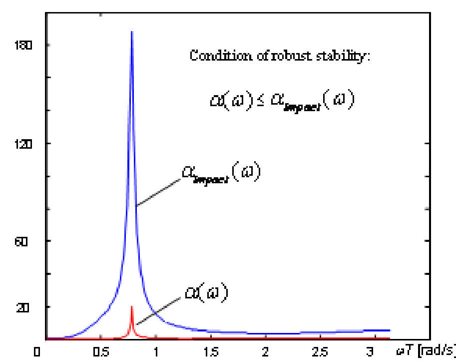

Fig.11. The multiplicative bound of uncertainties of IMPACT structure

Namely, the same experimental conditions as in [3] and the previous case are simulated (plant characteristics, torsional load, input signals). According to described procedure synthesis, polinomials of controling structure on Fig. 9 are defined. As inner contour filter $A(z^{-1})/C(z^{-1})$, again adopted simple RLSN predictor with c_p=0.2. Polinomials $R(z^{-1}) = P_u^o(z^{-1}) = 0.636881$ and $Q^o(z^{-1}) = 1 - z^{-1}$ are same as in the previous case. As the tuning parameter ς of (16) is choosen ς = 0.025, and polinomial $R_D(z^{-1})$ is $R_D(z^{-1}) = 1 - 1.55951z^{-1} + 0.06594z^{-2}$. In order to can solve Diophant's equation from (17), polinomial $T_p(z^{-1}) = (1-0.9z^{-1})(1-0.1z^{-1})$ is adopted. From (17) following polynomials of control structure $P_r(z^{-1}) = z^{-1}(0.03711 + 0.014363z^{-1} - 1.242112z^{-2} - 0.03324z^{-3})$ and $P_y(z^{-1}) = -0.055199 + 0.061z^{-1}$ are calculated.

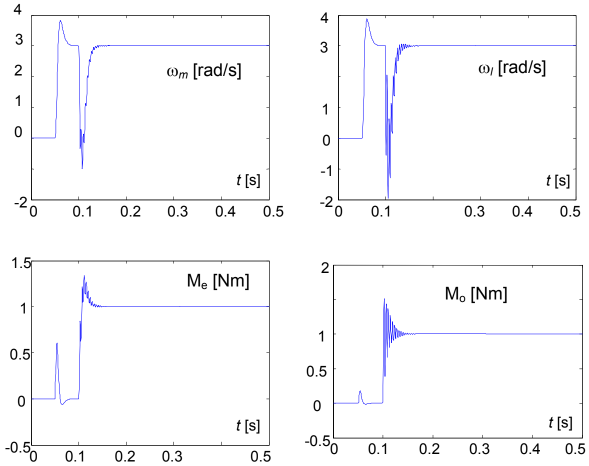

Fig.12. Operation of IMPACT structure on Fig.9 (c_p=0.2, ω_n=400 rad/s, ζ=0.7, $\omega_r(t)$=3·h(t-0.05) [rad/s], $M_l(t)$=1·h(t-0.1) [Nm])

6. CONCLUSION

Mechanical resonance is a current problem in servo systems, and falls into two categories: low-frequency and high-frequency. High-frequency resonance usualy causes instability at the natural frequency of the mechanical system, typically between 500Hz and 1200Hz. Low-frequency resonance occurs more often in general industrial machines, at the first phase crossover, typically between 200Hz and 400Hz. Standard servo control laws are structured for rigidly coupled loads. However, instability results when a such high-gain control law is applied to a flexible coupled servo system. Often, the resultin rigidity of the transmission is so low that instability results when servo gains raised to levels necessary to achive desired performance.

This paper presents several methods for dealing with torsional resonance in servo drives, and proposes a special case of the IMPACT strucutre in order to improve the existing control structures and motion control algorithms to make them compatible with mechanical subsystem. The antiresonant feature of the structure is not based on the exact cancellation of resonance poles. Due to the simplicity and robustness of the proposed structure, it can be easily applied to various flexible systems with different regulator combinations.

REFERENCES

[1] G. J. Schneider, „Taming Resonance in Servos", *Machine Design*, Vol. 57, No. 3, Feb. 7, 1985.
[2] K. Sugiura and Y. Hori, "Vibration suppression in 2- and 3-mass system based on the feedback of imperfect derivative of the estimated torsional torque," *IEEE Trans. Ind. Electron.*, vol. 43, pp. 56–64, Feb. 1996.
[3] S.N. Vukosavic and M.R. Stojic, „Suppression of torsional oscillations in a high-performance speed servo drive", *IEEE Trans. on Industrial Electronics*, vol. 45, N^{o}1, 108-117, 1998.
[4] J. Y. Hung, "Control of industrial robots that have transmission elasticity,"*IEEE Trans. Ind. Electron.*, vol. 38, pp. 421–427, Dec. 1991.
[5] M. Itoh and H. Yoshikawa, „Vibration suppression control for an articulated robot: Effects of model-based control applied to a waist axis", International Journal of Control, Automation, and Systems Vol. 1, No. 3, September 2003
[6] Y.Hori, „A review of torsional vibration control methods and a proposal of disturbance observer-based new techniques", 13th IFAC World Congress, San Francisco, 1996.
[7] M.S. Matijevic, *Development of new structures of digitally controls electromotor drives and industrial processes*, PhD thesis, Faculty of Mechanical Engineering, Kragujevac, 2001. (in Serbian)
[8] Ya.Z Tsypkin, „Design of robust optimal control systems having plants with bounded parameter uncertainties", *Avtom.Telemech.*, N^{o}9, (1992.), 139-159, (in Russian)
[9] Ya.Z. Tsypkin and U. Holmberg, „Robust stochastic control using the internal model principle and internal model control", *Int. J. Control*, vol. 61, N^{o}4, 809-822, 1995.
[10] M.S. Matijevic, M.R. Stojic, „IMPACT structure – possible improvement and applications", *Tehnika-Elektrotehnika*, vol.54, N^{o}5, Belgrade, (2005) (in Serbian)
[11] http://regpro.mechatronik.uni-linz.ac.at/
[12] S.Väliviita, Ovaska and O.Vainio, „Polynomial predictive filtering in control instrumentation: A review", *IEEE Trans. on Industrial Electronics*, vol. 46, N^{o}5, 876-888, 1999.

DIRECT TORQUE CONTROLLED INDUCTION MOTOR DRIVE BASED ON DOUBLE FEEDBACK STRUCTURE

Petar Matić, Dejan Raca, Branko Blanuša, Slobodan N. Vukosavić

Abstract: *In this paper sensorless Direct Torque Control (DTC) algorithm for induction machine (IM) drive based on simultaneous control of both radial and tangential components of stator flux vector is presented. Robustness of the drive is achieved through introduction of two PI regulators into inner double feedback stator flux control structure. Presented algorithm has no current-control loops, neither coordinate transformations. Performance of the proposed DTC algorithm is investigated and demonstrated by computer simulation.*

Keywords: *Direct Torque Control, Induction Machine Drive, Field Acceleration Method.*

1. Introduction

Decoupled control of torque and flux is required in high performance industrial and servo drives. This is commonly achieved through the Field Oriented Control (FOC), which is based on decoupling of the torque – producing and flux – producing components of stator current vector, or Direct Torque Control (DTC), which is based on direct control of stator voltage without inner current control loop [1].

FOC drive scheme requires fast current regulators and reference frame transformations. Current regulation in voltage source inverters is achieved by various configurations of the regulator. Some examples are: nonlinear hysteresis regulation [1], feed-forward regulation [2, 3, 5], internal model control structures (IMC) [4], synchronous or steady state frame regulators [1, 5, 6] etc. Quality of current regulation in FOC drives affects drive performance to a large extent. Widely used FOC algorithms are based either on rotor flux regulation (RFOC algorithms) or on stator flux regulation (SFOC). In both cases respective flux components are kept constant below the base speed (base speed region), and decreased proportionally to the rotor speed above the nominal value (field weakening region) by regulating appropriate current components.

In RFOC structures fast torque regulation in base speed region is achieved by changing torque producing stator current component while magnetizing current component is kept constant to produce desired value of rotor flux. Any change in torque will result in change of active stator current component, machine slip, and stator flux and voltage. Magnetizing stator current and rotor flux will stay constant in base speed region, and will be changed only if flux level is changed. Above the base speed (field weakening region), both magnetizing and active current components are changed. In SFOC structure, torque regulation is achieved by simultaneous change of both active and magnetizing stator current components to keep stator flux constant in base speed region because change in torque requires change of rotor flux, slip, synchronous speed and voltage. To obtain stator flux constant, an “decoupling term” in machine model should be introduced [6, 7, 8]. Field weakening operation also requires variation in both current references.

The apparent simplicity of RFOC schemes in base speed region is the main reason for their popular over SFOC. However, maintaining reference frame orientation in synch with rotor flux reduces this advantage of RFOC.

Typically current response of FOC drives is considered to be ideal and only outer (speed or position) loop is considered. This assumption is invalid in field weakening region. Full order drive model needs to be used in this regime. Back emf is close to maximum available voltage and voltage margin is not sufficient to establish desired current levels and/or dynamics [9, 10-13]. Unlike the base speed region, the RFOC voltage model includes dominant cross-coupling speed dependent voltage term along with the resistive voltage drop, and back emf [3, 5]. Under the same conditions SFOC equations consist of only the last two terms (there is no cross-coupling). This makes SFOC better suited for field weakening as it does not require cross-coupling compensation, IMC, or any other complex regulation technique [6, 14].

A large number of algorithms which tend to use benefits of both structures by regulating stator or rotor flux and using stator voltage equations in fixed reference frame were proposed with the inner current regulators are eliminated [15-20]. This approach is commonly called direct torque control (DTC). In order to regulate rotor flux, these structures must include frame transformations, which are not necessary when stator flux is controlled [19-21].

Usual DTC concpets are based on inverse model of IM [7, 15, 16, 18-21] and therefore are parameter sensitive. In this paper, inverse IM model is used only for determining physical phenomena of DTC concept based on control both radial and tangential components of stator flux. Instead of using dead-beat structure [7, 22] or frame transformations [15, 16, 18-21], a simple structure based on two PI regulators in feedback structure is used. This structure enables robust control and is parameter variation insensitive in contrast to usual DTC inverse model based concepts. Rotor flux variations due to torque variations are compensated naturaly via stator flux vector accelerartion. Proposed solution is described analitically and then confirmed by computer simulation.

2. Mathematical Background

The state space equations of induction machine in stationary reference frame are given in discrete time, complex vector form in (1) through (6).

$$\frac{\Delta\bar{\lambda}_s(k)}{\Delta t} = \bar{V}_s(k) - R_s \bar{I}_s(k), \tag{1}$$

$$\frac{\Delta\bar{\lambda}_r(k)}{\Delta t} = -R_s \bar{I}_r(k) + j\omega(k)\bar{\lambda}_r(k), \tag{2}$$

$$\bar{\lambda}_s(k) = L_s \bar{I}_s(k) + L_m \bar{I}_r(k), \qquad (3)$$

$$\bar{\lambda}_r(k) = L_r \bar{I}_r(k) + L_m \bar{I}_s(k), \qquad (4)$$

$$T_e(k) = \frac{3P}{2}\left(\bar{\lambda}_s(k) \times \bar{I}_s(k)\right), \qquad (5)$$

$$\omega(k) = P\omega_m(k), \qquad (6)$$

where $\bar{\lambda}_s(k)$ is the d – and q – axes stator flux complex vector with $\bar{\lambda}_s(k) = \lambda_{sd}(k) + j\lambda_{sq}(k)$, $\bar{\lambda}_r$ is the d – and q – axes rotor flux complex vector with $\bar{\lambda}_r(k) = \lambda_{rd}(k) + j\lambda_{rq}(k)$, $\bar{V}_s(k)$ is the d – and q – axes stator voltage complex vector with $\bar{V}_s(k) = V_{sd}(k) + jV_{sq}(k)$, $\bar{I}_s(k)$, $\bar{I}_r(k)$ are the d – and q – axes stator and rotor current complex vector with $\bar{I}_s(k) = I_{sd}(k) + jI_{sq}(k)$, $\bar{I}_r(k) = I_{rd}(k) + jI_{rq}(k)$, R_s and R_r are stator and rotor resistance, L_s and L_r are stator and rotor self – inductance, L_m is mutual inductance, $T_e(k)$ is the electromagnetical torque, P is pole – pair number, $\omega_m(k)$ and $\omega(k)$ are mechanical and electrical speed, and j is imaginary unit. Core losses and saturation are neglected in the proposed model. During the sampling instant Δt rotor speed can be treated as constant.

Changes in fluxes can be expressed as:

$$\Delta\bar{\lambda}_s(k) = \bar{\lambda}_s(k+1) - \bar{\lambda}_s(k), \qquad (7)$$

$$\Delta\bar{\lambda}_r(k) = \bar{\lambda}_r(k+1) - \bar{\lambda}_r(k), \qquad (8)$$

and change in motor torque can be expressed using an operating point model of (5):

$$T_e(k) = \frac{3P}{2}\left\{\Delta\bar{\lambda}_s(k) \times \bar{I}_s(k) + \bar{\lambda}_s(k) \times \Delta\bar{I}_s(k)\right\}. \qquad (9)$$

As shown in [21], change in machine torque expressed using only stator quantities can be found from the equivalent circuit of induction machine shown in Fig. 1.

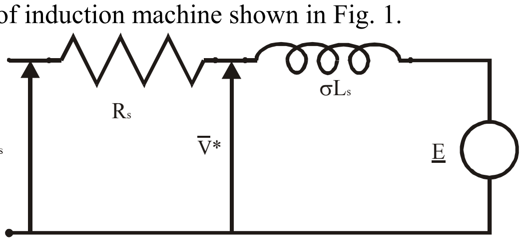

Fig. 1. Equivalent circuit of induction machine

Change of stator current can be found from the Fig. 1 as:

$$\Delta\bar{I}_s(k) = \frac{\bar{V}^*(k) - \bar{E}(k)}{\sigma L_s}\Delta t, \qquad (10)$$

where, $\sigma = 1 - L_m^2 / L_s L_r$ is the leakage coefficient and

$$\bar{V}^*(k) = \bar{V}_s(k) - R_s \bar{I}_s(k) \qquad (11)$$

$$\bar{E}(k) = j\omega_e(k)\left[\bar{\lambda}_s(k) - \sigma L_s \bar{I}_s(k)\right] \qquad (12)$$

are stator voltage with neglected IR drop and the back emf, which is assumed to be sinusoidal with dominant frequency ω_e. From Eq. (2, 3, 4, 10, 12) stator current is found as:

$$\bar{I}_s(k) = \frac{\left(1 + \sigma T_r^2 \omega_s^2(k)\right) + j(1-\sigma)T_r \omega_s(k)}{L_s\left(1 + \sigma^2 T_r^2 \omega_s^2(k)\right)}\bar{\lambda}_s(k), \qquad (13)$$

where $\omega_s(k) = \omega_e(k) - \omega(k)$ is the slip frequency, and $T_r = L_r / R_r$ is the rotor time constant.

Expresions (12) and (13) have to be substituted in (10), so the change of stator current will be:

$$\Delta\bar{I}_s(k) = \frac{\Delta\bar{\lambda}_s(k)}{\sigma L_s} - j\omega_e(k)\Delta t \frac{(1-\sigma)L_r}{\sigma L_s\left(1 + \sigma^2 T_r^2 \omega_s^2(k)\right)}\bar{\lambda}_s(k) - \\ - \omega_e(k)\Delta t \frac{(1-\sigma)T_r \omega_s(k) L_r}{L_s\left(1 + \sigma^2 T_r^2 \omega_s^2(k)\right)}\bar{\lambda}_s(k) \qquad (14)$$

In order to find expression for change in motor torque during a sample period, Eq. (13) and (14) should be substituted in (9). It is very useful to use polar representation of flux vectors shown on Fig. 2.

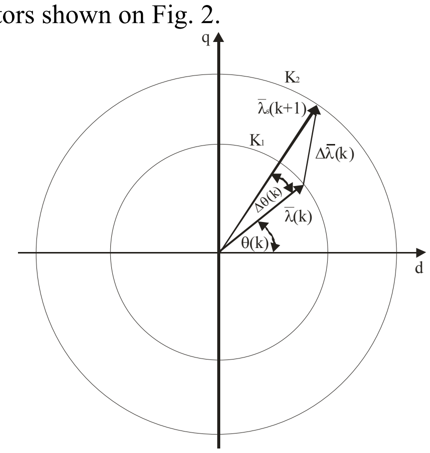

Fig.2. Definition of stator flux vector increment

Stator flux vector $\bar{\lambda}_s(k)$ has the angle $\theta(k)$ to the axes fixed to the stator. Desired flux magnitude Φ^* is represented by a circle centered in the origin with a radius equal to the magnitude of flux reference $\left|\bar{\lambda}(k+1)\right| = \Phi^*$. The desired stator flux vector increment (7) from Fig. 2 is defined by circle radius and the angle $\Delta\vartheta(k)$. It can be seen from the Fig. 2 that:

$$\bar{\lambda}_s(k) \times \Delta\bar{\lambda}(k) = \bar{\lambda}_s(k) \times \left[\bar{\lambda}_s(k+1) - \bar{\lambda}_s(k)\right] = \\ = \left|\bar{\lambda}_s(k)\right| \cdot \left|\bar{\lambda}_s(k+1)\right| \sin\Delta\vartheta(k) \qquad (15)$$

$$\Delta\bar{\lambda}_s(k) \times j\bar{\lambda}(k) = \left|\bar{\lambda}_s(k)\right| \cdot \left|\bar{\lambda}_s(k+1)\right| \cos\Delta\vartheta(k) - \left|\bar{\lambda}_s(k)\right|^2, \qquad (16)$$

so the change in torque can be written by substituing (13-14) in (9) and using (15-16) as:

$$\Delta T(k) = \frac{3P(1-\sigma)\left|\bar{\lambda}_s(k)\right|}{2\sigma L_s\left(1 + \omega_s^2(k)\sigma^2 T_r^2\right)} \\ \left[\begin{array}{l} \left|\bar{\lambda}(k+1)\right| \sin\Delta\vartheta(k) - \left|\bar{\lambda}_s(k)\right| \Delta t \omega_e(k) + \\ + \sigma T_r \omega_s \left[\left|\bar{\lambda}(k+1)\right| \cos\Delta\vartheta(k) - \left|\bar{\lambda}(k)\right|\right] \end{array}\right] \qquad (16)$$

For small values of angle $\Delta\vartheta(k)$ sine and cosine are:

$$\sin\Delta\vartheta(k) = \Delta\vartheta(k) \qquad (17)$$

$$\cos\vartheta(k) = 1, \qquad (18)$$

so the desired stator flux vector increment angle is:

$$\Delta\vartheta(k)=\frac{2\sigma L_s\left(1+\omega_s^2(k)\sigma^2T_r^2\right)}{3P(1-\sigma)\left|\overline{\lambda}_s(k+1)\right|\cdot\left|\overline{\lambda}(k)\right|}\Delta T+ \\ +\frac{\left|\overline{\lambda}_s(k)\right|}{\left|\overline{\lambda}(k+1)\right|}\Delta t\omega_e-\frac{\Delta\Phi\sigma T_r\omega_s(k)}{\left|\overline{\lambda}(k)\right|}, \qquad (19)$$

where

$$\Delta\Phi=\Phi^*-\left|\overline{\lambda}_s(k)\right|=\left|\overline{\lambda}_s(k+1)\right|-\left|\overline{\lambda}_s(k)\right|. \qquad (20)$$

It can be seen in Fig. 2 that by increasing the reference flux magnitude, Φ^* the circle radius will be increased (and vice versa), and by increasing the reference torque T^* on the same flux level ($\Phi^*=\left|\overline{\lambda}(k+1)\right|=\left|\overline{\lambda}(k)\right|$) the angle $\Delta\vartheta(k)$ will be increased (and vice versa). If there is no change in reference torque ($\Delta T(k)=0$) and no change in reference flux ($\Delta\Phi=0$ or $\left|\overline{\lambda}(k+1)\right|=\left|\overline{\lambda}(k)\right|$), stator flux vector increment angle is $\Delta\vartheta(k)=\omega_e(k)\Delta t$. This means that the stator flux continues to rotate at synchronous speed. If there is no change in flux ($\Delta\Phi=0$), and the torque has to be increased, it can be seen that the stator flux vector increment angle $\Delta\vartheta(k)$ has to be increased (and vice versa) (19). If there is a change in both stator flux magnitude and torque, stator flux vector increment angle $\Delta\vartheta$ can be increased or decreased depending on torque and flux changes

In Fig. 3, the Eq. 19 is illustrated for the values of the angle $-pi/2\le\Delta\vartheta\le pi/2$ for three levels of stator flux. It is assumed that there is unlimited voltage available, and it can be seen that there is possible to get larger torque with larger flux level.

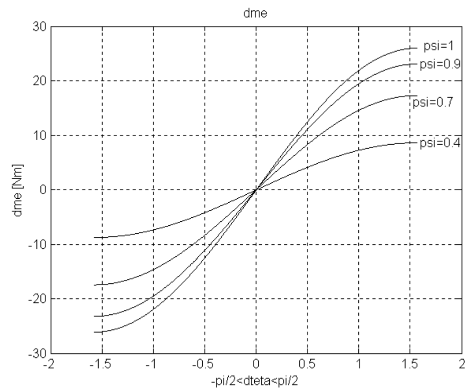

Fig. 3 Plot of Eq. (20) for $-pi/2\le\Delta\vartheta\le pi/2$

When stator flux angle $\Delta\vartheta(k)$ which depends on desired changes in torque and flux is calculated from (19), reference voltage at instant k than is:

$$\overline{V}_s(k)=\frac{\Delta\overline{\lambda}(k)}{\Delta t}+R_s\overline{I}_s(k)=\overline{V}_s^*(k)+R_s\overline{I}_s(k). \qquad (21)$$

Stator flux components are found from Fig. 4 by using their projections.

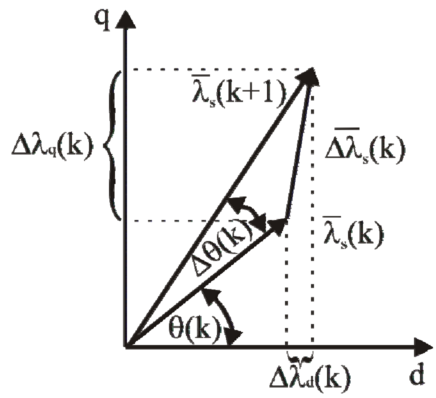

Fig. 4. Projections of stator flux increment vector

$$\Delta\lambda_d(k)=\left|\overline{\lambda}(k+1)\right|\cos(\vartheta(k)+\Delta\vartheta(k))-\left|\overline{\lambda}(k)\right|\cos\vartheta(k) \qquad (22)$$

$$\Delta\lambda_q(k)=\left|\overline{\lambda}(k+1)\right|\sin(\vartheta(k)+\Delta\vartheta(k))-\left|\overline{\lambda}(k)\right|\sin\vartheta(k) \qquad (23)$$

Assuming (22-23) and the fact that the stator flux vector components $\lambda_d(k)$ and $\lambda_q(k)$ are known, reference voltage components (21-22) than are:

$$V_d^*(k)=\frac{1}{\Delta t\cdot\left|\overline{\lambda}(k)\right|}\left[\left|\overline{\lambda}(k+1)-\overline{\lambda}(k)\right|\lambda_d(k)-\left|\overline{\lambda}(k)\right|\lambda_q(k)\Delta\vartheta(k)\right] \qquad (24)$$

$$V_q^*(k)=\frac{1}{\Delta t\cdot\left|\overline{\lambda}(k)\right|}\left[\left|\overline{\lambda}(k+1)-\overline{\lambda}(k)\right|\lambda_q(k)+\left|\overline{\lambda}(k)\right|\lambda_d(k)\Delta\vartheta(k)\right] \qquad (25)$$

The stator voltage vector reference from (21) than is:

$$\overline{V}_s(k)=\left(V_d^*(k)+jV_q^*(k)\right)+R_s\overline{I}_s(k) \qquad (26)$$

It is important to see that stator flux angle $\vartheta(k)$ doesn't have to be estimated directly than through its components, so estimation process is easier and there is no trigonometric functions in (23-24).

3. Rotor flux changes

In stator-flux based strategies, rotor flux changes caused by torque changes must be analysed due to problem of drive stability [1, 9]. Rotor flux dynamic during the stator flux changes can be neglected becouse of large rotor time constant, and mahtematical model of IM in steady state (1-6) can be used. Stator flux amplitude than is:

$$\left|\overline{\lambda}_s\right|=\frac{\left|\overline{V}_s^*\right|}{\omega_e}. \qquad (27)$$

and machine torque can be found by substituing (12) into (5) as:

$$T_e=\frac{3}{2}P\left(\frac{\left|\overline{V}_s^*\right|}{\omega_e}\right)^2\frac{R_r\omega_s}{\left(\frac{L_s}{L_m}\right)^2\left[R_r^2+\sigma^2\omega_s^2L_r^2\right]}. \qquad (28)$$

Machine torque expressed by rotor flux can be found by substituing (3-4) into (28) as:

$$T_e=\frac{3}{2}P\frac{\left|\overline{\lambda}_r^2\right|}{R_r}\omega_s, \qquad (29)$$

and break-down found by maximizing (28) than is:

$$T_{BD} = \pm\frac{3}{4}P\left(\frac{\left|\overline{V}_s^*\right|}{\omega_e}\right)^2 \frac{1-\sigma}{\sigma L_s}. \tag{30}$$

From Eq. (28-29) equation for rotor flux as function of stator flux can be found as:

$$\lambda_r^4 - \left(\frac{L_m}{L_s}\frac{\left|\overline{V}_s^*\right|}{\omega_e}\right)^2 \left|\overline{\lambda}_r\right|^2 + \sigma^2 L_r^2 \frac{4}{9P^2}T_e^2 = 0 \tag{32}$$

To have a real solution of Eq. (32), condition (33) must be followed:

$$\left(\frac{L_m}{L_s}\frac{\left|\overline{V}_s^*\right|}{\omega_e}\right)^4 - 4\sigma^2 L_r^2 \frac{4}{9P^2}T_e^2 \geq 0, \tag{33}$$

from which condition (34) is found as:

$$T_e \leq \frac{3}{4}P\left(\frac{\left|\overline{V}_s^*\right|}{\omega_e}\right)^2 \frac{1-\sigma}{\sigma L_s}, \tag{34}$$

or reference torque must be lower than break-down torque, $T_e^* \leq T_{BD}$. Rotor flux found from (32) than is:

$$\left|\overline{\lambda}_r\right| = \sqrt{\frac{\left(\frac{L_m}{L_s}\frac{\left|\overline{V}_s^*\right|}{\omega_e}\right)^2 + \sqrt{\left(\frac{L_m}{L_s}\frac{\left|\overline{V}_s^*\right|}{\omega_e}\right)^4 - 4\sigma^2 L_r^2 \frac{4}{9P^2}T_e^2}}{2}}. \tag{35}$$

In case of no load ($T_e = 0$), rotor flux $\left|\overline{\lambda}_r^0\right|$ is simply:

$$\left|\overline{\lambda}_r^0\right| = \frac{L_m}{L_s}\frac{\left|\overline{V}_s^*\right|}{\omega_e}, \tag{36}$$

and when load torque is equal to break - down torque $T_e = T_{BD}$ the minimal rotor flux $\left|\overline{\lambda}_r^{MIN}\right|$ is given by:

$$\left|\overline{\lambda}_r^{MIN}\right| = \frac{1}{\sqrt{2}}\frac{L_m}{L_s}\frac{\left|\overline{V}_s^*\right|}{\omega_e}. \tag{37}$$

From (36) and (37) it can be concluded that in stator flux oriented schemes, rotor flux will decrease for $\sqrt{2}$ times from no-load torque to load torque equal to break – down torque when stator flux is kept constant:

$$\frac{\lambda_r^0}{\lambda_r^{MIN}} = \sqrt{2}. \tag{38}$$

Eq. (35) is shown on Fig. 4. for a motor with parameters given in Appendix 1. ($T_{BD}/T_{enom} = 5{,}25$).

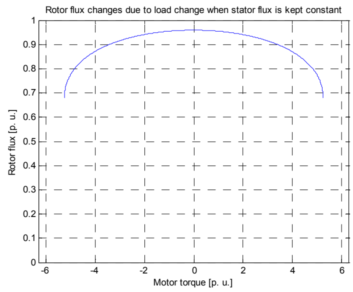

Fig. 4. Changes of rotor flux due to load torque when stator flux is kept constant

As it is shown on Fig. 4, rotor flux is decreased when load torque increase. In case when desired (reference) torque is larger than realisable (break – down torque dependent on flux level), drive loses its stability. As stator – flux based technique, this method must have reference torque limiter in order to keep drive stability (Eq. (34)). Changes of rotor flux due to torque increase are to be compensated by changes of synchronous speed (by accelerating stator flux vector).

4. Direct Torque Control Block Diagram

DTC control scheme based on inverse IM model can be formed from Eq. (19), (24) and (25) like in [22]. Desired change in torque is exspressed as diference between reference T^* and actual torque

$$\Delta T(k) = T^* - T(k), \tag{39}$$

and with change in flux (20) are substituted into (19). However, inverse model – based strategies are highly parameter sensitive and in regimes when desired changes of flux (20) and torque (39) are too large, voltage calculated from (24) and (25) can be larger than available. In order to improve robustnes of the drive, alternative approach will be used. Eq. (20) can be rewritten into the following form:

$$\Delta\theta(k) = PI_1[\Delta T(k)] - PI_2[\Delta\Phi(k)] + \omega_e(k)\Delta t, \tag{40}$$

where the first and second term on the right hand side of (40) represent stator flux angle changes due to torque and flux changes, while the third term is steady-state stator flux angle. When machine is in steady state, first and second term should be equal to zero. Instead of using inverse IM model from (20), parameters $PI_1[\Delta T(k)]$ and $PI_2[\Delta\Phi(k)]$ are choosen to be outputs of two PI regulators in order to achieve zero value of change in angle $\Delta\vartheta(k)$ in steady state. In this case, IM inverse model which is parameter senistive is replaced by double feedback structure as shown on Fig. 5 what significantly improves robustnes of the drive.

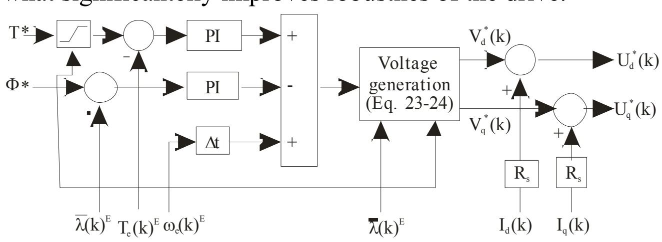

Fig. 5. Block Diagram of the Proposed DTC Structure

Torque reference must be limited due to drive stability condition (34), so reference limit block is introduced on Fig. 5. In order to compensate IR voltage drop on stator resistnace, an IR compensator block is shown on Fig. 5 according to (26). Estimated values from Fig. 5 are denoted by superscript “E”.

5. Field weakening

As machine speed ω increases, synchronous speed ω_e as well as stator voltage increase, and when speed is equal to nominal (base) speed ω_{eBASE}, stator voltage $\left|\overline{V}^*\right|$ amplitude should be equal to its maximal value

$$\left|\overline{V}^*_{MAX}\right| = \left|U_{MAX} - R_s \overline{I}_{sNOM}\right|, \tag{41}$$

where U_{MAX} is maximal available inverter voltage, and $\overline{I}_{sNOM}$ nominal stator current. Stator flux vector increment amplitude $\Delta\overline{\lambda}_s$ than is equal to maximal (base) amplitude:

$$\left|\Delta\overline{\lambda}_{sBASE}\right| = \left|\overline{V}^*_{MAX}\right|\Delta t = const.. \tag{42}$$

with increment angle

$$\Delta\vartheta_{BASE} = \omega_{eBASE}\Delta t\,. \tag{43}$$

This is the point where machine enteres field weakening region, what is shown on Fig. 6. Further increase in synchronous speed (angle $\Delta\vartheta$) is possible only if stator flux is decreased becouse voltage is in limit (42). Stator flux amplitude when machine enteres field weakening region is from (41) and (27) can be found as:

$$\left|\overline{\lambda}_{sBASE}\right| = \frac{\left|\overline{V}^*_{MAX}\right|}{\omega_{eBASE}}. \tag{44}$$

From (42-44) change in stator flux due to synchronous speed increase when voltage is kept on maximum value in field weakening is simply:

$$\left|\overline{\lambda}_s(k)\right| = \left|\overline{\lambda}_{sBASE}\right| \frac{\omega_{eBASE}}{\omega_e(k)}\,. \tag{45}$$

Eq. (45) can be used as stator flux reference Φ^* in Fig. 5 in field weakening region (for speeds above base ω_{eBASE}). Base speed ω_{eBASE} is nominal synchronous machine speed, and base flux $\left|\overline{\lambda}_{sBASE}\right|$ is calculated from nominal voltage, current, stator resistance and base speed (44) and (45).

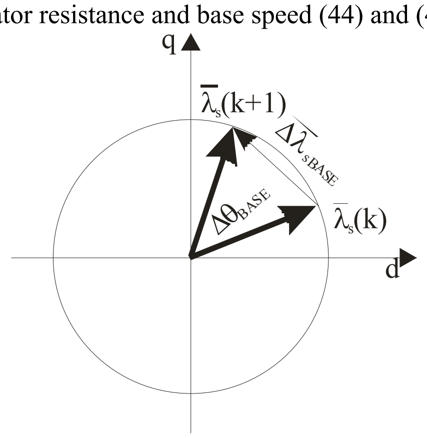

Fig.6. Situation when machine enteres field weaking zone.

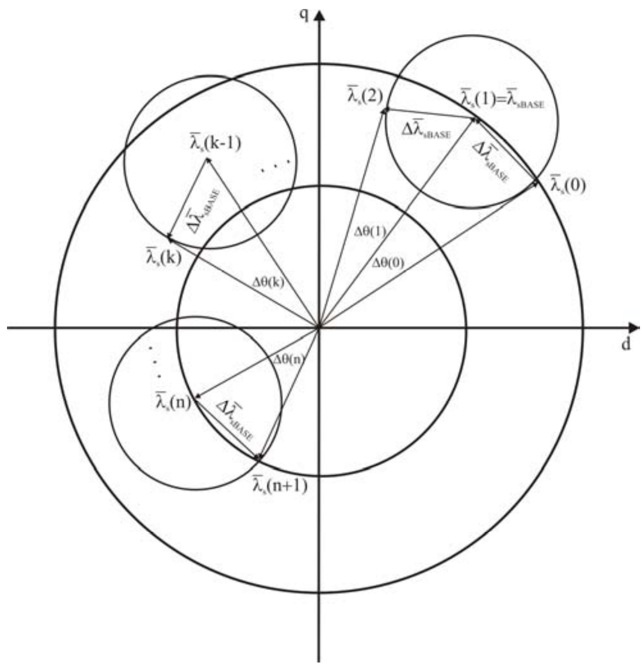

Fig. 7. Transient in field weakening when machine is supplied with maximum available voltage.

To use full available voltage in field weakening, it is desirable to let $\left|\Delta\overline{\lambda}_s\right| = \left|\Delta\overline{\lambda}_{sBASE}\right|$ during the whole transient period. This means that stator flux vector increment tip will lay on circles which radius is equal to (42) during the transient as shown on Fig. 7.

Starting from base speed ω_{eBASE} at instant $k=1$ stator flux is decreased from starting value $\left|\overline{\lambda}(1)\right| = \left|\overline{\lambda}_{sBASE}\right|$ to final value at instant n as:

$$\left|\overline{\lambda}_s(n)\right| = \left|\overline{\lambda}_{sBASE}\right| \frac{\omega_{eBASE}}{\omega_e(n)} \tag{46}$$

by utilizing full inverter voltage $\left|\overline{V}^*_{MAX}\right|$ during the whole transient regime as shown on Fig. 7. During the transient, stator flux is decreased, and therefore maximum torque available (30) is decreased due to rotor flux decrease (35). Condition (34) must be followed to keep drive stability .

6. Estimation

Proposed DTC algorithm is based only on stator quantities, so equation (1) can be used for stator flux vector estmation based on knowing only stator currents and voltages. The goal is to estimate stator flux components, $\lambda_d(k)$, $\lambda_q(k)$, and from them synchronous speed $\omega_e(k)$ and motor torque $T_e(k)$ as well as stator flux angle $\vartheta(k)$. In this paper, simple flux estimator based on Eq. (1)) which uses low pass filter instead of pure integrators is used [1]

When flux components are known, flux modulus is simply:

$$\left|\overline{\lambda}^E_s(k)\right| = \sqrt{\left[\lambda^E_d(k)\right]^2 + \left[\lambda^E_q(k)\right]^2}\,, \tag{47}$$

and machine torque from (5) is:

$$T^E_e(k) = \frac{3P}{2}\left\{\lambda^E_d(k)\cdot\overline{I}_q(k) - \lambda^E_q(k)\cdot\overline{I}_d(k)\right\}. \tag{48}$$

Synchronous speed and stator flux angle are found from:

$$\omega_e(k) = \frac{d\vartheta(k)}{dt} = \frac{\lambda_d^E \dfrac{d\lambda_q^E}{dt} - \lambda_q^E \dfrac{d\lambda_d^E}{dt}}{\left[\lambda_d^E\right]^2 + \left[\lambda_q^E\right]^2}, \qquad (49)$$

$$\vartheta(k) = \int \omega_e(k)dt . \qquad (50)$$

Only stator – fixed frame current $I_d(k)$ and $I_q(k)$ have to be measured, while stator voltage can be calculated directly from the PWM pattern.

7. SIMULATION RESULTS

Proposed algorithm is simulated in Matlab Simulink and obtained results are given on Fig. 8. Motor torque reference is given as square shaped, and machine is in no-load condition with nominal flux level. There is no speed regulation, and machine works in torque regulated mode as shown on Fig. 5. Decoupled control of torque and flux is aciheved with very fast transient response, what can be seen on Fig. 8.a. and Fig. 8.b.

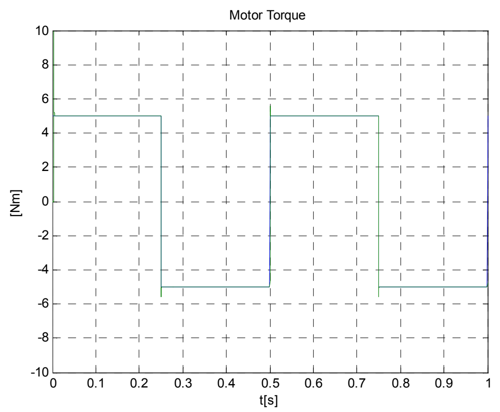

Fig. 8.a. Reference and motor torque

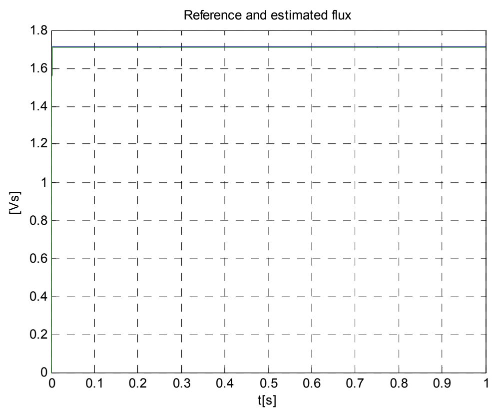

Fig. 8.b. Reference and estimated stator flux

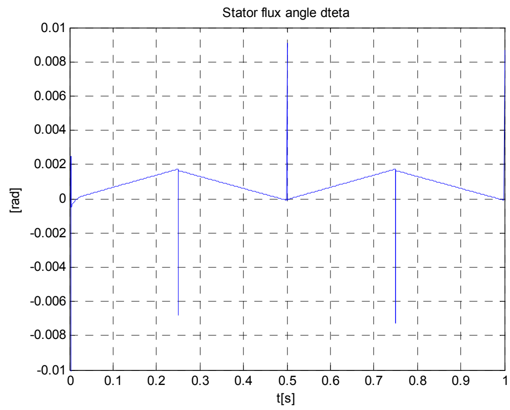

Fig. 8.c. Stator flux angle $\Delta\vartheta$

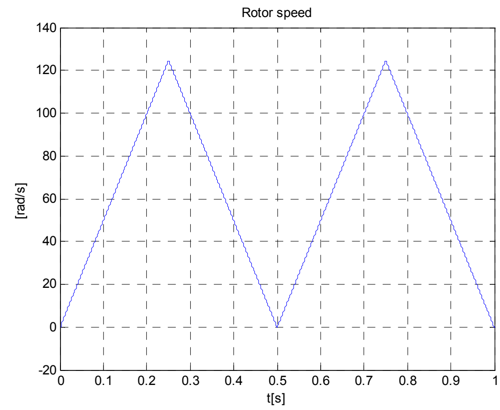

Fig. 8.d. Rotor speed ω_m

On Fig. 8.c. stator flux angle increment (40) is shown. As it can be seen from Fig. 8.c and Fig. 8.d, as speed increase and torque is kept constant (Fig. 8.a), stator flux angle must increase. Stator currents are shown on Fig. 8.e.

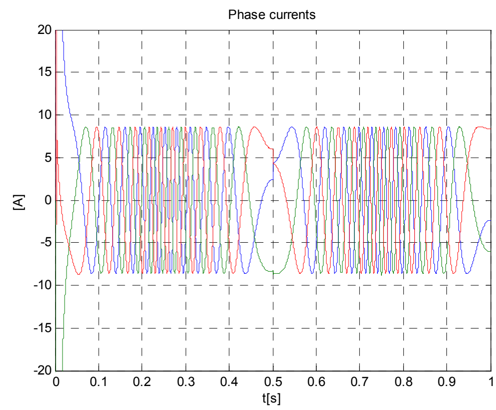

Fig. 8.e. Phase currents

On Fig. 9 closed speed loop drive is simulated. Machine is working in field weakening region with speed reference equal to double nominal speed. At $t = 0.8s$ motor is loaded with 20% nominal load torque After the speed exceedes nominal value (Fig. 9.a), stator voltage remains constant and equal to nominal stator voltage (Fig. 9.f). Stator flux reference is decreased inversly to the speed (Fig 9.b), and rotor flux is decreased as load increases due to (35), whati is shown on Fig. 9.d. As load increase, stator flux angle on Fig. 9.e. increase .

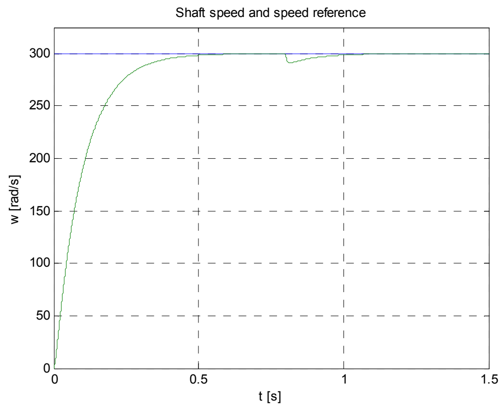

Fig. 9.a Reference and rotor speed ω_m

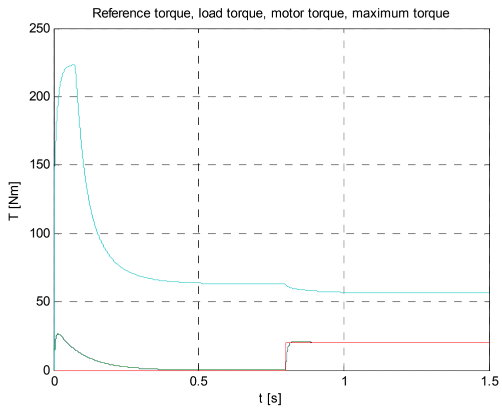

Fig. 9.b. Reference,estimated and load torque

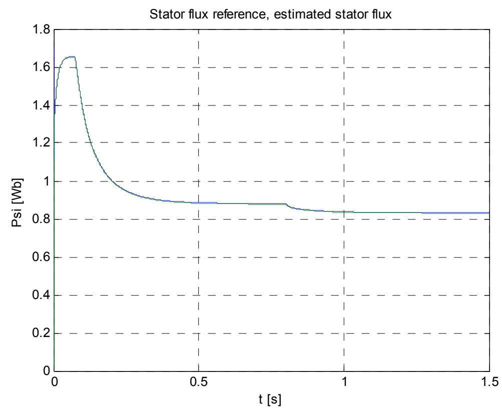

Fig. 9.c. Reference and estimated stator flux

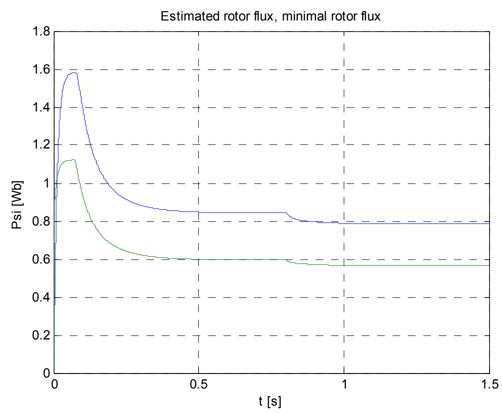

Fig. 9.d. Estimated and minimal rotor flux (37)

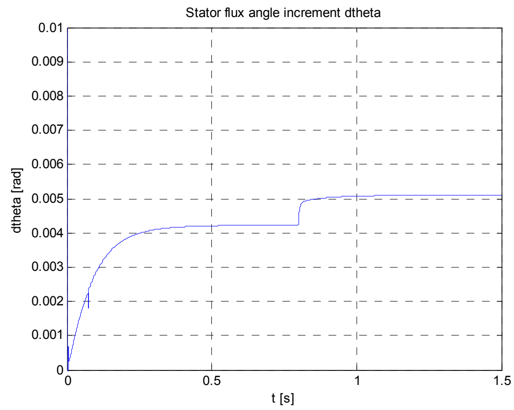

Fig. 9.e. Stator flux angle $\Delta\vartheta$

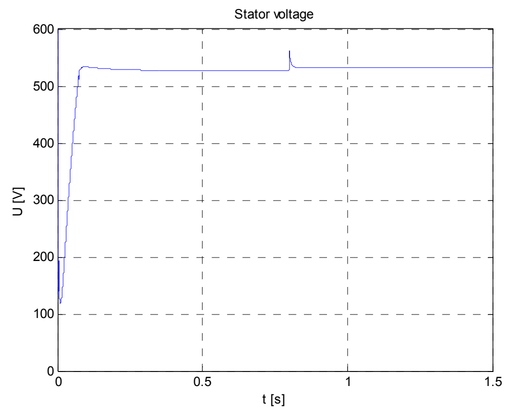

Fig. 9.f. Stator voltage amplitude reference

8. Conclusion

In this paper one simple sensorlesss direct torque control algorithm for induction motor is presnted. Algorithm has no inner current regulation controll loop, speed sensor as well as coordinate transformations. It is based on stator flux control, and therefore it is suitable for further investigations in field weakening region. Robustnes of the system is acheived by using original regulation structure based on two PI regulators instead of using inverse model based algorithms.

Rotor flux can't be changed fast due to large rotor time constant, so RFOC based structures have poor torque regulation in field weakening region. Rapid change of stator flux and therefore synchronous speed is benefit of stator-flux based DTC stragegies. Becouse rotor flux changes much slower than stator flux, fast torque response is achieved by fast change of synchronous speed and therefore a machine slip. This is the reason why proposed algorithm has very good performances in voltage limit region. Stability condition must be followed in order to keep stability becouse break-down torque decreases as rotor flus decreases.

Appendix

The rated values and parameters for the machine ZK-132 used in the simulation are:

Rated output power: 7.5kW
Rated voltage: 380V Δ
Rated frequency: 50Hz
Pole-pair number: 2
Rated speed: 1440rpm
Power factor: 0.82
Stator resistance: 2.04Ω
Rotor resistance: 1.87Ω
Stator Inductance: 8 mH
Rotor Inductance: 92mH
Mutual Inductance: 0.191H

REFERENCES

[1] Peter Vas: Sensorless Vector and Direct Torque Control, Oxford University Press, London, 1998.

[2] R. Lorenz, D. Lawson: "Performance of Feedforward Current Reguloators for Field – Oriented Induction Machine Controllers", IEEE Transactions on Industry Applications, Vol. 1A-23, No.4, pp. 597-602, July/August 1987

[3] F. Britz, M. Degner, R. Lorenz: "Analysis and Design of Current Regulators Using Complex Vectors", *IEEE Transactions on Industry Applications*, Vol. 36, No. 3, May/June 2000.

[4] L. Harnefors, H. P. Nee: "Model – Based Current Control of AC Machines Using the Internal Model Control Method", IEEE Transactions on Industry Applications, Vol. 34, No. 1, January/February 1998.

[5] J. Jung, K. Nam: "A Dynamic Decoupling Control Scheme for High - Speed operation of Induction Motors", IEEE Transactions on Industrial Electronics, Vol. 46, No. 1, pp.100-110, February 1999.

[6] D. W. Novotny, T. A. Lipo: *Vector Control and Dynamics of AC Drives*, Oxford University Press, London, 1997.

[7] Barbara H. Kenny, Robert D. Lorenz: "Stator and Rotor Flux Based Deadbeat Direct Torque Control of Induction Machines", IEEE Transactions on Industry Applications, Vol 39, No. 4, July/August 2003.

[8] R. Doncker, D. Novotny: "The Universal Field Oriented Controller", *IEEE Transactions on Industry Applications*, Vol. 30, No. 1, January/February 1994.

[9] Sang-Hoon Kim, Seung-Ki Sul: "Maximum Torque Control of an Induction Machine in the Field Weakening Region", *IEEE Transactions on Industry Applications*, Vol. 31, No.4, July/August 1995.

[10] Rudolf S. Wieser: "Optimal Rotor Flux Regulation for Fast – Accelerating Induction Machines in the Field – Weakening Region", *IEEE Transactions on Industry Applications,* Vol. 34, No.5, September/October 1998.

[11] Jul – Ki Seok, Seung – Ki Sul: "Optimal Flux Selection of an Induction Machine for Maximum Torque Operation in Flux – Weaking Region", *IEEE Transactions on Power Electronics*, Vol. 14, No. 4, pp. 700-708, July 1999.

[12] Fernando Briz, Alberto Diez, Micahel W. Degner, Robert D. Lorenz: "Current and Flux Regulation in Field –Weakening Operation", *IEEE Transactions on Industry Applications,* Vol. 37, No.1, pp. 42-50, January/February 2001.

[13] Lennart Harnefors, Kai Pietilainen, Lars Gertmar: "Torque – Maximizing Field-Weakening Control: Design, Analysis, and Parameter Selection", *IEEE Transactions on Industrial Electronics*, Vol. 48, No.1, February 2001.

[14] Myoung – Ho Shin, Dong – Seok Hyun: "Speed Sensorless Stator Flux – Oriented Control of Induction Machine in the Field Weakening Region", *IEEE Transactions on Power Electronics,* Vol. 18, No.2, March 2003.

[15] Cristian Lascu, Ion Boldea, Frede Blaabjerg: "A Modified Direct Torque Control for Induction Motor Sensorless Drive", IEEE Transactions on Industry Applications, Vol. 36, No. 1, Jan/Feb 2000.

[16] Y. S. Lai, J. H. Chen: "A New Approach to Direct Torque Control of Induction Motor Drives for Constant Inverter Switching Frequency and Torque Ripple Reduction", IEEE Transactions on Energy Conversion, Vol. 16, No. 3, September 2001.

[17] D. Casadei, G. Serra, A. Tani, L. Zarri, F. Profumo: "Performance Analysis of a Speed Sensorless Induction motor Drive Based on a Constant Switching Frequency DTC Scheme", IEEE Transactions on Industry Applications, Vol. 39, No. 2, March/April 2003.

[18] Z. Sorchini, P. Krein: "Formal Derivation of Direct Torque Control for Induction Machines", IEEE Transactions on Power Electronics, Vol. 21, No.5, September 2006.

[19] Dj. M. Stojic, S. N. Vukosavic: "A New Induction Motor Drive Based on the Flux Vector Acceleration Method", IEEE Transactions on Energy Conversion, Vol. 20, No. 1, pp.173-180, March 2005.

[20] C. Lascu, A. Trzynadlowski: "Combining the Principles of Sliding Mode, Direct Torque Control, and Space-Vector Modulation in a High-Performance Sensorless AC Drive", IEEE Transactions on Industry Applications, Vol. 40, No. 1, pp. 170-177, January/February 2004.

[21] Thomas G. Habetler, Francesco Profumo, Michele Pastorelli, Leon M. Tolbert: "Direct Torque Control of Induction Machines Using Space Vector Modulation", IEEE Transactions on Industry Applications, Vol 28, No.5, pp.1045-1052. Sept/Oct 1992.

[22] P. Matić, B. Blanuša, S. N. Vukosavić, "A Novel Direct Torque and Flux Control Algorithm for the Induction Motor Drive", IEEE International Electric Machines and Drives Conference, IEMDC'03, Proceedings, Vol. 2, pp. 965-970, 1-4. June 2003.

AN IMPROVED LOSS MODEL BASED ALGORITHM FOR EFFICIENCY OPTIMIZATION OF THE INDUCTION MOTOR DRIVES

Branko Blanuša, Petar Matić, Željko Ivanović, Slobodan N. Vukosavić

Abstract: *New algorithm, based on loss model and torque reserve control, for efficiency optimization of the induction motor drive is presented in this paper. As a result, power and energy losses are reduced, especially when load torque is significant less compared to its nominal value. This algorithm can be used in high performance drive and present good compromise between power loss reduction and good dynamic characteristics. Simulation and experimental tests are performed.*

Keywords: *Efficiency Optimization, Induction Motor Drive, Loss Model, Parameter Identification, TorqueRreserve*

1. INTRODUCTION

Induction motor is without doubt the most used electrical motor and a great energy consumer [1]. Three-phase induction motors consume 60% of industrial electricity and considerable efforts to improve their efficiency are taken [1]. Most of motors operate at constant speed although the market for variable speed is expanding. Moreover, induction motor drive (*IMD*) is often used in servo drive application. Vector control (*VC*) or Direct Torque Control (*DTC*) are the most often used control techniques in the high performance applications.

There are numerous papers in which problem of efficiency optimization of the *IMD* in the last 20 years is treated. Although, good results achieved, there is no generally accepted method. There are three strategies which are usually used in the efficiency optimization of the induction motor drive [2]:

- Simple State Control-*SSC;*
- Loss Model Control-*LMC* and
- Search Control –*SC*.

First strategy is based on controling one variable in the drive. The variable must be measured or estimated and its value is used in the feedback control to keep it on predefined reference value. This strategy is simple, but gives good results only for the narrower set of the working conditions. Also, it is sensitive to parameter changes due to parameter variations caused by temperature changes and saturation.

In the second strategy power losses model is used for optimal control of drive. This is the fastest strategy, because the optimal control is calculated directly from the loss model. However, power loss modeling and calculation of the optimal operating point can be very complex. Also, this strategy is sensitive to parameter variations.

In the search strategy on-line efficiency optimization control based on searching method is implemented. Optimization variable, stator or rotor flux, is decremented or incremented in steps until the measured input power settles down to the lowest value. This strategy has an important advantage compared to other strategies. It is completely insensitive to parameter variations. The control does not require any motor parameter and the algorithm is applicable universally to any motor.

Besides all good characteristics of search strategy methods, there is an outstanding problem in its use. Flux never reaches its nominal value, and oscillate around it in small steps. Sometimes convergation to optimal value can be to slow.

Very interesting problem for any ptimization algorithm is working with low flux level and a light load. When load is low, optimization algorithm settles down magnetization flux to make balance between iron and cooper losses and reduce total power losses. In this case drive is very sensitive to load perturbations.

LMC algorithm with on-line parameter identification in loss model and torque reserve control implemented for indirect vector controlled *IMD* is proposed in this paper. Parameter identification is based on matrix calculation and Moore-Penrose pseudoinversion. Input power, output power and values of variables in loss model must be known. Torque reserve is determined on calculated reference flux from loss model and current and voltage constrains in machine. For this purpose fuzzy controller is used. Algorithm for efficiency optimization is included in the model of *IMD* and both simulation and experimental studies are performed to validate theoretical development.

Functional approximation of the power losses in induction motor drive is given in the second Section. Procedure of parameter identification in loss model and calculation of optimal magnetization current are described in the third Section. Experimental results are presented in the fourth Section.

2. FUNCTIONAL APPROXIMATION OF THE POWER LOSSES IN THE INDUCTION MOTOR DRIVE

The process of energy conversion within motor drive converter and motor leads to losses in motor windings and magnetic core as well as conduction and commutation losses in the inverter.

Converter losses: Main constituents of converter losses are the rectifier, DC link and inverter conductive and commutation losses. Rectifier and DC link inverter losses are proportional to output power, so the overall flux-dependent losses are inverter losses. These are usually given by:

$$P_{INV} = R_{INV} \cdot i_s^2 = R_{INV} \cdot \left(i_d^2 + i_q^2\right), \tag{1}$$

where i_d, i_q are components of the stator current i_s in d,q rotational system and R_{INV} is inverter loss coefficient.

Motor losses: These losses consist of hysteresis and eddy current losses in magnetic circuit (core losses), losses in stator and rotor conductors (copper losses) and stray losses. At nominal operating point, core losses are typically 2-3 times smaller then cooper losses, but they represent main loss component of a highly loaded induction motor drives [3]. The main core losses can be modeled by [4]:

$$P_{Fe} = c_h \Psi_m^2 \omega_e + c_e \Psi_m^2 \omega_e^2, \tag{2}$$

where Ψ_d is magnetizing flux, ω_e supply frequency, c_h is hysteresis and c_e eddy current core loss coefficient.

Copper losses are due to electric current flow through the stator and rotor windings and are given by:

$$p_{Cu} = R_s i_s^2 + R_r i_q^2. \tag{3}$$

The stray flux losses depend on the form of stator and rotor slots and are frequency and load dependent. Total secondary losses (stray flux, skin effect and shaft stray losses) usually don't exceed 5% of the overall losses [3]. Considering also, that the stray losses are of importance at high load and overload conditions, while the efficiency optimizer is effective at light load, the stray losses are not considered as a separate loss component in the loss function. Formal omission of the stray loss representation in the loss function have no impact on the accuracy algorithm for on-line optimization.

Based on previous consideration, total flux dependent power losses in the drive are given by the following equitation:

$$P_\gamma = (R_{INV} + R_s) i_d^2 + (R_{INV} + R_s + R_r) i_q^2 + c_e \omega_e^{\,2} \psi_m^2 + c_h \omega_e \, \psi_m^2 . \quad (4)$$

Efficiency algorithm works so that flux in machine is less or equal to its nominal value:

$$\psi_D \le \psi_{Dn}, \quad (5)$$

where Ψ_{Dn} is nominal value of rotor flux and linear expression for rotor flux can be accepted:

$$\frac{d\psi_D}{dt} = \frac{R_r}{L_r} L_m i_d - \frac{R_r}{L_r} \psi_D , \quad (6)$$

where $\Psi_D = L_m i_d$ in steady state.

Expression for output power can be given as:

$$P_{out} = d\omega_r \psi_D i_q, \quad (7)$$

where d is positive constant, ω_r angular speed, Ψ_D rotor flux and i_q active component of the stator current.

Based on previous consideration, assumption that position of the rotor flux is correctly calculated (Ψ_Q=0) and relation $P_{in}=P\gamma+P_{out}$ output power can be given by the following equation:

$$P_{in} = a i_d^2 + b i_q^2 + c_1 \omega_e^{\,2} \psi_D^2 + c_2 \omega_e \psi_D^2 + d \omega_r \psi_D i_q , \quad (8)$$

where $a=R_s+R_{INV}$, $b= R_s+R_{INV}+R_r$, $c_1=c_e$ and $c_2=c_h$.

Input power should be measured and exact P_{out} is needed in order to acquire correct power loss value and to avoid coupling between load pulsation and efficiency optimizer.

3. DETERMINATION OF PARAMETERS IN THE LOSS MODEL AND DERIVATION OF THE OPTIMAL MAGNETIZATION CURRENT

Procedure of the parameter determination in the loss model is shown in Fig. 1. There is a modification in the procedure described in paper [3], so the iron losses are considered separately like hysteresis losses and eddy current losses. Inputs to the algorithms are samples of i_d^2, i_q^2, $\omega_e \psi_D^2, \omega_e^2 \psi_D^2, \omega_r \psi_D i_q$ and P_{in} and they are acquired every sample time, usually 100-200µs. As high frequency components do not contribute identification W=[a b c_1 c_2 d]^T, input parameters and P_{in} are averaged within Q intervals $T=QT_S$. The averaging is implemented as the sum of Q consequetive samples of each signal (Fig.1). Column vectors P(:,1), P(:,2), P(:,3), P(:,4) and P(:,5) of matrix P_{Mx5} are created from the M successive values of A_N, B_N, C_{N1}, C_{N2}, D_N, N=1,..,M and vector Y_N is formed from the M averaged values of input power

$$\int_{nT}^{(n+1)T} P_{IN}(t)dt = a \int_{nT}^{(n+1)T} i_d^2(t)dt + b \int_{nT}^{(n+1)T} i_q^2(t)dt +$$
$$c_1 \int_{nT}^{(n+1)T} \left[\psi_D^2(t)\omega_e^2(t)dt\right] + c_2 \int_{nT}^{(n+1)T} \left[\psi_D^2(t)\omega_e(t)dt\right] +$$
$$d \int_{nT}^{(n+1)T} \left[i_q(t)\psi_D(t)\omega_r(t)dt\right]$$
$$Y_N = aA_N + bB_N + c_1 C_{N1} + c_2 C_{N2} + dD_N . \quad (9)$$

Calculation of the vector W_g is based on Moore Penrose pseudoinverse of rectangular matrix P_{Mx5} [3]:

$$W_g = \left[a_g \, b_g \, c_g \, d_g\right]^T = (P^T P)^{-1} PY , \quad (10)$$

and W_g is aproximative solution of matrix equation $PW=Y$, such the value of $\|PW - Y\|$ is minimum.

New vector W_g is usually calculated every 1.5-2s. The choice of Q is essential for correct parameter identification. Credibility of W_g, relies on the excitation energy contained in input signals. Hence, in absence of any disturbances, matrix P^TP is getting near or being singular and values obtained from P should be discarded. In that case values of parameters are not changed and parameter determination is continued.

For a known operational conditions of the induction motor (ω_r and T_{em}) and parameters in the loss model it is possible to calculate current i_d which gives minimum of the power losses [4].

Based on expression (4) power losses can be expressed in terms related to i_d, T_{em} and ω_s as follows

$$P_\gamma(i_d, T_{em}, \omega_e) = \left(a + c_1 L_m^2 \omega_e^2 + c_2 L_m^2 \omega_e\right) i_d^2 + \frac{bT_{em}^2}{(dL_m i_d)^2} . \quad (11)$$

Assuming absence of saturation and specifying slip frequency:

$$\omega_s = \omega_e - \omega_r = \frac{i_q}{T_r i_d} . \quad (12)$$

power loss function can be expressed as function of current i_d and operational conditions (ω_r, T_{em}):

$$P_\gamma(i_d, T_{em}, \omega_r) = \left(a + c_1 L_m^2 \omega_r^2 + c_2 L_m^2 \omega_r\right) i_d^2 +$$
$$\frac{(2c_1\omega_r + c_2) L_m T_{em}}{dT_r} + \left(c_1 \frac{T_{em}^2}{(dT_r)^2} + \frac{bT_{em}^2}{(dL_m)^2}\right) \frac{1}{i_d^2} . \quad (13)$$

Based on equation (13), it is obvious, the steady-state optimum is readily found based upon the loss function parameters and operating conditions.

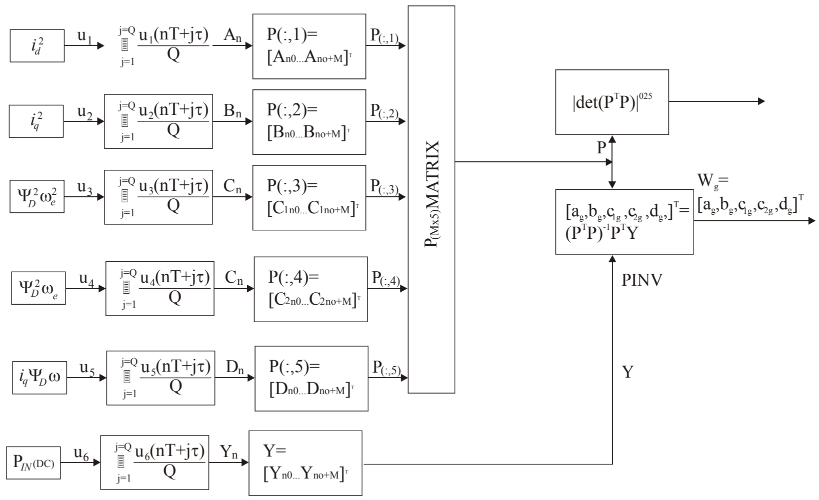

Fig 1. Determination of the parameters in the loss model from input signals.

Substituing $\alpha = \left(a + c_1 L_m^2 \omega_r^2 + c_2 L_m^2 \omega_r\right)$ and $\gamma = c_1 \dfrac{T_{em}^2}{d^2 T_r^2} + \dfrac{b T_{em}^2}{d^2 L_m^2}$ value of current i_d which gives minimal losses is:

$$i_{dopt} = \left(\frac{\gamma}{\alpha}\right)^{0.25}. \tag{14}$$

Presented method is loss model based so it is fast [5]. Optimal value of magnetizing current is directly calculated from the model.

Online procedure for parameter identification is applied, so this method is robust on the parameter variations. One of the greatest problem of *LMC* methods is its sensitivity on load perturbation, especially for light loads when the flux level is low. This is expressed for a step increase of load torque and then two significiant problems appear:

1. Flux is far from its value during transient process, so transient losses are big.
2. Insufficiency in the electromagnetic torque leads output speed to converge slowly to its reference value with significant speed drops. Also, oscillations in the speed response appears.

These are common problem of methods for efficiency optimization based on flux adjusting to load torque. Speed response when step change of load torque (from 0.5 p.u. to 1.1 p.u.), for nominal flux and when *LMC* method is applied, is presented in the Fig. 2. Speed drops and slow speed convergence to its reference value are more exposed for *LMC* method.

These are the reasons why torque reserve control in *LMC* method for efficiency optimization is necessary. Model of efficiency optimization controller with torque reserve control is presented in Fig. 3. Optimal value of magnetization current is calculated from the loss model and for given operational conditions Eq. (14). Increment of magnetizing current (Δid) is generated from the fuzzy rules through the fuzzy inference and defuzzification, on the basis of the previously determined torque reserve (ΔT_{em}). Fuzzy logic controller is used in determination of Δi_d. Controller is very simple, and there is one input, one output and 3 rules. Only 3 membership functions are enough to describe influence of torque reserve in the generation of i_{dopt}^*.

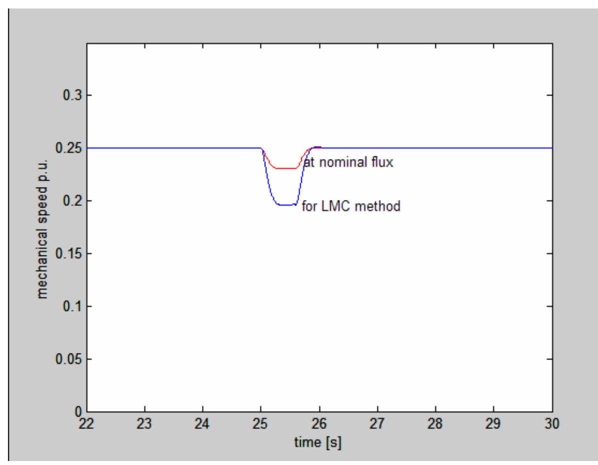

Fig. 2. Speed response on the step load increase for nominal flux and when LMC is applied.

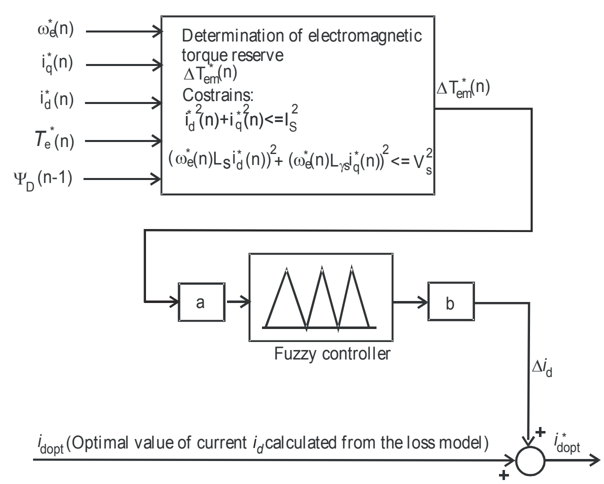

Fig. 3. Block for efficiency optimization with torque reserve control.

If torque reserve is sufficient then $\Delta i_d \approx 0$ and this block have no effect in determination of i_{dopt}^*. Oppositely, current i_d (magnetization flux) increases to obtain sufficient reserve of electromagnetic torque.

Two scaling factors are used in efficiency controller [6]. Factor *a* is used for normalization of input variable, so same controller can be used for a different power range of machine. Factor *b* is output scaling factor and it is used to adjust influence of torque reserve in determination of i^*_{dopt} and obtain requested compromise between power loss reduction and good dynamic response.

IV. EXPERIMENTAL RESULTS

Experimental tests were performed on the Laboratory Station for Vector Control of the Induction Motor Drives -Vectra. Basic parts of the Laboratory Station Vectra are:

- induction motor (3 MOT, Δ380V/Y220V, 3.7/2.12A, cosϕ=0.71, 1400o/min, 50Hz)
- incremental encoder connected with the motor shaft,
- three-phase drive converter (DC/AC converter and DC link),
- PC and dSPACE1102 controller board with TMS320C31 floating point processor and peripherals,
- interface between controller board and drive converter.

Control and acquisition function as well as signal processing are executed on this board, while PC provides comfortable interface toward user.

Algorithms observed in this paper is software realized using Matlab – Simulink, C and real-time interface for dSPACE hardware. Handling real-time applications is done in ControlDesk.

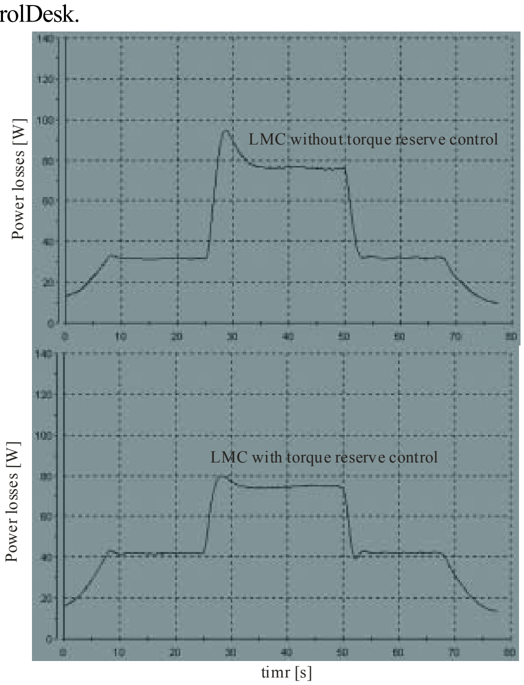

Fig. 4. Graphics of power losses for a step change of load torque.

Power losses and speed response of the drive with and without applied algorithm for torque reserve control are presented in Figs. 4. and 5. respectively. The load torque step changes in t_1=25s from 0.5 p.u. to 1.0 p.u. and vice versa in t_2=50s at constant reference speed ω_{ref}=0.2 p.u.

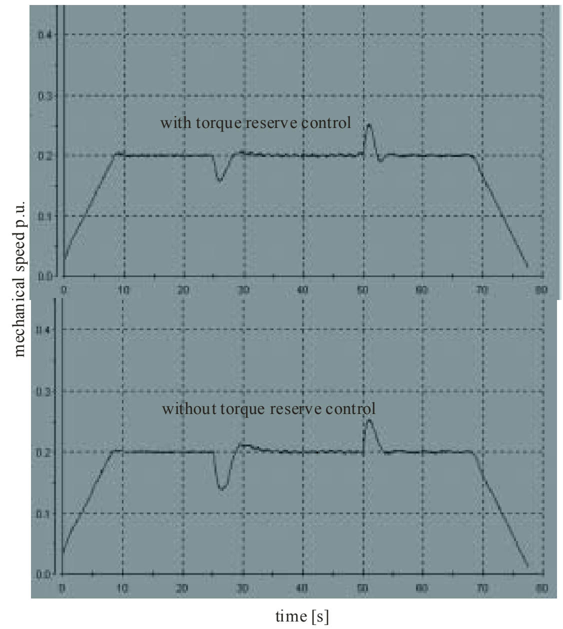

Fig. 5. Graphics of mechanical speed for a step change of load torque.

V. CONCLUSION

By implementation *LMC* method with torque reserve control following results are achieved:

1. Less sensitivity on load perturbation compared to standard *LMC* methods without torque reserve control.
2. Better control characteristics
3. Less transient losses

Algorithm with torque reserve control gives negligible higher losses in a steady state then standard *LMC* methods.

REFERENCES

[1] S. N. Vukosavic: "Controlled Electrical Drives - Status of technology", Proceedings of XLII ETRAN Conf. , pp. 3-16, No. 1, 1998.

[2] F. Abrahamsen, F. Blaabjerg, J. K. Pedersen, P.B. Thogersen, “Efficiency optimized control of medium-size induction motor drives”, Industry Applications Conference, pp. 1489 -1496, Vol. 3, 2000.

[3] S. N. Vukosavi}, E. Levi, “Robust DSP-based Efficiency Optimization of Variable Speed Induction Motor Drive”, IEEE Transaction of Ind. Electronics, Vol. 50, No. 3, 2003.

[4] W. A. Roshen, “Magnetic Losses for Non-Sinusoidal Waveforms Found in AC motors”, IEEE Tran. on Power Electronics, pp. 1138-1141, Vol. 21, No. 4, 2006.

[5] C. Chekaborty, “Fast Efficiency Optimization Techniques for the Indirect Vector Controlled Induction Motor Drives”, IEEE Trans on Industry Applications, pp. 1070-1076, Vol. 39, No. 4, 2003.

[6] Emanuele Cerruto, Alfio Consoli, Antonio Testa, “Fuzzy Adaptive Vector Control of Induction Motor Drives”, IEEE Transactions on Power Electronics, Vol.12, No.6 November 1999.

INSTRUCTION FOR AUTHORS

Name of the author/s, Affiliation/s

Abstract: *Short instruction for authors is presented in this paper. Works that are to be printed in the review "Electronics" should be typed according to this instruction.*
Keywords: *Review Electronics, Faculty of Electrical Engineering in Banjaluka, Instruction for authors.*

1. INTRODUCTION

In the review "Electronics", we publish the scientific and professional works from different fields of electronics in the broadest sense like: automatics, telecommunications, computer techniques, power engineering, nuclear and medical electronics, analysis and synthesis of electronic circuits and systems, new technologies and materials in electronics etc. In addition to the scientific and professional works, we present new products, new books, B. Sc., M. Sc. and Ph.D. theses.

In order to enable the unification of the technical arrangement of the works, to simplify the printing of the review "ELECTRONICS", we are giving this instruction for the authors of the works to be published in this professional paper.

2. TECHNICAL DETAILS

2.1. Submitting the papers

The works are to be delivered to the editor of the review by the E-mail (elektronika@etfbl.net) or on floppy (or CD) by post mail to the address of the Faculty of Electrical Engineering (Elektrotehnicki fakultet, Patre 5, 78000 Banja Luka, Republic of Srpska, Bosnia and Herzegovina).

2.2. Typing details

The work has to be typed on the paper A4 format, 8.27" width and 11.69" height (21.0x29.7 cm), upper margin of 1" (2.54 cm) and lower margin of 0,59" (1,5 cm), left and right margins of 1,57" (2 cm) and 0,39" (1cm) (mirrored margins). The header and footer are 0,5" (1.27cm) and 57" (2 cm). <u>The work has to be written in English language</u>. Our suggestion to the authors is to make their works on a PC using the word processor MS WORD 97/2000, and for the figures to use the graphic program CorelDraw, if the graphs are not going from the original programs, i.e., from the programs received (like MATLAB).

The title of the work shall be written on the first page, in bold and 12 pt. size. Also, on the first page, moved for one line spacing from title, the author's name together with the name of his institution shall be printed in the letter size (10pt, *Italic)*. The remaining parts of the manuscript shall be done in two columns with 0.5cm distance. The work shall be typed with line spacing 1 (Single) and size not less than 10 pt (like as this instruction). After the title of the work and the name of the author/s, a short content in English language follows, written in italics. The subtitles in the text shall be written in bold, capital letters of the size as in the text (not less than 10 pt.). Each work shall, at the beginning, comprise a subtitle INTRODUCTION, and, at the end, the subtitles CONCLUSION and BIBLIOGRAPHY / REFERENCES.

The operators and size marks that do not use numerical values, shall be written in common letters. The size marks that can use numerical values shall be written in italics. The equations shall be written in one column with right edge numeration. If the breaking of equations or figures is desired, those may be placed over both columns.

Illustrations (tables, figures, graphs etc.) may be wider than one column if necessary. Above a table there shall be a title, for instance: Table 2. *The experimental measuring results.* The same applies to figures and graphs but the accompanying text comes underneath the figure of graphs, for instance: Fig.3: *Equivalent circuit diagram...*

The work should not be finished at the beginning of a page. If the last manuscript page is not full, the columns on that page should be made even. Number of pages should not go over 6.

3. CONCLUSION

This short instruction is presented in order to enable the unification of technical arrangement of the works.

4. REFERENCES

At the end of work, the used literature shall be listed in order as used in the text. The literature in the text, shall be enclosed in square brackets, for instance: ...in [2] is shown ...

ELECTRONICS, Vol. 10, No. 1, September/October 2006.